NUCLEAR ENERGY RESEARCH INITIATIVE (NERI)
FINAL REPORT

Project Title:

MOLTEN SALT HEAT TRANSPORT LOOP: MATERIALS CORROSION AND HEAT TRANSFER PHENOMENA

Grant No.: DE-FC07-05ID14675

Project No.: 04-154

Final Report covering Period
April 1, 2005 to March 31, 2008

Submitted by:

Lead Organization:

University of Wisconsin, Madison
Dr. Kumar Sridharan
Dr. Mark Anderson
Dr. Michael Corradini
Dr. Todd Allen
Mr. Luke Olson (Graduate Student)
Mr. James Ambrosek (Graduate Student)
Mr. Daniel Ludwig (Graduate Student)

Submitted on: July 9, 2008

1

TABLE OF CONTENTS

LIST OF FIGURES

LIST OF TABLES

1. INTRODUCTION AND OBJECTIVES

The Next Generation Nuclear Power Plant (NGNP) will likely be the very high-temperature reactor utilizing graphite moderation with TRISO fuel particles in either a prismatic matrix or pebble bed configuration. The NGNP is to be designed to produce two energy products: electricity and process heat for hydrogen production. This extraction of process heat from the NGNP will require an intermediate heat transport loop for process safety. The heat transport fluid should: (i) be chemically compatible with the surrounding structural materials, (ii) have superior fluid-mechanical and heat-transfer properties for an economical design of the process heat exchangers and the heat transport loop, and (iii) have acceptable safety characteristics under normal and off-normal conditions. The fluid most likely will be a high-pressure inert gas (e.g., helium) or a high-temperature molten salt [1]. The interface between the reactor and the hydrogen production system will likely involve long heat transfer paths at elevated temperatures. A potential transport fluid that can be successfully implemented in a heat exchange loop is a molten fluoride salt because of its superior characteristics: large specific heat and good thermal conductivity, high density at low pressures, resistance to radiolysis, and relatively good chemical inertness [1, 2]. This molten salt, if chosen to be properly compatible with the heat exchanger and piping materials, can minimize the temperature drop in the intermediate heat transport loop and the required pumping power, thereby minimizing the delivered cost of the process heat [1]. An immediate challenge for using molten fluoride salts is their corrosive nature at the desired high temperatures of use. In terms of corrosion mechanisms in materials, the molten fluoride salt environment is quite different from other high temperature environments, in that the normally accepted paradigm of developing a protective oxide layer to provide corrosion resistance does not fully apply to this environment, owing to thermodynamically driven dissolution effects [3]. The goals of this research program were to: (i) investigate corrosion rates and mechanisms of a number of potential candidate materials in the molten salt environment that will provide directions for appropriate alloy selection and development of new alloys specifically for the heat transfer application, (ii) design a molten salt flow loop to study heat transfer performance, and (iii) observe corrosion effects and document the associated molten salt loop design and heat transport performance for the NGNP project as an integral and separate-effects database.

2. SUMMARY OF ACCOMPLISHMENTS

2.a. Abstract

An experimental system for corrosion testing of candidate materials in molten FLiNaK salt at 850°C (or higher if necessary) has been designed and constructed. While molten FLiNaK salt was the focus of this study, the system can be utilized for evaluation of materials in other molten salts that may be of interest in the future. Using this system, the corrosion performance of a number of code-certified alloys of interest to NGNP as well as the efficacy of Ni-electroplating have been investigated. The mechanisms underlying corrosion processes have been elucidated using scanning electron microscopy, x-ray diffraction, and x-ray photoelectron spectroscopy of the materials after the corrosion tests, as well as by the post-corrosion analysis of the salts using inductively coupled plasma (ICP) and neutron activation analysis (NAA) techniques. High temperature electrochemisty was performed of FLiNaK salt at 650°C to detect the extent Cr and Fe dissolution in the salt. This included anodic stripping voltammetry and cyclic voltammetry, and these techniques while providing fundamental insights of corrosion processes in molten salts, also provide the basis for the development of probes for on-line monitoring of corrosion in molten salt systems in industrial environments. Since graphite and carbon-based materials may be used for

structural components in molten salt systems, the strength and molten salt environmental compatibility of a high temperature graphite-based epoxy has been evaluated in detail. Heat transfer analysis of flowing molten FLiNaK salt in various candidate structural materials has been performed and bench marked against the results of previous researchers. A design for a molten flow loop has been completed. Interactions have been fostered with other research groups working in this area in the U.S., including Oak Ridge National Laboratory, Idaho National Laboratory, University of California, Berkeley, and University of Nevada, Las Vegas.

2.b. Graduate and Undergraduate Students

Three graduate students have been involved in this research. Mr. Luke Olson and Mr. James Ambrosek are pursuing their Ph.D. degrees in this area, and it is anticipated that they will get their doctoral degrees in 2009 and 2010, respectively. Mr. Daniel Ludwig will be completing his M.S degree in this area in July 2008. Additionally, undergraduate students Dustin Jacqmin and Graham Bradford (Nuclear Engineering) and Benjamin Hauch (Materials Science and Engineering) have also been involved in this project.

2.c. Conferences, Workshops, and Papers

1. "Plan for First Molten Salt Corrosion Experiments", L.C. Olson, J. W. Ambrosek, and K. Sridharan, **Liquid Salt Workshop**, Oak Ridge National Laboratory, Oak Ridge, TN, October 2005.
2. "Liquid Salt Research at University of Wisconsin", M.H. Anderson, L. Olson, J.W. Ambrosek, K. Sridharan, and T.R. Allen, **Liquid Salt Technical Working Group**, Pratt & Whitney Rocketdyne Desoto Facility, Conoga Park, CA, October, 2005.
3.. "Experimental Design for Testing Materials Corrosion in Molten Fluoride Salt"; L. Olson, K. Sridharan, M. Anderson, and T. R. Allen, Trans. **American Nuclear Society Annual Conference,** Reno, NV, vol. 94, p.805, June 2006.
4. "Evaluation of Material Corrosion in Molten Fluoride Salt "; L.C. Olson, J.W. Ambrosek, K. Sridharan, M.H. Anderson, T.R. Allen, and M.L. Corradini, **American Institute of Chemical Engineers** Annual Conference, San Francisco, CA, November, 2006.
5. "Molten Salt Research at University of Wisconsin" K. Sridharan and M.H. Anderson **Liquid Salt Workshop** hosted by University of Nevada, Las Vegas, November, 2006.
6. "Alloy Corrosion in Molten FLiNaK Salt"; L. Olson, J. W. Ambrosek, K. Sridharan, M.H. Anderson, and T.R. Allen, **American Nuclear Society Annual Conference,** Boston, MA**,** June 2007.
7. "Electrochemical Analysis of Molten Salts in conjunction with Neutron Activation Analysis", D.C. Ludwig, L.C. Olson, T.R. Allen, M.H. Anderson, K. Sridharan, **American Nuclear Society Transactions**, Anaheim, CA, Vol. 98, June 2008, p. 1040-41.
8. "Materials Corrosion in Molten Salt LiF-NaF-KF Salt"; L.C. OLson, J.W. Ambrosek, K. Sridharan, M.H. Anderson, and T.R. Allen, **Journal of Fluorine Chemistry**, in press, to be published in 2008.
9. "Current Status of Knowledge of the Fluoride Salt (FLiNaK) Heat Transfer", J. Ambrosek, M. Anderson, K. Sridharan and T. Allen, **Nuclear Technology**, in press, to be published 2008.
10. "Corrosion of Materials in Molten Salts", .K. Sridharan*, L.C. Olson, J.W. Ambrosek, D.C. Ludwig, Y. Chen, M.H. Anderson, L. Tan, and T.R. Allen, **Materials Science and Technology Annual Conference**, Pittsburgh, PA, October 2008.
11. "Anodic Stripping Voltammetry for Quantification of Chromium in Molten FLiNaK", D.C. Ludwig, L.C. Olson, K. Sridharan, M.H. Anderson, T.R. Allen" manuscript under preparation for submission to **Journal of Electroanalytical Chemistry.**
12. Alloy Interaction with Carbon in Molten FLiNaK." L.C. Olson, J.W. Ambrosek, K. Sridharan, M. H. Anderson, and T.R. Allen, **manuscript under preparation** for submission to a journal.

3. HIGH TEMPERATURE STATIC CORROSION TEST SYSTEM

3.a. Salt

From the standpoint of future NGNP applications it is important to select a salt that has good heat transfer characteristics, low vapor pressure, low melting point, high boiling point, and not prohibitively expensive. Because of high volumetric heat capacity of liquid salts in general, the equipment size and the pumping power can be substantially smaller than other heat transport fluids, which in turn can lead to lower equipment and operating costs. For the purposes of illustration, Figure 1 shows the number of 1m diameter pipes needed to transport 1000 MWth with 100ºC rise in coolant temperature. Table 1 shows a the relevant thermal properties of some coolants. Beryllium-containing salts have good heat transfer properties, but the higher toxicity of these salts leads to added handling expenses.

	Water (PWR)	Sodium (LMR)	Helium	Liquid Salt
Pressure (MPa)	15.5	0.69	7.07	0.69
Outlet Temp (ºC)	320	540	1000	1000
Coolant Velocity	6	6	75	6
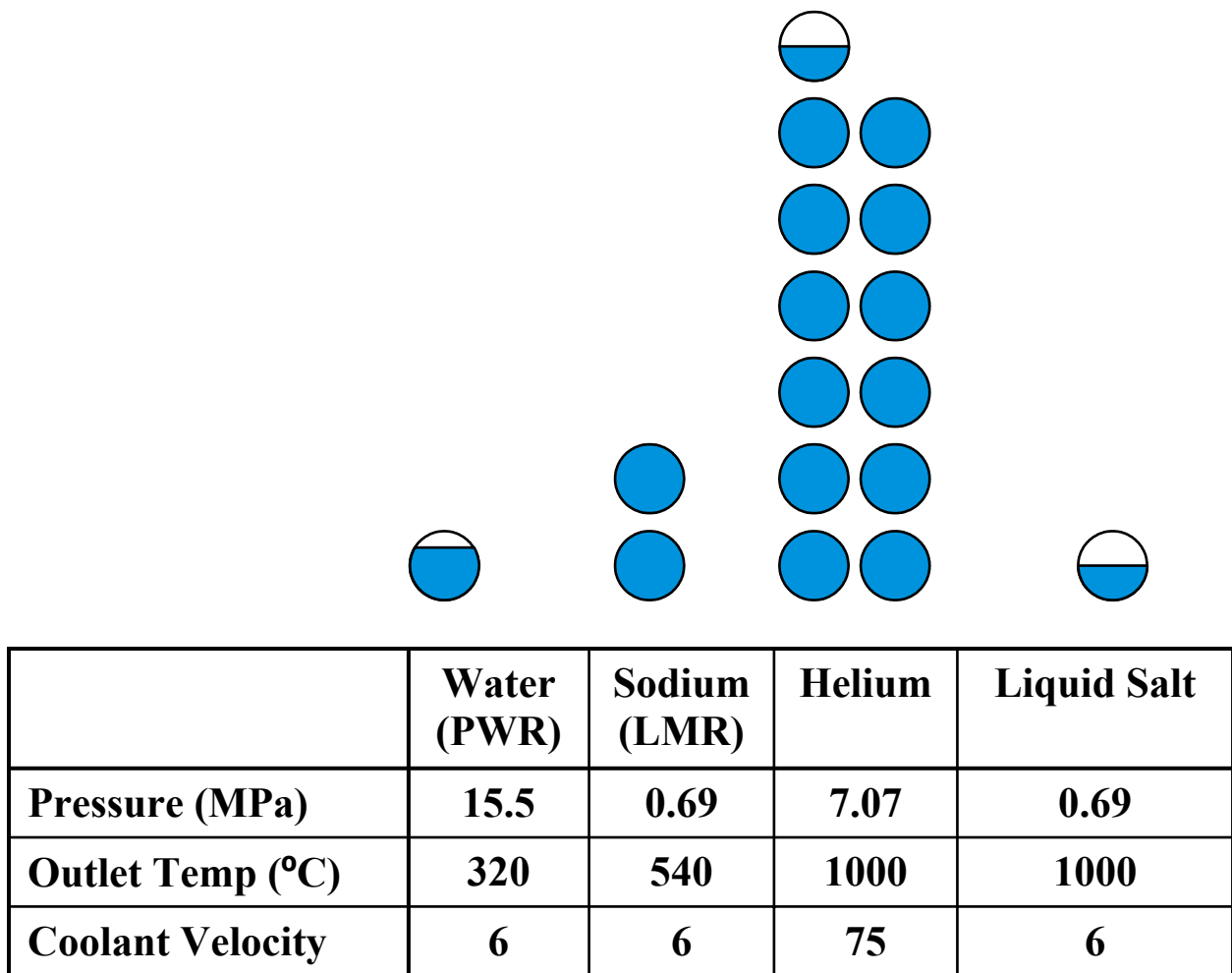
Figure 1. Schematic illustration of the number of 1m diameter pipes needed to transport 1000 MWth with 100ºC rise in coolant temperature [4].

10

Table 1. A comparison of the properties of some coolants [from 5, 6].

Salt (mol %)	Tm (ºC)	ρ (g/cm³)	ρ*Cp, (cal/cmºC)	μ (cP)	k (W/m-K)
FLiBe LiF-BeF2 (66.7-33.3)	460	1.94	1.12	5.6	1
FLiNaK LiF-NaF-KF (46.5-11.5-42)	454	2.02	0.91	2.9	0.92
KCl-MgCl₂ (68-32)	426	1.66	0.46	1.4	0.4
Water (H₂O) @ 20°C	0	1	0.44	1	0.6
He (P=7.5MPa)		0.0038	0.005	0.042	0.29
Na	97.8	0.78	0.23	0.18	60

Based on heat transfer and other considerations stated above, as well as the recent seminal work of Williams et al at ORNL on comparison of a wide range of heat transfer salts, it was decided that high temperature corrosion experiments for this research will be performed in FLiNaK. FLiNaK salt is a eutectic mixture of three fluorides, with a composition 46.5%LiF-11.5%NaF-42%KF and it has a melting point of about 454°C [7, 8]. FLiNaK is well suited for the temperature range used in this research (up to 850°C), due to its low volatility (low vapor pressure) and its relative ease of handling.

Discussions with the molten salt research group at ORNL brought forth the importance of the role of salt purity on corrosion [9]. Based on these discussions it was decided that the FLiNaK salt be procured from Electrochemical Systems Inc. (ECS), also located in Oak Ridge, TN. The company has previously provided these salts for ORNL research and other research programs. The company has extensive experience in salt preparation, sealing in appropriate containment, and shipping. In October 2005, the University of Wisconsin group visited ORNL and ECS to conduct discussions on procurement of this salt. Tha FLiNaK salt was supplied in a sealed nickel vessel (nickel is highly resistant to corrosion in FLiNaK), in which it would be melted at the University of Wisconsin and pumped directly into the static corrosion test cells.

18 kg of high purity FliNaK, purified by a hydrofluorination purification process were procured from ECS. Additionally, 0.97 kg of non-hydrofluorinated FliNaK (slightly lower purity) was procured from Idaho National Laboratory (INL). Finally, FLiNaK salts were also prepared at the University of Wisconsin (UW) by mixing and melting LiF, KF, and NaK in right molar proportions inside an atmosphere controlled glove box. Thus, the three grades of FLiNaK with differing purity levels (but essentially same nominal composition), were available for corrosion testing. While the high purity ECS salt allowed for the evaluation of corrosion without interference from impurities, it also aided in benchmarking the results of this work against previous work at ORNL. The INL and UW FLiNaK salts would provide an evaluation of corrosion at purity levels that would be more representative of a large-scale industrial environment.

3.b. Design and Material of Corrosion Test Cell
3.b.i. Material for Corrosion Cell

From the standpoints of safety, salt purity, salt handling and testing issues several design considerations were explored for the corrosion test cell, prior to arriving at the final design. The material considered for Designs 1 and 2 (described below) for the molten salt containment and other salt contacting components was glassy carbon. This type of amorphous carbon has been demonstrated to be chemically inert to molten salts. Moreover, it is not wetted by molten salt, making it easy to drain the salt out after experiments and reuse the crucible. Discussions were initiated with a company in Germany, Sigradur, which specializes in this material and price quotations for various components were obtained. The drawbacks of this material are its high costs, difficulty in machining, and a limit on maximum thickness procurable (6mm maximum thickness). Design 3 (final design) which involves a disposable crucible utilizes POCO Graphite Grade AXZ-5Q1, with a particle size of 5 µm and a pore size of 0.7 µm [10,11]. This graphite is purified to contain a total ash range of less than 5 ppm. Experience with molten fluoride salts from the MSRE program has indicated that larger pore size can lead to salt infiltration into the graphite [12]. Glassy carbon was however used for high temperature electrochemisty experiments that were preformed separately.

3.b.ii. Design 1

A schematic illustration of the first design is shown in Figure 2. In essence, the design consists of two vessels, a nickel vessel in which the salt would be melted and a glassy carbon corrosion test vessel. The salt would be melted in the Ni vessel and pumped into the glassy carbon corrosion test vessel (containing the samples) for corrosion experiments through a Ni-alloy transfer pipe. Operations in both vessels would be carried out under an argon gas cover. A double-ball valve would be used for sampling the salt composition. This design was not pursued because of concerns in finding high temperature valves for FLiNaK and seals between glassy carbon and nickel, as well as the high material-salt contact area.
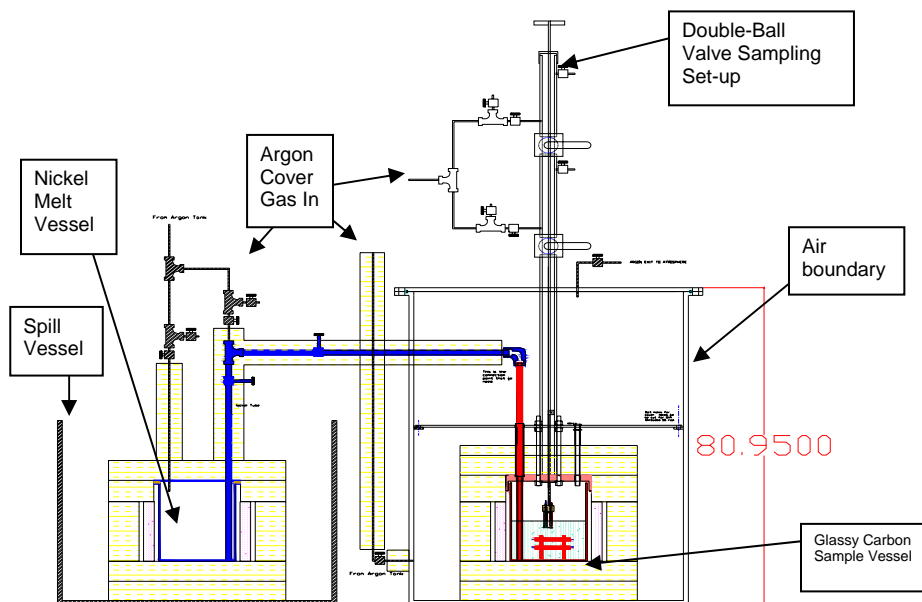
Figure 2. Schematic illustration of the first design explored for the static corrosion testing cell..

3.b.iii. Design 2

A schematic illustration of the second design is shown in Figure 3. This would also involve a glassy carbon crucible, but it would be operated in an argon glove box. In this design, provisions were provided for introducing electrodes for cyclic voltammetric studies. The voltammetric studies would provide on-line information on the effects of dissolution of the alloy constituents in the salt. This design was not pursued after discussions with our collaborators at ORNL, who pointed out that even 1ppm of oxygen in the argon cover-gas could cause contamination, especially over a long term exposure period. Moreover, the voltammetric experiments would introduce more components in direct contact with the salt. It was therefore decided that voltammetric experiments would be investigated in a separate experimental system.

For both designs shown in Figures 2 and 3, a stirring mechanism using either a rotating paddle or flowing argon was considered, in order to induce a small degree of flow of the molten salt during corrosion experiments. Our discussions with ORNL personnel indicated that corrosion by dissolution is limited by thermodynamic parameters rather than transport of species from the corroding surface. Thus, it was decided not to stir the salt, which also has the added benefit in terms of minimizing material/salt interfaces in the corrosion cell.
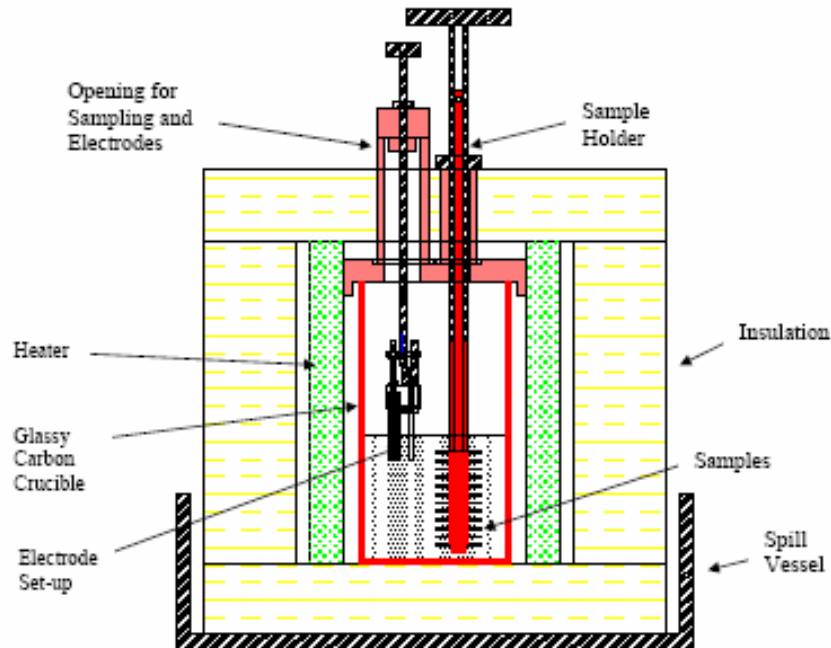
Figure 3. Schematic illustration of the second design explored for the static corrosion test cell.

3.b.iv. Design 3 - Final Design:

A more simplified, cost-effective design was finalized and used for subsequent static corrosion tests (Figure 4). This design uses high-density POCO graphite containment for molten salt rather than glassy carbon. The relatively low costs and ready machinability of this material made it an attractive choice compared to glassy carbon. A separate graphite crucible was used for each corrosion test and each alloy making the minor amounts of salt sticking to the crucible during draining, a non-issue. The tests samples (three samples of a given alloy, alloys tested in triplicate) are fixtured to an axially placed central graphite rod using graphite screws. The graphite crucible with the samples is placed in a stainless steel capsule for safety purposes and top of the crucible is covered with graphite and stainless steel lids with a 1/4" opening for introducing the salt. The top stainless steel lid is then welded shut. All operations are carried out inside an atmosphere controlled glove box. After introducing the salt to the desired level, the opening is welded shut, this operation also being performed inside the glove box. For the INL salt, small granules were introduced into the high-density graphite crucible containing the test samples before the crucible is welded into its stainless steel air boundary.   The stainlesss steel capsule is then placed in a high temperature furnace for corrosion tests. After corrosion testing for a desired duration the furnace temperature is lowered to 500°C and the test capsule is inverted in order for the salt to drain away from the samples. The stainless steel capsule is sectioned using a lathe and the samples are retrieved.
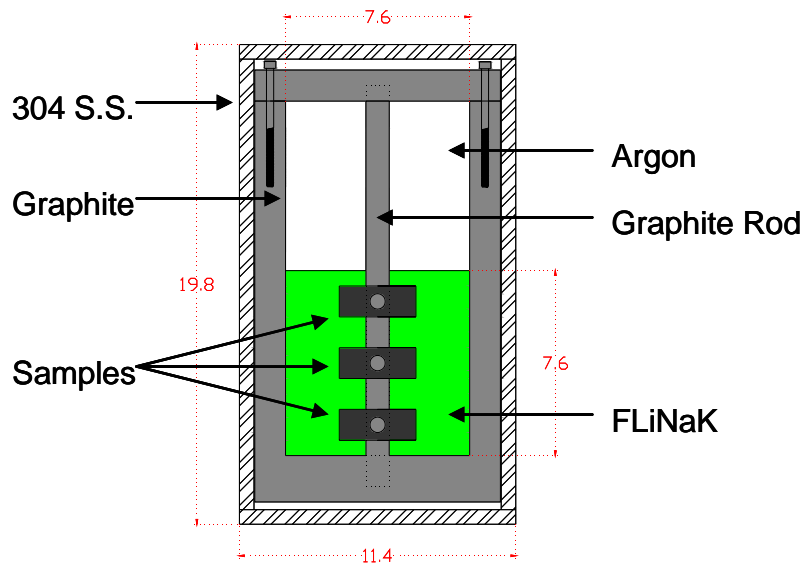
Figure 4. Schematic illustration of the corrosion capsule apparatus used for testing corrosion performance of various alloys in molten FLiNaK salt at 850°C. Dimensions are in inches.

3.c. Procedure for Preparation of Corrosion Test Capsules

A number of graphite crucibles, central sample rods and the graphite set screws were machined from POCO graphite blocks and ultrasonically cleaned in methanol and water. They were then baked at 1000°C in the atmosphere-controlled furnace to remove moisture. Three samples of a given alloy were then fixtured to the central graphite sample rod using graphite set screws. The graphite crucible, central sample fixturing rod and test samples are shown in Figure 5. A graphite lid was used to cover the crucible and was secured with set-screws. The graphite crucibles were then placed in the 304 stainless steel

capsules and the tops were welded shut as shown in Figure 6. Three 1/8 inch pieces of tubing were used to keep the holes aligned for introducing the salt into the corrosion capsules.

(a)

(b)

(c)

(d)
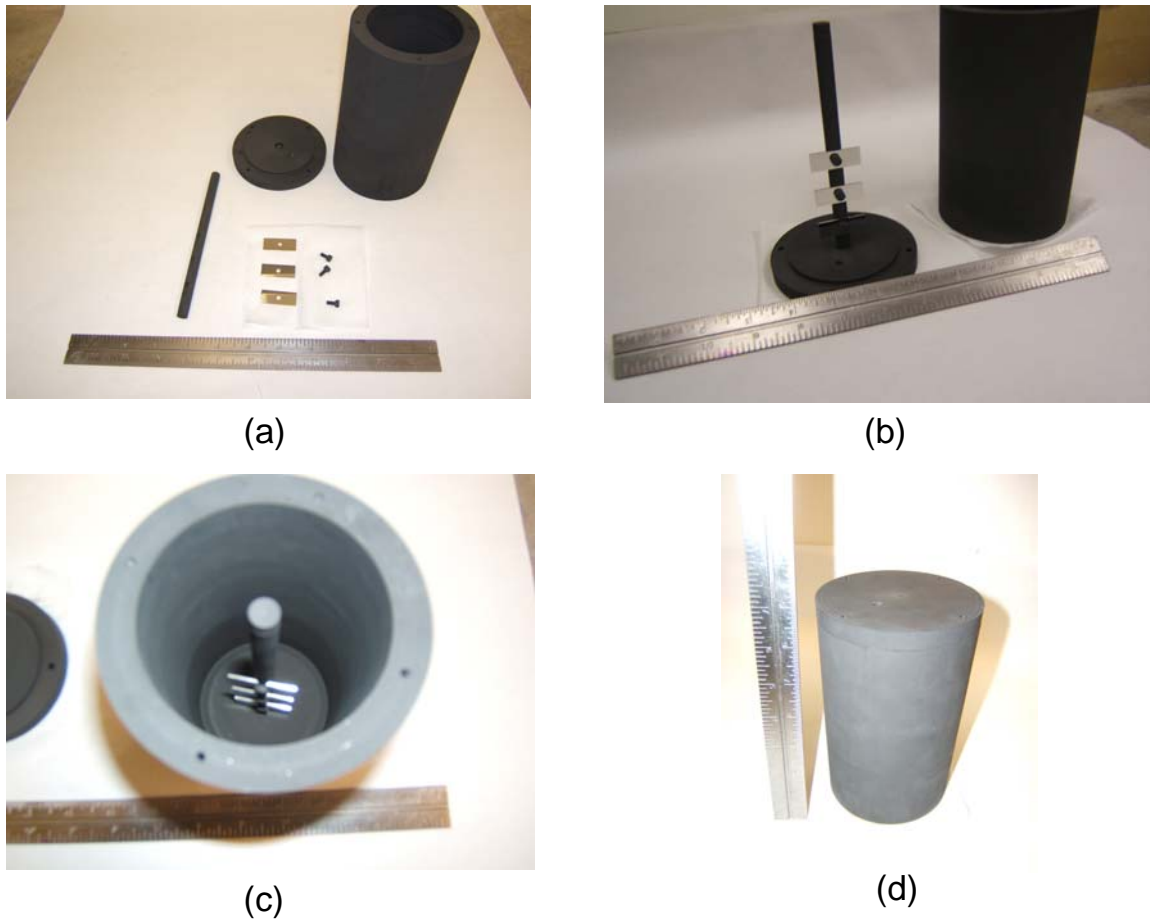
Figure 5. Photographs showing a finished graphite crucible and other parts: (a) graphite pieces for one crucible and alloy samples, (b) alloy samples attached to central graphite rod to be inserted upside down into lid, (c) alloy samples and sample rod inserted into graphite crucible, and (d) graphite crucible, ready for lid to be screwed shut.
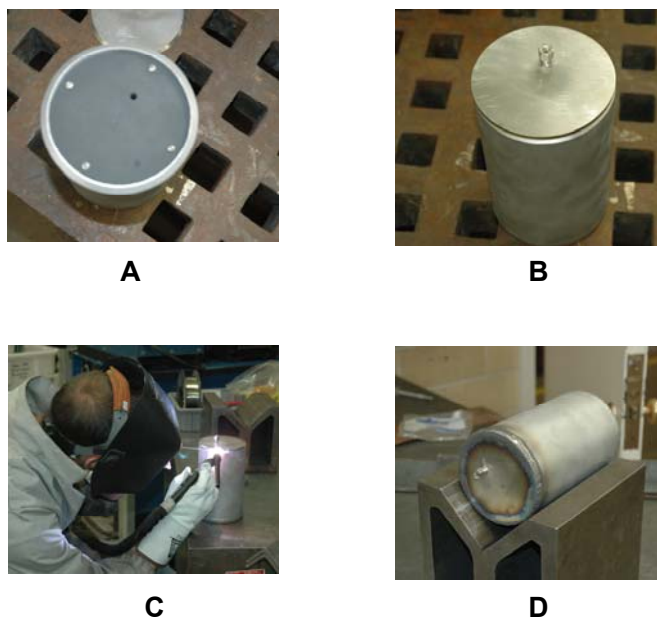
Figure 6. Steps involved in the encapsulation of the graphite corrosion capsules: A) the graphite capsule inserted into the stainless steel capsule, B) the stainless steel lid situated on the capsule wall with the 1/8" guide tube inserted, C) the initial welding, and D) the finished corrosion capsule ready for storage under vacuum.

After the containment vessel was welded shut, the capsules were placed in the antechamber of the glove-box and the atmosphere inside was evacuated. The capsules were kept under vacuum in the ante-chamber, or in the glove-box, until they were filled with salt and sealed.

The salt obtained from ECS was transferred from the nickel vessel to the corrosion capsule by a 304 stainless steel transfer line in a glove box, as shown in Figure 7 and 8. The glove box has several penetrations welded into it for instrumentation. It was leak tested and shown to provide an adequate air boundary. In addition, it was shown to remove moisture to at least 6ppm with all the equipment in it. This low moisture level was achieved by first flushing the glove box and then allowing the "dry-train" to run for several days. The glove box heat exchanger was shown to work with the capsule heater at temperatures near 1000°C for extended periods. During this time the internal glove box temperature was held at or below 30°C. In addition, the glove box is installed with an oxygen sensor procured from Alpha Omega Instruments capable of measuring oxygen levels of 1-1000ppm.

In order to transfer the salt, the system was pre-heated. The nickel vessel was heated to 600°C, the transfer line to 500°C, and the corrosion capsule to 500°C. A dry stream of argon gas pressurized the nickel vessel forcing the salt to flow through the transfer line to the corrosion capsule. The amount of salt transferred to the corrosion capsule was measured with a scale located under the capsule heater. The optimum amount of salt to be transferred was 0.7 kg. After the mass of salt transferred reached 0.65 kg, argon was pressurized through the transfer line to remove any salt in the transfer line. This brought the mass of salt inside the corrosion cell to approximately 0.70 kg. The transfer line was removed from the corrosion capsule and the capsule was sealed at 600°C. For INL salt, salt addition was made directly to the capsule as solid pieces inside the glove box. The capsule was then heated to 600°C and welded shut.
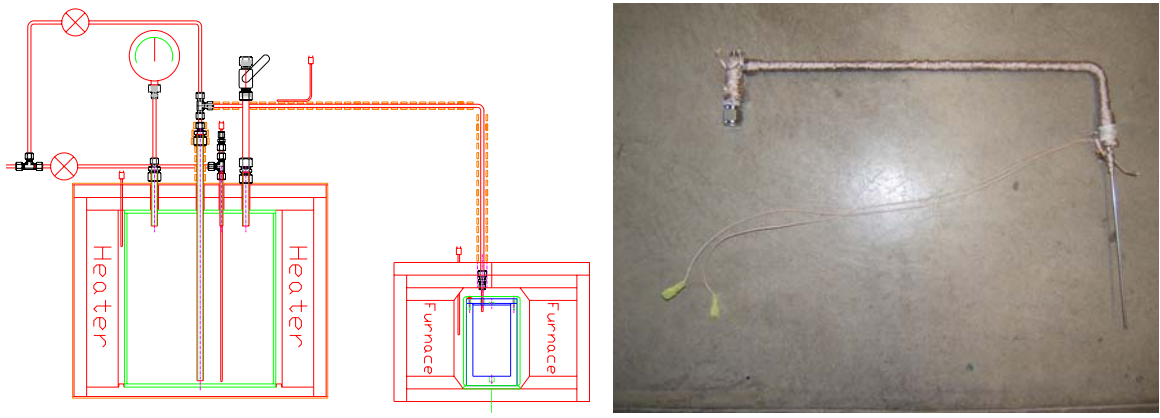
Figure 7. FLiNaK transfer apparatus and transfer tubing for transferring the ECS molten FLiNaK salt into the corrosion test capsule.
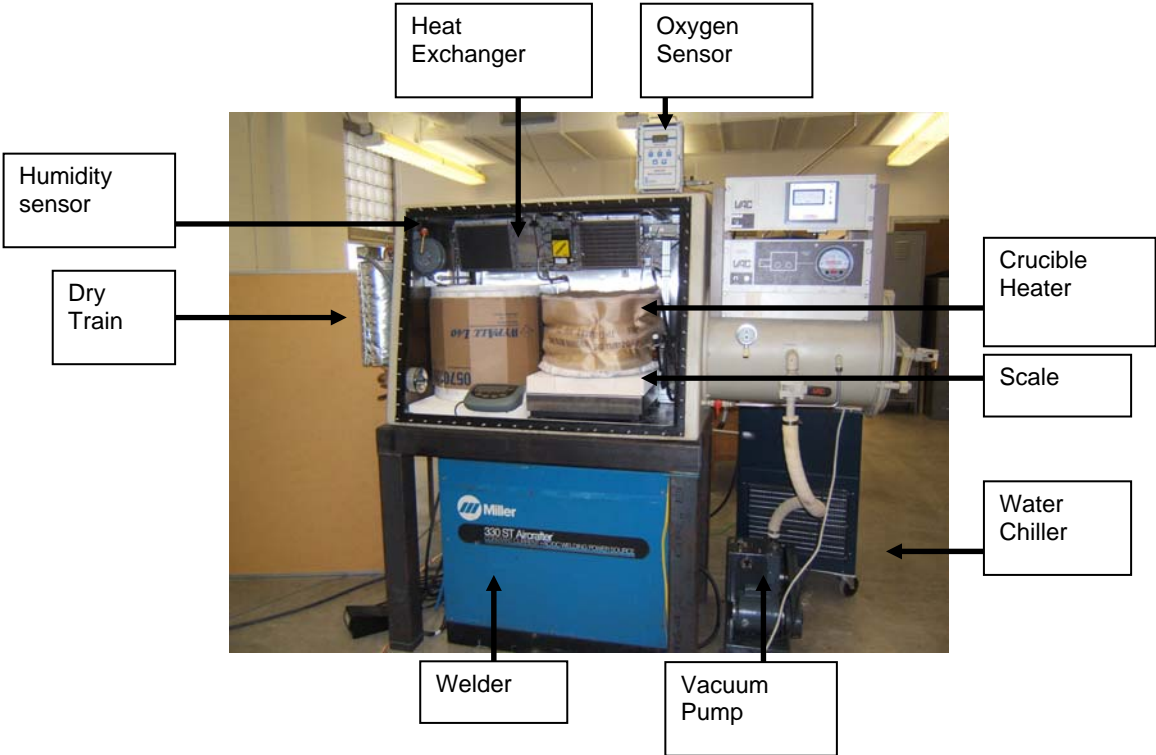
Figure 8. Interior of glove-box where several key components of the molten salt transfer system are visible. The melt heater on the left and the capsule heater on the right. The glove-box heat-exchanger is visible on the top portion of the photo. FLiNaK salt is in the heater on the left.

The sealed capsules were removed from the glove box and placed in a high temperature furnace for corrosion tests. Four capsules were placed in the high temperature furnace for each run as shown in Figure 9. The furnace was ramped to 850°C at a known rate and held at that temperature for 500 hours. Following this, the furnace was cooled to 500°C, and the capsules were inverted to allow the salt to drain away from the corrosion samples as shown in Figure 10. The capsules were then placed back in the furnace and the system was cooled to room temperature.

Figure 9. The crucibles to be tested were placed in the argon atmosphere furnace, which was heated to 850°C.

Figure 10. The corrosion capsules were inverted at 500°C after testing at 850°C for 500 hours.

After the completion of the tests, the bottom sections of the corrosion capsules were removed using an automated mill in two steps, involving first cutting through the stainless steel canisters, and then cutting through the graphite. Subsequently, the samples were detached from the rods as shown in Figure 11. Following the initial weighing, the samples were cleaned in three steps as mentioned below. After the samples had dried, they were weighed a second time before being placed in a desiccator before further analysis.
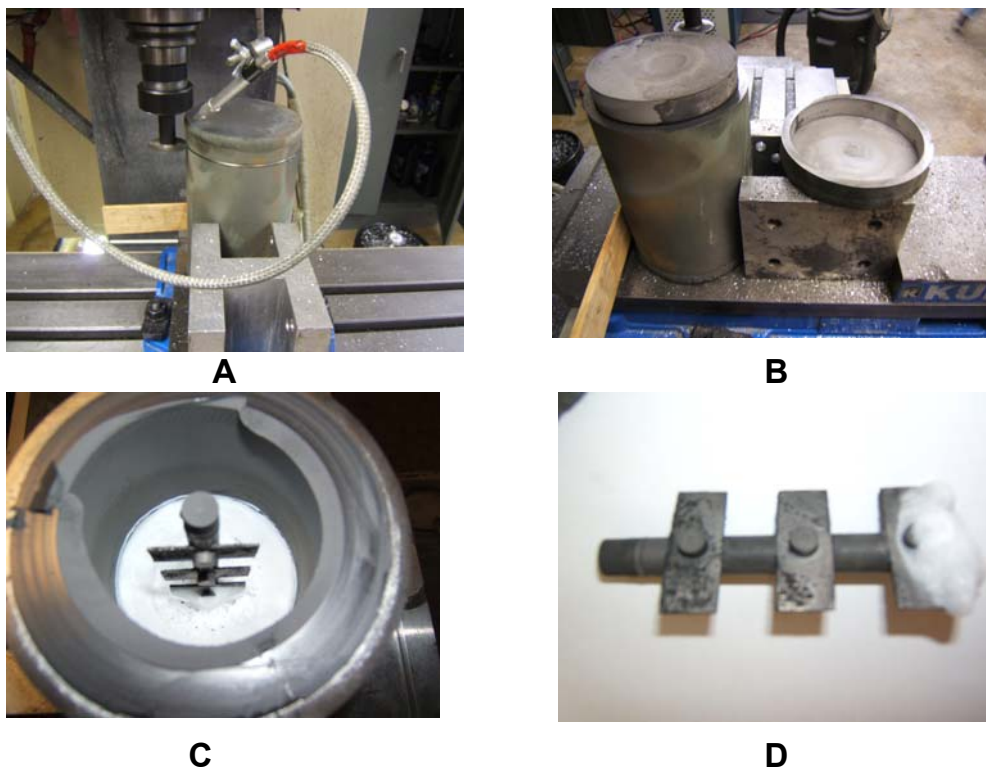
Figure 11. Cutting open the corrosion capsule. A) initial cutting of the stainless steel capsule, B) cutting of the graphite capsule, C) corrosion capsule after the stainless steel and graphite bottoms were removed, and D) the section of graphite rod with the samples still fixtured.

3.d. Salt Removal from Test Samples

Despite inverting the corrosion capsules at 500°C and allowing the molten FLiNaK salt to drain away from the samples, it was believed that some salt might have been stuck to the samples upon cooling. Even though the amount that would stick to the samples would likely be small, it would still be enough to provide an unknown amount of error in the weight loss measurements. A variety of tests were undertaken to establish a salt removal procedure. The options tested included cleaning test samples in a variety of liquids ultrasonically and dipping the samples in a separate water-soluble molten salts. A technique used by Russian researchers to clean FLiBe salt showed the desired result. This technique involves washing the samples in a 1M solution of aluminum nitrate, $Al(NO_3)_3$, which is a good solvent for lithium fluoride, followed by washing in distilled water and alcohol [13]. Specifically, the samples were cleaned in 1 M $Al(NO_3)_3$ in two separate steps five minutes each, followed by ultrasonic cleaning in distilled water for five minutes, and finally for five minutes ultrasonically in acetone (Figure 12).

Figure 12. Removal of solidified salt from test samples using 1 M Al(NO₃)₃.

3.e. Problems Encountered and How They Were Overcome

Several experimental issues were encountered, but were successfully overcome. The thermocouple probes as well as heating elements of the argon atmosphere furnace had to be replaced. The graphite crucibles were re-machined to give an extra 0.060" clearance between the outside of the graphite capsules and the stainless steel capsules. The salt transfer tube from the ECS nickel vessel to the corrosion capsule had to be redesigned to minimize salt solidification in the line.

During testing of the newly acquired high temperature furnace, it became obvious that it was not operating to specifications. Upon removal of the retort, it was clear that some of the heating elements had failed as shown in Figure 13. The furnace was subsequently repaired and used successfully. The cloth covered thermocouples in the box furnace were replaced with stainless steel clad Type K thermocouples (Figure 14). A graphite tray was placed at the base of the furnace as shown in Figure 15, as a contingency in the event of a capsule failure.

Figure 13. Some heating elements in the high temperature furnace failed and had to be replaced and the furnace was subsequently operated satisfactorily.
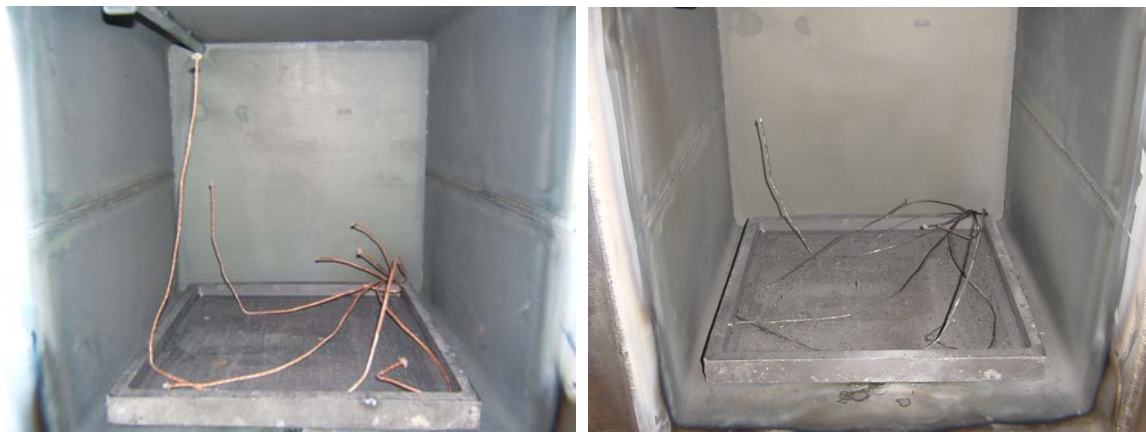
Figure 14. Initial calibration thermocouples.

Figure 15. Photograph of the argon atmosphere furnace showing thermocouples and graphite spill tray.

Problems were encountered with FLiNaK freezing in the transfer line from the reservoir to the corrosion capsules. The initial transfer tube seen in Figure 16A used a single tape heater to maintain the tube at 500°C. The original transfer tube was built from stainless steel tubing that was swaged to the nickel container with a ½" to ¼" coupler that was in turn swaged to a ¼" T-coupler. The T-coupler allowed for a gas stream to be connected to the transfer tube at the top. The gas was then used for clearing the tube of FLiNaK. Another ¼" stainless steel tube was connected to the T-coupler. This stainless steel tube transferred the FLiNaK to the corrosion capsules. Just prior to entering the corrosion capsules, the ¼" tube was reduced to a 1/8" stainless steel tube by a coupler. The 1/8" stainless steel tube was inserted into the corrosion capsule. FLiNaK would freeze in the T-swage connecting the blow-out line with the 1/2" nickel tubing from the reservoir and the transfer tube, as well as in the blow-out line and 1/8" spout. Several redesigns of the transfer line progressed before one that would work for several fillings was found. The best design of the transfer tube was constructed according to the following procedure. First, three k-type thermocouples were tack welded to the tubing. Next, the tube was wrapped

in glass-fiber electrical tape to prevent electrical current from the wrap heaters interfering with the thermocouples should a heating tape fail. Finally, three separate heating tapes were wrapped around the tubing and covered in insulation as shown in Figure 16.
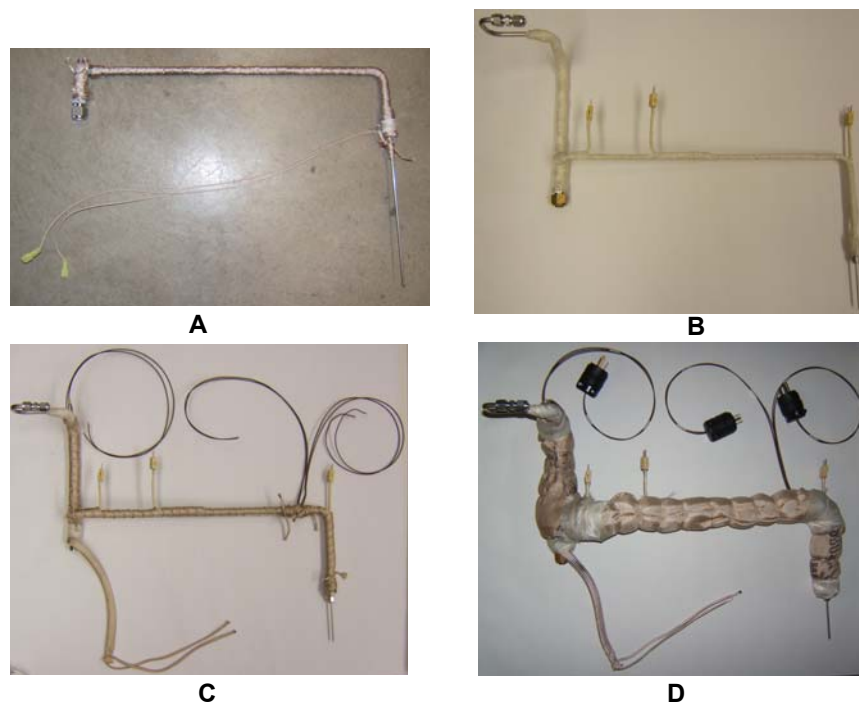
Figure 16. FLiNaK transfer tube design: A) the initial heating tape design, B) the transfer tube after it had thermocouples tack welded on and had been wrapped in fiber tape for electrical insulation, C) the transfer tube after it had the three tape heaters wrapped around it, and D) the finished transfer tube after it had been insulated with Kaowool and a fiber cloth and electrical connections attached to the heating tape leads.

3.f. Initial Dry Runs to Establish Capsule Integrity

An important consideration in the design of the corrosion cell was the mechanical stability of the outer stainless steel capsule that constitutes the boundary between the molten salt and the furnace atmosphere. This is critical from the standpoints of safety and contamination of the molten salt that can influence the corrosion test results. The stainless steel capsule was made from three separate 304L stainless steel pieces, a 4" in diameter, 7" length, and 0.237" thickness and two end caps, ¼" in thickness. Welding was performed using five TIG passes using ER 308L, 0.0625" diameter filler rod. To allow for the contraction of air during cooling a small gap was left open which was eventually filled by the same method after cooling. The stainless steel capsule was then heated to 1000°C and held at this temperature for 500 hours. At these temperatures for this long of a duration, the metal capsule would be close to its creep rupture point. It was noted that, despite considerable oxidation of the surface, the stainless steel capsule maintained its integrity in that there were no obvious cracks in the welds or in the cylindrical sections of the capsule or apparent yielding of the end-caps or the cylinder walls. Figure 17 shows a photograph of the stainless steel capsule after exposure at 1000°C for 500 hours, in air.

Figure 17. **Photograph of the oxidized stainless steel capsule after exposure at 1000°C for 500 hours, in air.**

To examine the presence and penetration of cracks in detail, the weld region was sectioned, mounted, polished, and then examined under a scanning electron microscope (Figure 18). Maximum crack length was identified to be 1500μm and the oxide layer on the inner surface was about 20μm. The total wall thickness prior to the test was 6020μm (0.237").

(a)   (b)
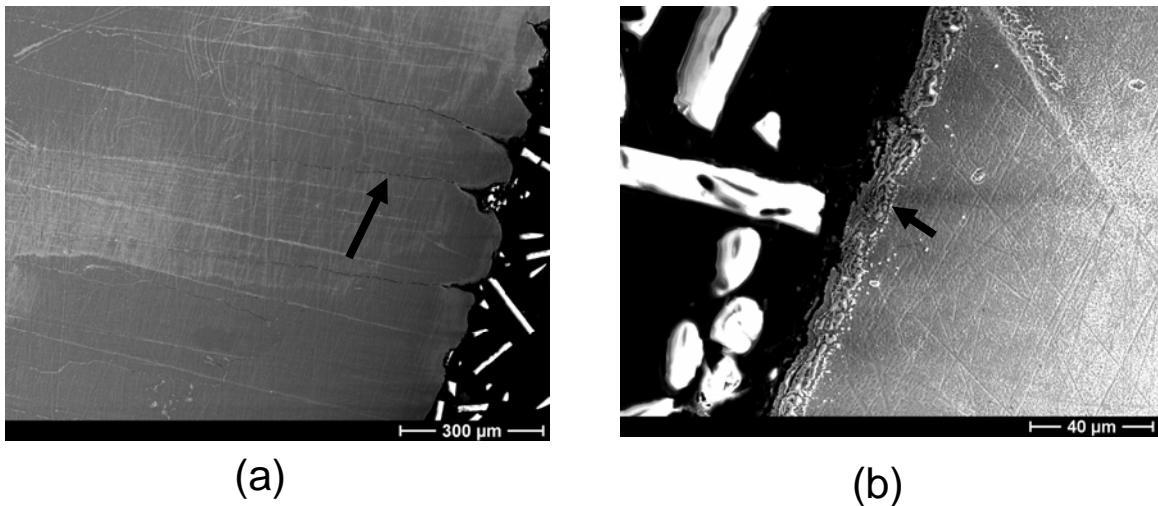
Figure 18. SEM images of (a) cracks emanating from the outer side of the stainless steel capsule (maximum crack length was measured at 1500μm) and (b) oxide layer on the inner surface.

3. g. Examples of Stress and Temperature Calculations

A number of calculations have been performed to ensure the reliability and success of the initial experiments. This has included, estimation of internal stresses on the corrosion capsule at temperatures of up to 1000°C under varying pressures, necessary thickness of the stainless steel outer casing, salt volume calculations to ensure complete immersion of samples, and heat transfer calculations for estimation of salt temperature during temperature ramp-up. Figure 19 shows an example of the calculations for hoop stress (outer atmospheric pressure minus the internal pressure) of the outer stainless steel containment as function of temperature assuming that an initial vacuum of 1/5 atmosphere is created in the containment. Our calculations for the salt requirements to ensure complete immersion of samples upon melting indicate that about 0.63 kg would be required per crucible test, but since the scale that is being used is accurate to within 0.1kg; 0.7kg will be used. Figure 20 shows Finite Element Heat Transfer (FEHT) simulations of the temperature profiles of the outer wall of the corrosion cell and the salt during temperature ramp-up.
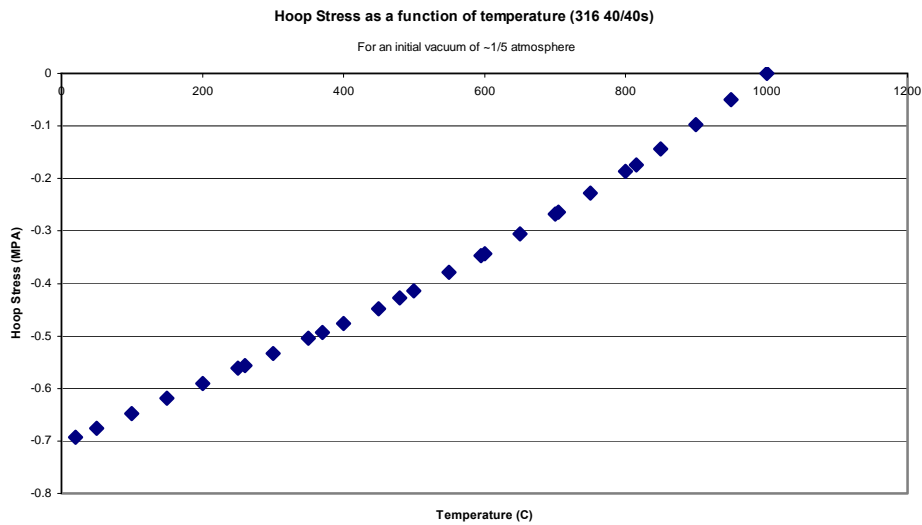
Figure 19. Calculation of Hoop stress up to 1000°C for stainless steel outer containment, assuming the containment is evacuated to 1/5 atmosphere.
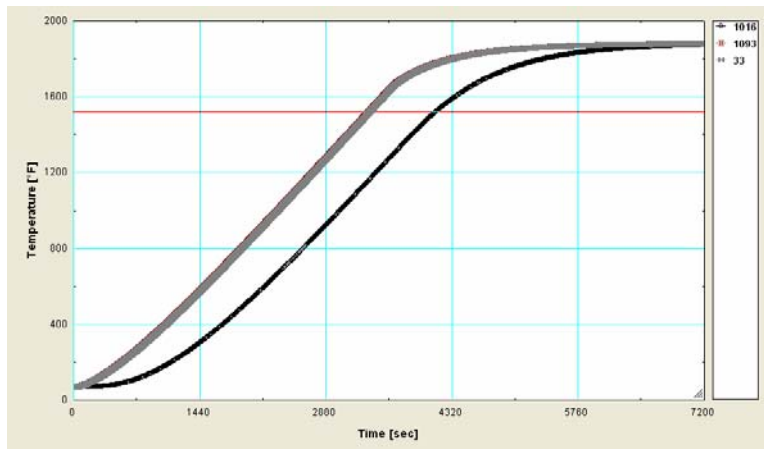
Figure 20. Finite Element Heat Transfer (FEHT) simulations showing the temperature of the outer walls of the containment and the salt during temperature ramp-up.

24

4. MATERIALS CORROSION TESTING AND ANALYSIS

4.a. Candidate Alloys for Corrosion Testing

Six candidate alloys were selected for initial screening based on their code-certification status, high temperature strength, air oxidation resistance, and prior experience in other molten salt research programs. Hastelloy-N, Hastelloy-X, Haynes-230, Incoloy-800H, Ni-201, and Nb-1Zr were selected from an initial list of potential alloys under consideration for construction of a molten salt heat transfer loop [6]. Additionally, Incoloy-800H, Hastelloy-N, Haynes-230, and Hastelloy-X are code certified for use in specific high temperature environments and have been identified as potential candidate materials for the Advanced High Temperature Reactor (AHTR) concept [14]. Hastelloy-N was developed at Oak Ridge National Laboratories (ORNL) for use in fluoride salts under the MSRE program [12]. Hastelloy-N has superior compatibility with the molten fluoride salt-graphite system for temperatures up to 650°C [15]. Nickel-201 was included because nickel is very resistant to thermodynamic dissolution in molten fluoride salts.

In year two, an additional material namely Ni-electroplated Incoloy 800H alloy was added to the list of materials to be tested. Incoloy 800H samples were polished up to 600 grit surface finish and sent to Southwest United Industries Inc. in Tulsa, Oklahoma, where they were electroplated using the sulfamate nickel coating process. Table 2 lists the nominal compositions of the alloys selected for the corrosion study and Table 3 lists criteria for selection of these alloys.

Figure 21 shows the yield strength of these alloys as a function of temperature. It is obvious that nickel-200 is not practical as a structural material and that Nb-1Zr, while being weak in comparison to the nickel-base and iron-nickel-base alloys at low temperatures, is stronger at high temperatures. Additionally, the nickel-base alloys have a superior high temperature strength compared to iron-nickel based alloys.

Table 2. Materials tested for corrosion in molten FLiNaK at 850°C for 500 hours.

Alloy	Cr	Mo	W	Al	Ti	Fe	C	Co	Ni	Mn	Nb	Zr	0.2%YS (MPa) @850C	UTS (MPa) @850C
Haynes-230	22.5	1.2	14.1	0.3		1.8	0.1	0.3	59	0.5			251	352
Hastelloy-N	6.31	16.1	0.06	<.01	<.01	4.03	.03	.15	72.2	0.53		<.01	196	339
Hastelloy-X	21.3	8.8	0.4			19.3	.06	1.4	47.5	.54			193	286
Nb-1Zr											99.05	0.95	186	221
Incoloy-800H	20.4			0.5	0.6	42.3	.07		31.6	0.8			102	129
Ni-201					.02	.05	.02	.02	99.4	.19			18	65
Nickel-Plated Incoloy-800H														

Table 3. Alloys for the first phase of corrosion testing [16, 17].

Alloy	Comments
Ni-based	
Hastelloy-N	Tested in ORNL molten salt loop; provides a good reference point; contains ~6% Cr; code-certified for use up to about 700°C
Hastelloy-X	Recommended for usage up to 900°C; high Cr content (~20%); poor air corrosion resistance; code-certified
Haynes-230	Contains ~10% tungsten, can be used up to 1000°C; high Co content (~10%); high Cr content (~20%); marginal air corrosion resistance; code-certified
Fe-based	
Incoloy-800H	Recommended for usage up to 1000°C, long history of high temperature usage, easy to fabricate, high Cr content, poor air corrosion resistance; code-certified
Nb-based	
Nb-1Zr	Nb-based alloys have been identified for high temperature applications and have favorable fabricability. Nb-1Zr has also been identified for use on the hydrogen iodide side of a high-temp HX; Nb alloys such as Nb-5Ta or Nb-10%Hf may also be good potential alloys.

Ultimate Tensile Stress as a Function of Temperature
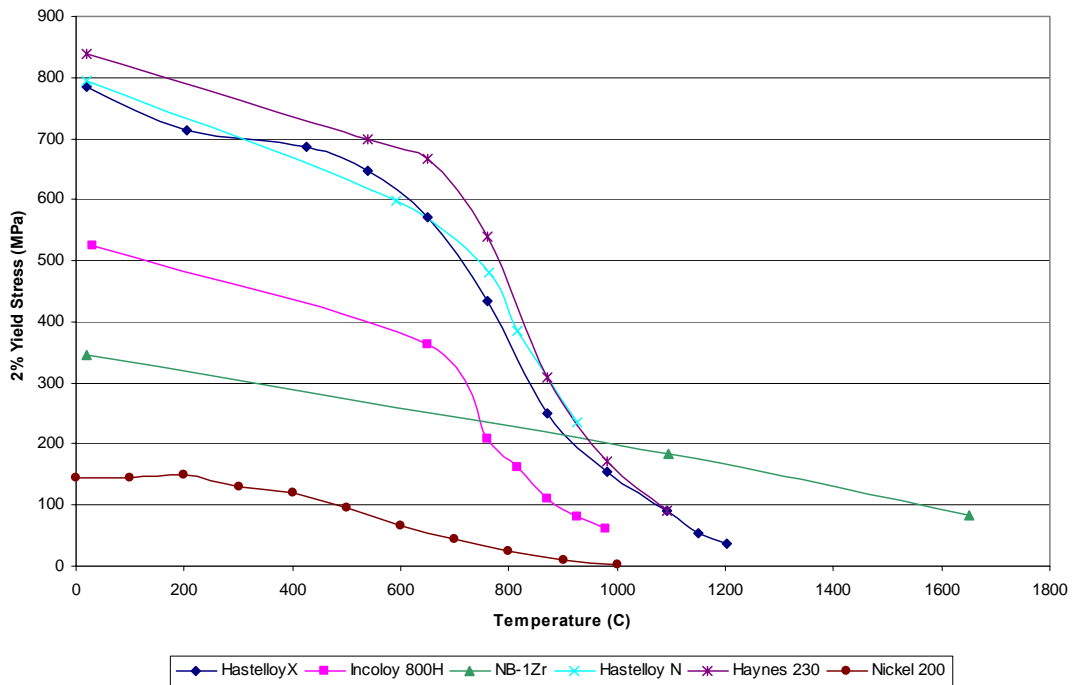
Figure 21. Yield stress of alloys as a function of temperature.

4.b. Test Samples

Sheet stocks of six alloys were procured after a national survey of vendors and cut into rectangular test strips (1.25" length, 0.5" width). A hole was drilled in the center for fixturing to the central graphite rod. The alloy samples were ground progressively with finer grits of silicon carbide grit paper metallographically polished with a one micron diamond paste to a mirror-like finish, in order to facilitate accurate post-corrosion-testing materials analysis. Figure 22 shows the dimensions and photograph of the samples that were used for high temperature corrosion tests in molten FLiNaK.
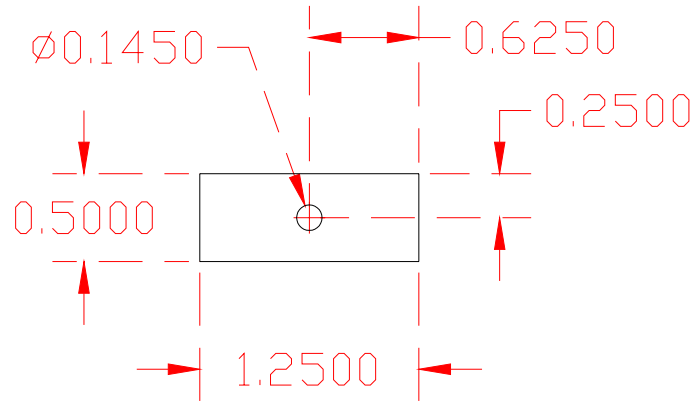
(a)
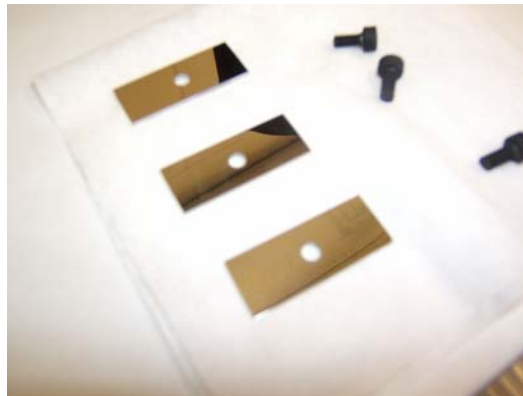
(b)

Figure 22. (a) Dimensions of the test samples and (b) photograph of the test samples.

4. c. Results of Corrosion testing and Analysis

Figure 23 shows a summary of the weight loss measurements (per unit area) for all the samples tested. For the three Ni-based alloys, Haynes-230, Hastelloy-N, and Hastelloy-X the weight loss correlates inversely with the Cr content of the alloy. The weight change measurements for Incoloy-800H samples tested in hydrofluorinated ECS FLiNaK salt and non-hydrofluorinated INL FLiNaK salt were comparable indicating that under the conditions tested, the additional impurity content in the non-hydrofluorinated salt did not have a significant influence on corrosion performance. The Ni-rich Ni-201 alloy and Ni-electroplated Incoloy-800H samples performed exceptionally well due to the strong dissolution resistance of Ni in molten fluoride salts. The Nb-1Zr alloy exhibited extremely high rate of dissolution implying that this alloy may be unsuitable for use in molten fluoride salts.
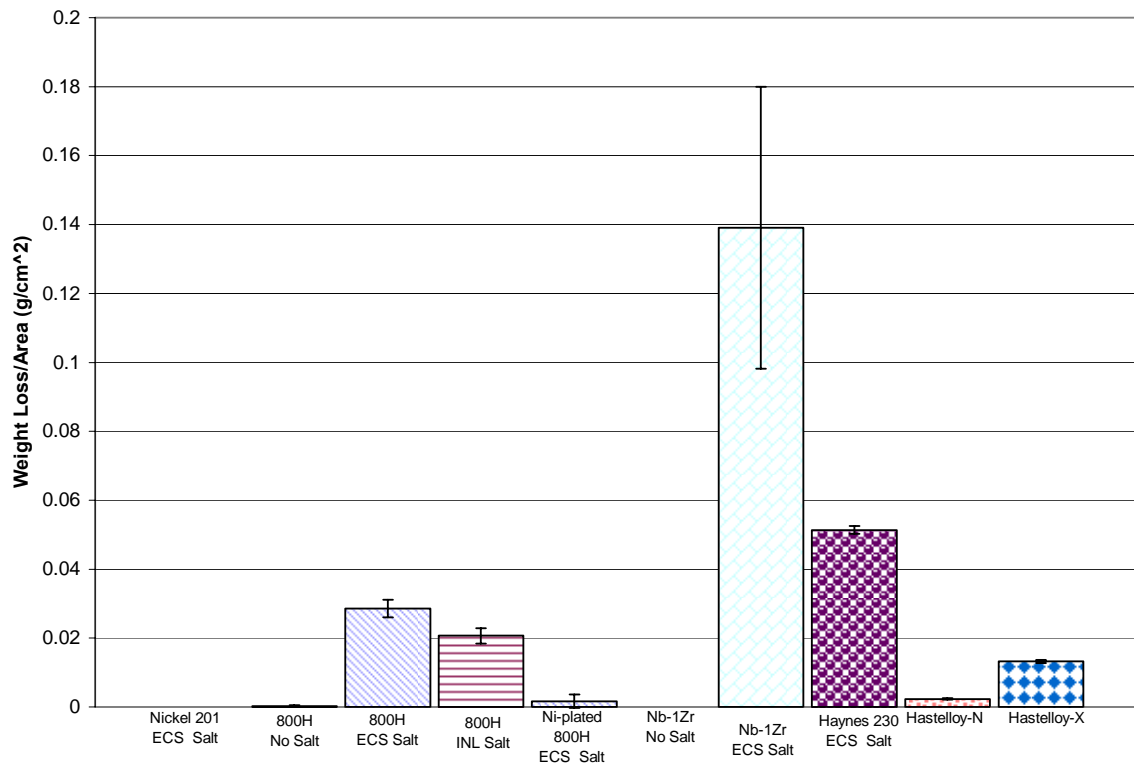
Figure 23. Results of weight-loss for various materials after exposure to FLiNaK at 850°C for 500 hours.

Figure 24 shows the SEM plan and cross-sectional views of Hastelloy-N (5%Cr), Hastelloy-X (20% Cr), and Haynes 230 (23% Cr) after molten salt exposures. All three alloys exhibited significant grain boundary attack and the extent of the corrosion attack was proportional to the Cr-content of the alloy. EDS elemental maps showed that grain boundaries in these alloys act as conduits for Cr diffusion in these alloys to their surface and into the salt. Figure 25 shows SEM EDS analysis of Hastelloy-X and indicates considerable enrichment of Mo at the grain boundaries and these Mo phases (at the grain boundaries as well as in the grains) were resistant to dissolution. Likewise, as shown in Figure 26, for Haynes 230 alloy W enrichment was observed at the grain boundaries, and the outermost layer after corrosion consisted predominantly of a Ni-rich layer. This also appears to indicate that W-rich phases are resistant to dissolution in molten salt.

28
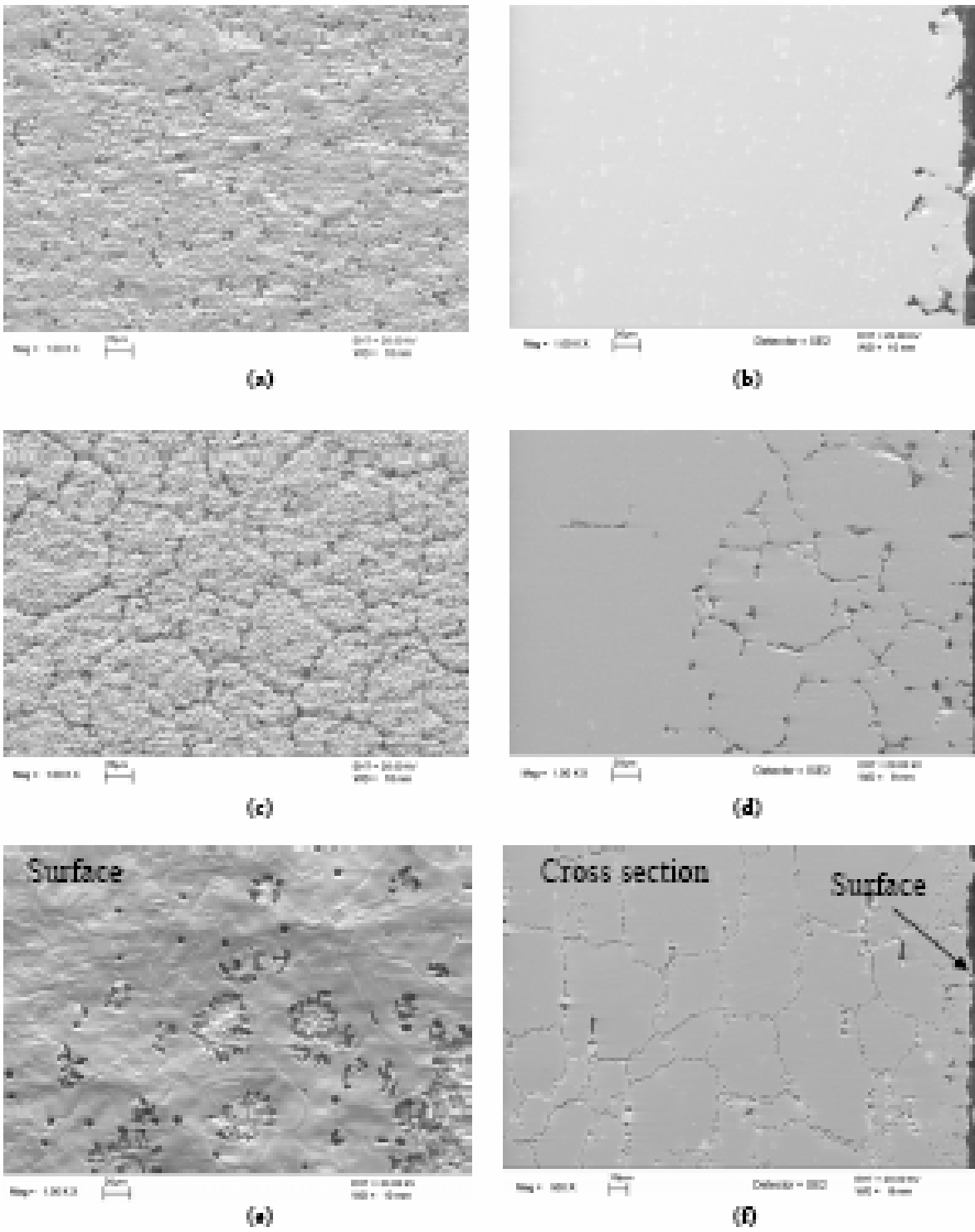
Figure 24. SEM plan and cross-sectional images of alloys (a) and (b) Hastelloy-N, (c) and (d) Hastelloy-X, and (e) and (f) Haynes 230, after exposure to molten salt at 850°C for 500 hours.
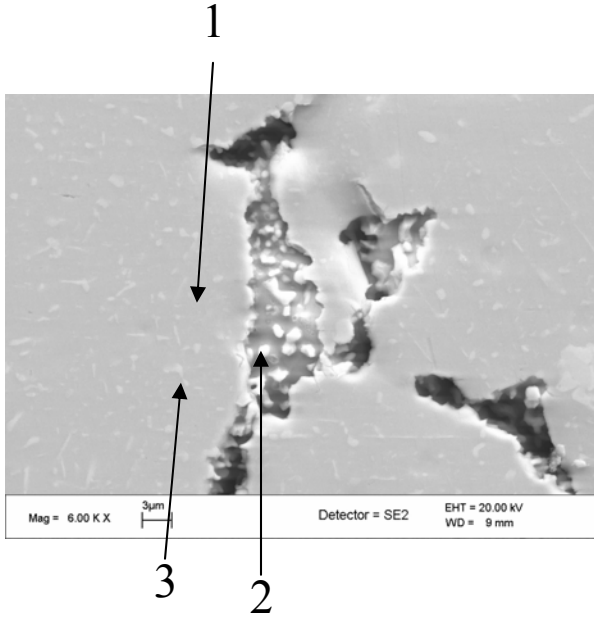
	Cr	Fe	Ni	Mo
Point 1	**5.05**	**26.4**	**59.45**	**4.38**
Point 2	**0.74**	**7.94**	**36.32**	**42.9**
Point 3	**7.04**	**11.0**	**36.08**	**37.8**
Hastelloy-X	**21.34**	**19.3**	**47.53**	**8.76**

Figure 25. SEM-EDS analysis of Mo-containing Hastelloy-X sample after exposure to molten salt at 850°C for 500 hours. Point 1 represents the alloy matrix, Point 2 represents a molybdenum enriched region on the grain boundary, Point 3 represents a molybdenum enriched region in the grain.
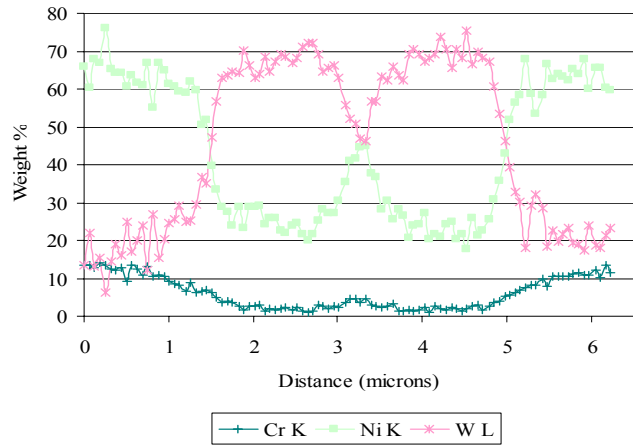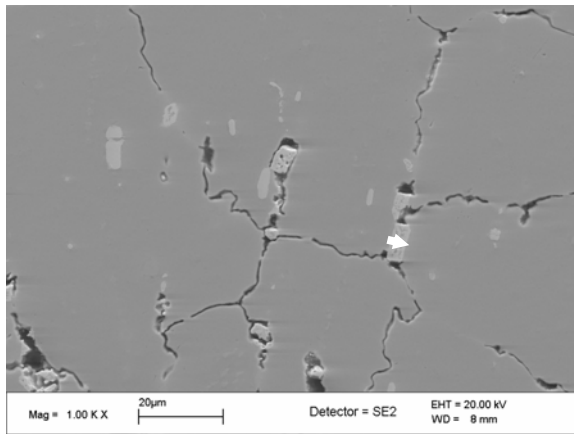
Figure 26. SEM-EDS analysis of W-containing Haynes 230 sample after exposure to molten salt at 850°C for 500 hours, showing that W-rich phases are generally resistant to dissolution in molten salt.

Figure 27. Photographs of Nb-1Zr alloy of the after exposure to molten salt at 850C for 500 hours, showing sever corrosion and embrittlement.

Figure 27 show the photographs of the Nb-1Zr alloy after exposure to molten salt. This alloy exhibited severe corrosion and brittleness. This is supported by the large corrosion weight loss for this alloy shown in Figure 23. The severe attack and brittleness observed in this alloy implies that it may be generally unsuitable for use in molten fluoride salts at temperatures of 850°C or higher. Formation of carbide phases as a result of interaction with graphite may also have caused this extreme brittleness. Figure 28 shows the SEM plan and cross-sectional views of Ni-201 alloy after exposure to molten salt. This nearly-pure Ni alloy exhibits negligible corrosion except for the minor grain boundary attack observed in the plan view.
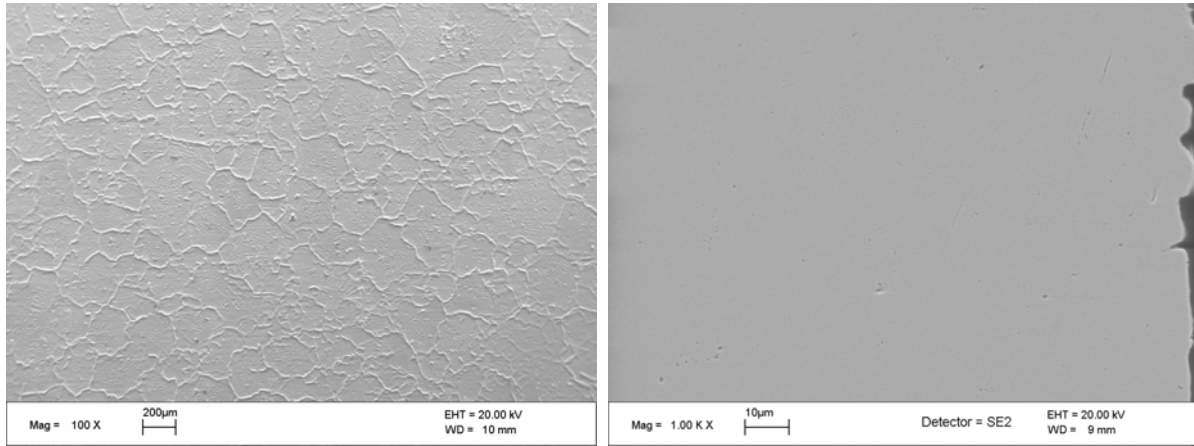
(a)   (b)

Figure 28. SEM images of Ni-201 alloy after exposure to molten FLiNaK salt at 850°C for 500 hours (a) plan view and (b) cross-sectional view.

Figure 29 shows the cross-sectional SEM image of the Ni-electroplated 800H alloy after the corrosion tests. The alloy was quite resistant to dissolution in molten FLiNaK. However, EDS analysis across the Ni plating showed that Fe and Cr from the alloy had diffused through the plating and into the salt. Some porosity seems to have evolved in the Ni electroplating due to Kirkendall effect during this diffusion. It should be noted here that Ni electroplating tested was not optimal from the standpoint of minimizing the diffusion of Fe and Cr. Coating densification and microstructural modification may minimize the diffusion of Fe and Cr across the electroplated Ni. Ni-electroplating can be applied economically on the inner surfaces of tubes, and therefore this could be considerable interest to the NGNP.
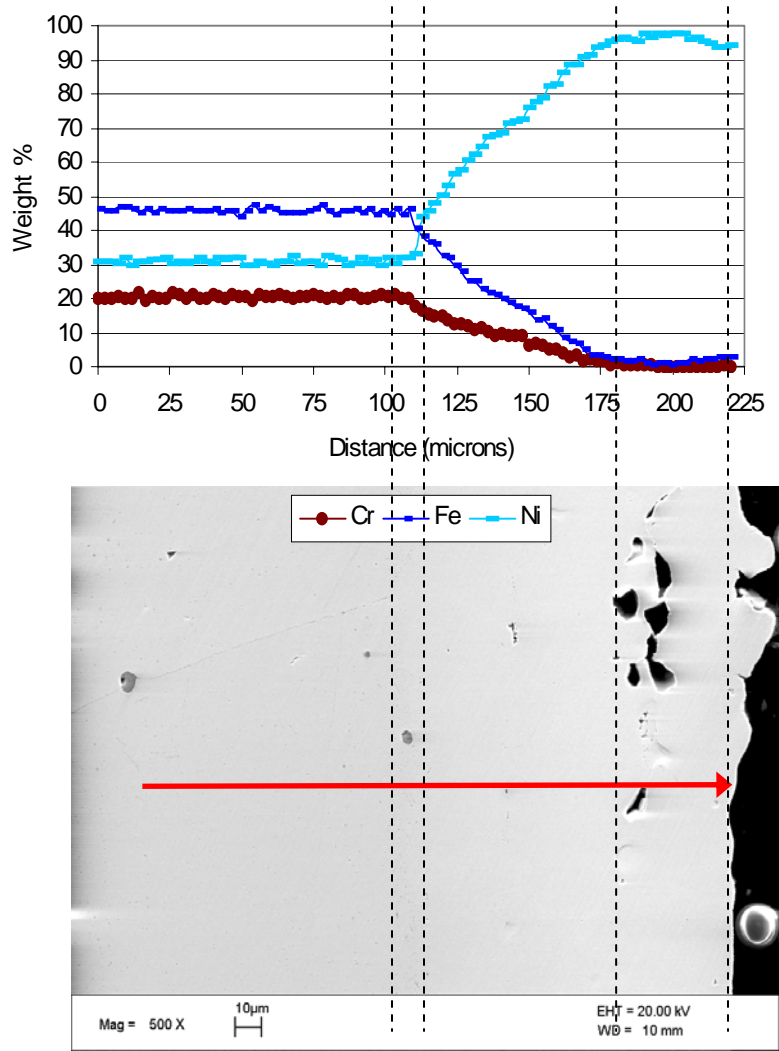
Figure 29. Cross-sectional SEM image (below) and EDS analysis (top) for the Ni-electroplated Incoloy 800H after exposure to molten salt at 850°C for 500 hours .

4,d. Salt Analysis

FLiNaK salt samples in the as-received condition as well as those taken from all the corrosion capsules were analyzed at the Soil Sciences Laboratory at the University of Wisconsin, Madison for heavy metal and other impurities using the ICP-MS technique. An example of this is shown in Table 4 for pre-corrosion samples of the salt obtained from INL.

Table 4. Analysis of INL FLiNaK salt. TC, TS, and TN stand for total carbon, total sulfur, and total nitrogen respectively.

TOTAL MINERALS (ppm)												
Sample	P	K	Ca	Mg	S	Zn	B	Mn	Fe	Cu	Al	Na
1	<39	400271	22	<6	<39	1.1	4	0.7	16	6	<39	63192

HEAVY METALS (ppm)								
Sample	Cd	Co	Mo	Ni	Pb	Li	Si	Ba	Sr
1	<3	<2	<3	<2	<16	74412	4538	<0.2	3.8

ICP-MS (ppm)										
Sample	Ti	V	Cr	Co	Ni	Zr	Nb	Mo	La	Hf	W
1	9.92	17.56	2.95	0.012	<0.08	1.69	0.39	0.22	0.52	0.34	<0.02

Ion Chromatography (%)		
Sample	F	Cl⁻	SO_4
1	39.30	0.84	ND*

*Not detected

Other (%)			
Sample	H_2O	TC	TS	TN
1	0.4	0.04	<0.01	0.02

Initial results for chromium content from the heavy metals analysis is shown in Table 5. The amount of chromium in the salt was determined by ICP-MS analysis. Figure 30 shows the Cr-content of the salt after corrosion testing as a function of the Cr content of the alloy that was tested in that particular salt. The amount of chromium in the salt correlated approximately to the amount of chromium in the alloy. The presence of Cr in the salt used for testing Ni electroplated Incoloy 800H indicates that the Cr permeated from the base metal through the Ni plating.

Table 5. Chromium content in ECS FLiNaK salt as obtained by ICP-MS analysis, after corrosion tests of various materials at 850°C for 500 hours.

Test Alloy	Initial Alloy Weight % Cr	Cr in Salt sample (ppm)
Incoloy-800H	20.4	154.54
Incoloy-800H (INL salt)	20.4	144.71
Ni-Plated Incoloy-800H	*	14.39
Haynes-230	22.5	79.61
Hastelloy-N	6.3	27.19
Hastelloy-X	21.3	63.92
Ni-201	--	1.31
Nb-1Zr	--	0.65
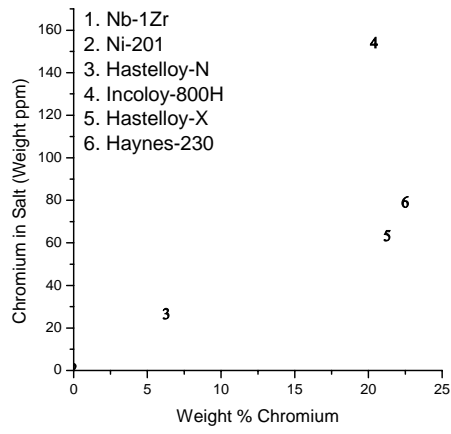
Figure 30. Cr content of the salt (as determined by ICP-MS technique) as a function of the Cr content of the test alloy.

4.e. Results from Air Oxidation Tests

Air oxidation tests were undertaken for all alloys tested and the nickel-plated Incoloy-800H samples. The results of the atmosphere oxidation tests are shown in Figure 31. The Nb-1Zr alloy suffered severe oxidation further confirming the unsuitability of this alloy for the heat exchanger application. The high Cr Ni-based superalloys performed exceptionally well, followed in performance by Incoloy-800H and Ni-electroplated Incoloy 800H. The Ni plating reduced the oxidation resistance of Incoloy 800H. However, if Ni were plated on an alloy with significant air oxidation resistance (e.g., Incoloy 800H) only in the regions that were exposed to molten fluoride salts, then a compromise could be achieved to get both air oxidation and molten salt corrosion resistance. This is a result of significant and direct value to future molten salt systems.
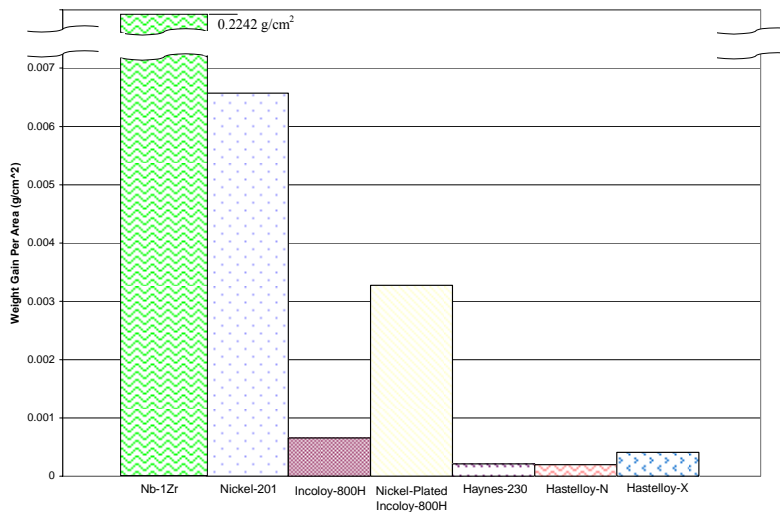
Figure 31. Results of air oxidation study performed for various materials in air at 850°C for 500 hours.

4. f. Analysis of Ni-Electroplated Incoloy 800H

Because of the practical promise of Ni-electroplating to mitigate corrosion, and the ability of Ni-electroplating to be applied in a non-line-of-sight manner on the inside surfaces of long tubes in a cost-effective manner, Ni-electroplated Incoloy 800H samples were investigated in greater detail. An intriguing observation after high temperature corrosion testing of Ni-electroplating was the observation of voids throughout the Ni-plating (Figure 32). Mechanisms for the formation of these voids include Kirkendall effect as seen in other superalloys without adequate oxidation resistance [18], initial porosity of the plating that coalesce to form voids. Additionally, the possibility that the voids were caused by impurities has also investigated. Hydrated salt and oxide impurities in the Ni plating can decompose at elevated temperatures to form steam that will expand Ni coatings under heat treatment [19]. To test these hypotheses, Ni-plated 800H samples were exposed to conditions similar to those experienced during corrosion testing, but in an inert helium environment.
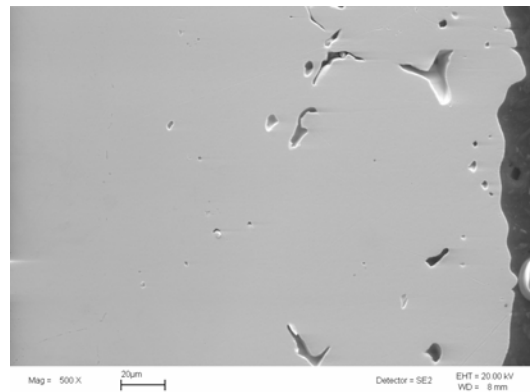
Fig. 32. Ni-plated Incoloy-800H after corrosion testing showing void formation in the plating.

Fig. 33 shows the cross-sectional image of heat treated (in helium atmosphere) Ni-plated 800H. The presence of the voids demonstrates that their formation was not exclusive to the Ni-plated 800H samples exposed to FLiNaK. The abundance of voids seen in the heat treated sample was not as high as that observed in the samples exposed to FLiNaK.
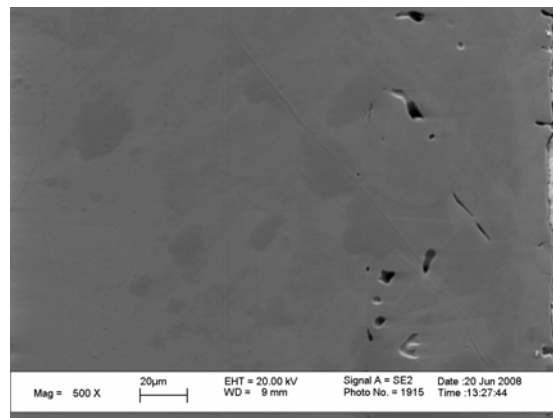
Figure 33. Ni-plated Incoloy-800H heat treated at 850°C for 500 hours in helium environment showing the formation of voids but in less abundance than those observed in molten salt exposed samples.

To further elucidate the origin of the voids, another batch of samples was electroplated with Ni from the same commercial firm (Southwest United Industries Inc.) that had plated the previous samples. A sample from the second Ni-plated batch was exposed to the same heat treatment (850°C for 500 hours in helium environment). SEM images of the heat treated samples (Figure 34) shows much smaller voids and that they appeared to be primarily located at the alloy/plating interface. Due to this evidence, it is likely that the large number of voids seen in Figures 32 and 33 were due to impurities or a low density of the plating in that batch. These findings indicate that control of the purity and characteristics of the plating bath are important to ensure a compact, adherent Ni-plating.
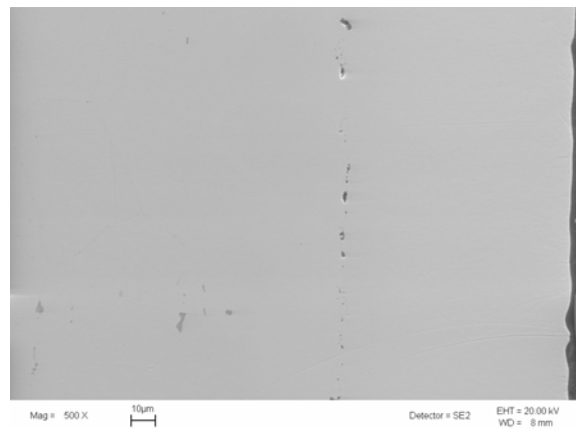
Fig. 34. Ni-electroplated Incoloy-800H heat treated at 850°C for 500 hours in helium environment showing the formation of voids along the alloy/plating interface.

It has been proposed by other researchers that as electroplated Ni-grains grow, impurities are swept up along the grain boundaries [20], which leads voids being found in these regions after heat treatment [21]. By this logic, the voids present in Fig. 32 should be found along grain boundaries. To evaluate the location of the voids, the samples were etched, and reexamined under SEM. The results are shown in Figure 35, and appear to support this claim.
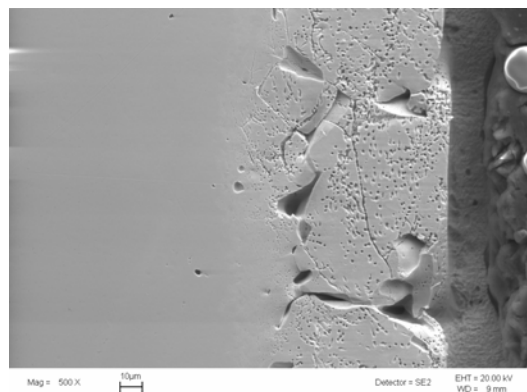
Figure 35. Etched Ni-plating, showing the preferential presence of voids in the vicinity of grain boundaries.

While it appears that the voids may be present at some grain boundaries, some boundaries appear to be devoid of these voids. Jacobson and Silwa [22] studied the location of voids and grain growth during heat treatments, and found that their location coincided with migrating, high angle grain boundaries. This work was inconclusive in regards to whether the voids were caused by gases or coalescence of excess vacancies. However, the voids seen in Fig. 34 appear to be from impurities at the alloy-plating interface.

The hardness of the Ni-plating was also investigated, and found to agree well with the results published by Jacobson and Silwa [22]. Initially, the electroplated Ni-plating is much harder than the Ni-201 that was also tested, however, after heat treatment/FLiNaK testing, the hardness of the Ni-plating and the Ni-201 samples appeared to converge (Figure 36).

Vickers Microhardness Tests

○ Ni-201
□ Ni-plating, heat 2
△ Ni-plating, heat 1

•The microhardness data follows the general trend
•Ridges on surface grains on FLiNaK exposed samples were polished off with diamond paste for hardness samples

	Pre HT	Post HT
Ni-201	151	104
Ni-Plate 1	253	80
Ni-Plate 2	251	75
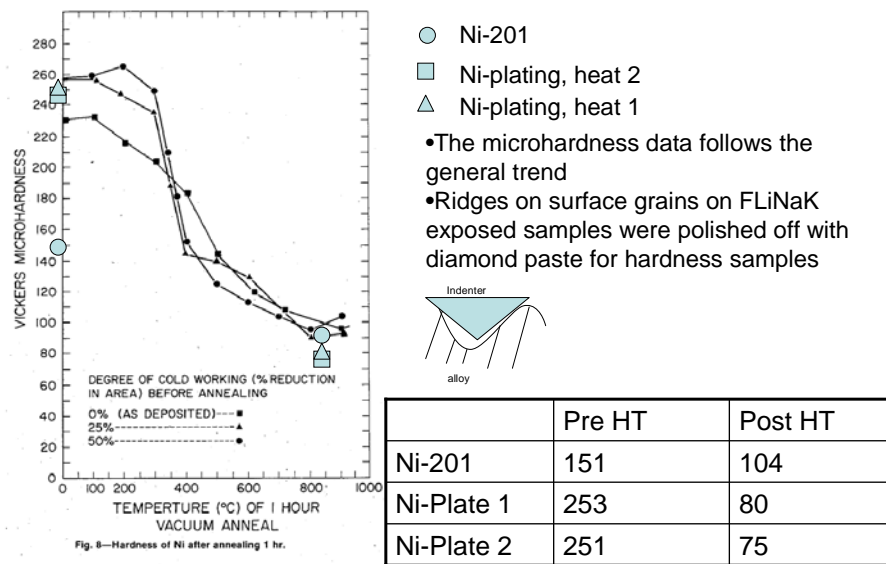
Source: B. Jacobson, J. Silwa, (1979). Structure and mechanical properties of electrodeposited nickel, Plating and Surface Finishing, pp. 42-47.

Fig. 36. Results from Vickers microhardness tests of Ni-electroplating after high temperature corrosion tests and heat treatments.

4. g. Graphite Interaction in High Temperature Corrosion Tests
An intriguing aspect of corrosion tests in FLiNaK was the high rate of corrosion observed in the alloys. It is speculated that the graphite crucible played a significant role in accelerating the corrosion process for all the alloys. The observation that most reinforced this belief was the observation of a Cr enriched layer on several of the graphite fixturing rods as shown in Figure 37.

Inconel-617, 22% Cr   Haynes-230, 23% Cr

Incoloy-800H, 20% Cr   Hastelloy-N, 6% Cr

Fig. 37. Photographs showing a sampling of gray deposits on the graphite fixturing rods after corrosion testing.

The graphite rods were examined using SEM/EDS technique. The results of these techniques (Fig. 38) demonstrated that the surface layer was enriched in Cr for all test capsules, and also Fe for the Incoloy-800H bearing capsule.
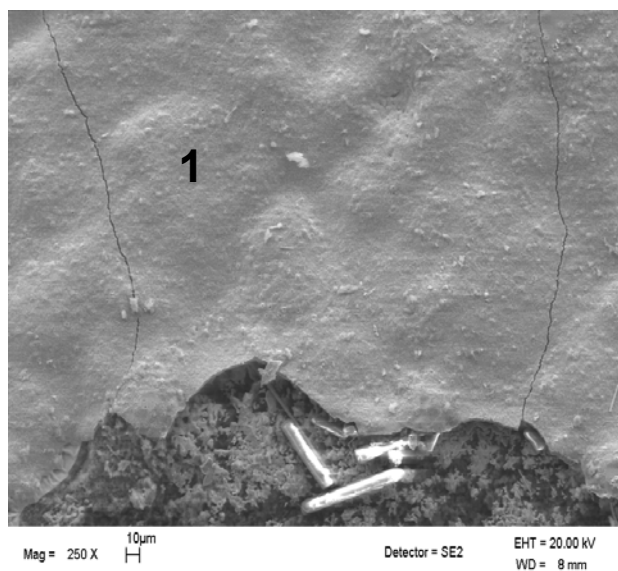
Fig. 38. SEM Micrograph of the surface of the carbon rod after corrosion testing on Alloy 800H in FLiNaK salt. EDS analysis performed at the point labeled '' showed the following composition: C: 57.9%, Cr: 32.2%, and Fe: 9.4%.

Figure 39 shows cross-sectional image of the surface layer formed on the graphite fixturing rod after corrosion testing of Incoloy 800H, Haynes 330 and Incoloy 617. The thickness of the Cr enriched layers did not appear to correlate to weight-loss data discussed earlier. Figure 39 also shows elemental x-ray maps for the deposited layer for Incoloy 800H sample test, and shows the layer to be enriched in Cr, Fe, and C.
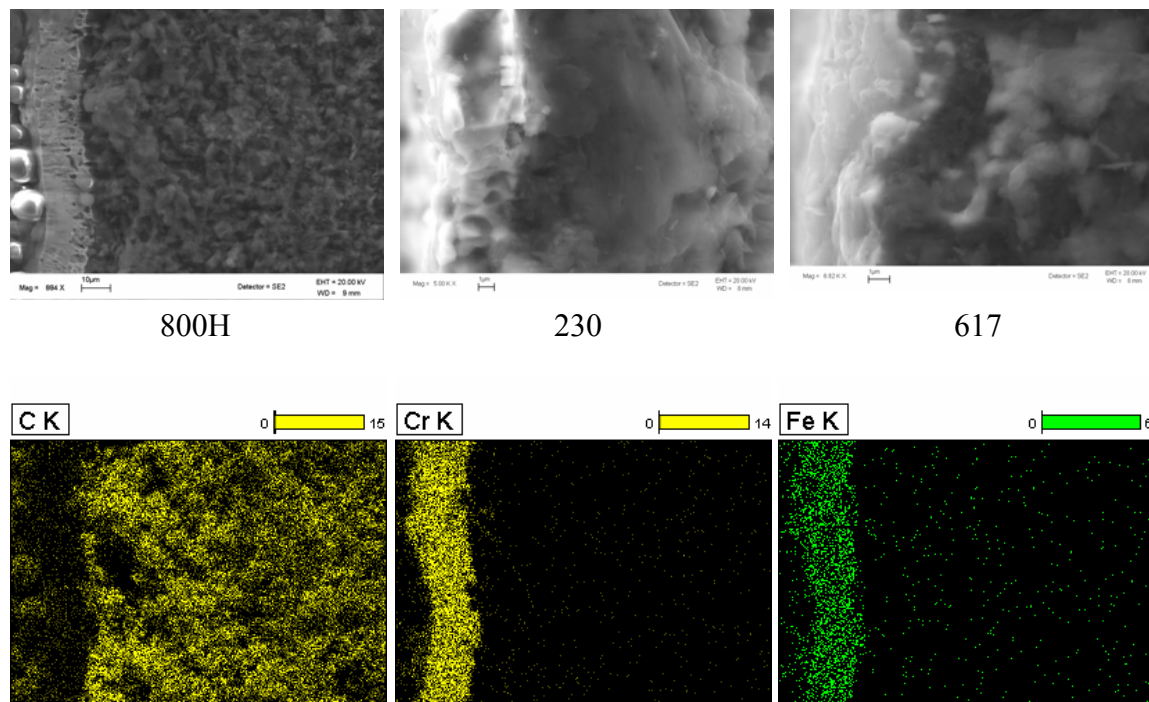
Fig. 39. SEM cross-sectional image of the layer deposited on graphite central rod after corrosion testing of Incoloy 800H, Haynes 230, and Incoloy 617. The lower pictures are EDS elemental x-ray maps of the layer formed in the Incoloy-800H test.

X-ray diffraction of the films on the graphite samples showed patterns corresponding to the Cr_7C_3 phase as shown in Figure 40. For the film on the graphite rod from the Incoloy-800H test capsule, there appeared to be a slight shift in the XRD pattern than that expected for pure Cr_7C_3. The pattern shift is believed to be from the incorporation of the smaller diameter Fe atom in the carbide phase, indicating that this surface layer corresponds to the $(Cr, Fe)_7C_3$ stoichiometry. The XRD pattern for the Haynes-230 and Inconel-617 graphite sample-fixturing rods were indicative of Cr_7C_3 stoichiometry, but had large background patterns due to the smaller thickness of the films in relation to the depth of the x-ray penetration during XRD analysis.
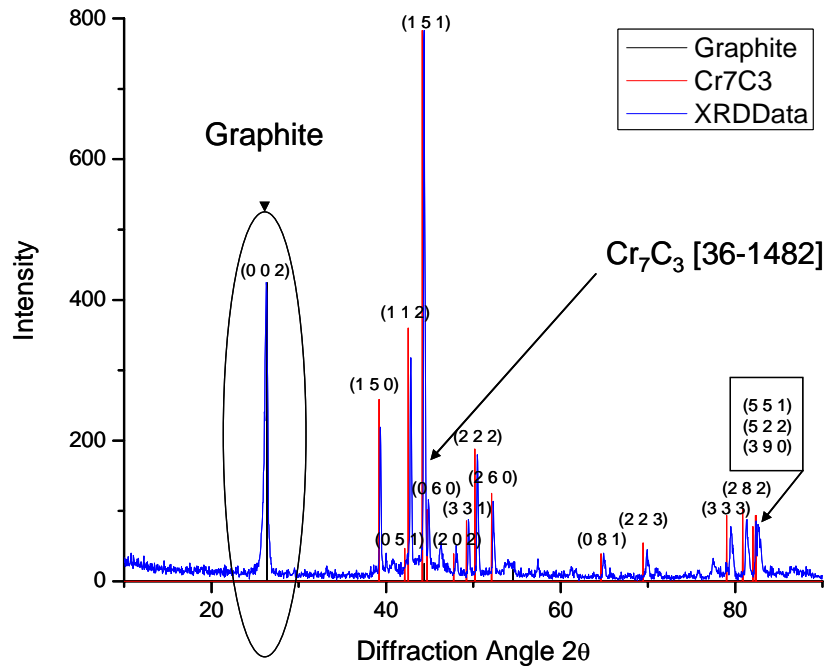
Fig. 40. XRD diffraction pattern of Cr enriched film on graphite fixturing rod from the Incoloy 800H corrosion test. The peak corresponds to Cr_7C_3 stoichiometry, but the slight shift in the peak position in conjunction with EDS analysis indicates the film to consist of $(Cr, Fe)_7C_3$ phase.

The findings of the x-ray diffraction studies were supported by XPS analysis (Figure 41). As reported by Tabet et al. [23] and Detroye et al. [24], the 1s peak at 282.7 eV is characteristic of a carbide phase, and the peak at 284.6 eV is characteristic of graphite. Furthermore, the Cr and Fe XPS peak position data closely matched the data presented by Detroye et al. [24] for $(FeCr)_7C_3$.
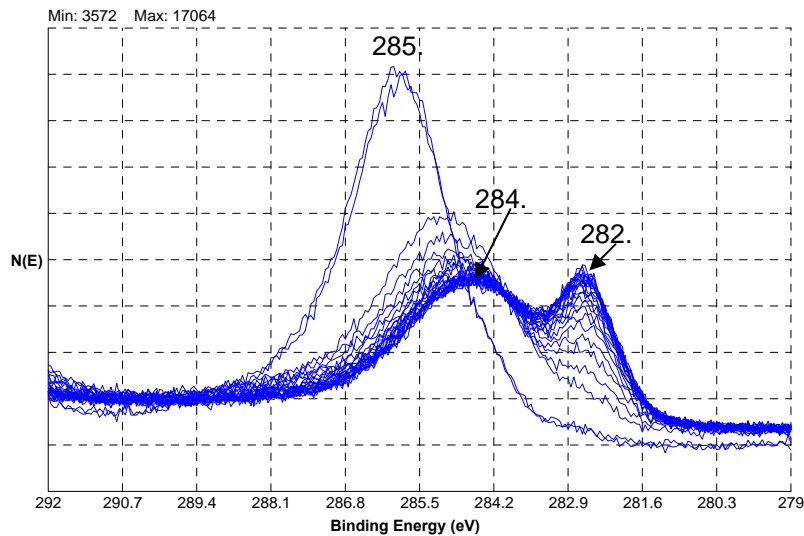
Fig. 41. Results of XPS analysis of surface layer deposited on the graphite central rod after testing Incoloy 800H, confirming the presence of a carbide phase on the surface.

It is believed that an acceleration of corrosion within the corrosion capsules was promoted by FLiNaK's tendency to sustain multiple valence states of Cr and the difference in chemical activity between the electronegative metal Cr in the alloy and that of the graphite crucible and components [8]. The aforementioned Cr-carbide film formation is speculated to be the result of the reaction, $21CrF_2+3C{\rightarrow}Cr_7C_3+14CrF_3$ at the graphite surface for the graphite capsule used to test Incoloy-800H, similar to the reactions seen in molten salt heat treatment baths discussed by Ozeryanaya [25]. Following the further oxidation of Cr^{2+} to Cr^{3+} and formation of the Cr carbide at the graphite interface, the Cr^{3+} ion migrates back to the alloy surface through convection or diffusion where it oxidizes Cr metal in the alloy and reduces back to Cr^{2+} from Cr^{3+} according to the reaction, $2CrF_3+Cr{\rightarrow}3CrF_2$ [25]. A detailed analysis of Cr-C interactions will be published as a journal article.

It is clear that if Cr was being removed from the FLiNaK during testing by the formation of a carbide with the graphite, the chemical activity of the molten FLiNaK would be increased. It follows that the increased corrosion potential of the molten FLiNaK would accelerate the corrosion of alloys. This accelerated corrosion has been further supported in our recent experiments where corrosion testing of Incolloy-800H samples in an Incoloy-800H crucible, under identical conditions, showed significantly less corrosion than the Incoloy-800H tested in the graphite crucibles. The results of this test demonstrated a very small weight-loss per area of 0.15 mg/cm^2, substantially less than that observed for this alloy in graphite crucible. Analysis of these Incoloy-800H samples, however, demonstrated that the corrosion mechanisms were indeed the same as those found in the alloys tested in the graphite capsules, i.e. migration and outward diffusion of Cr along the grain boundaries as shown in Figure 42.
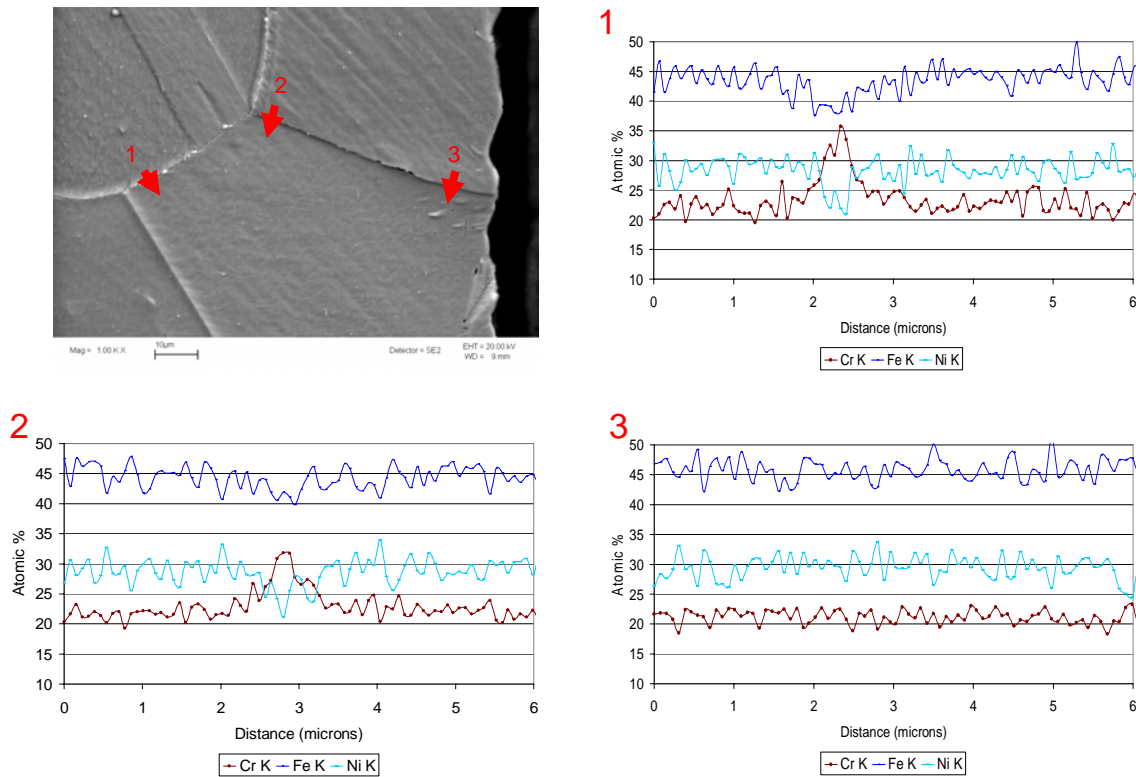
Fig. 42. **SEM micrograph of etched Incoloy-800H from the 800H crucible after exposure to molten FLiNaK for 500 hours at 850°C. It can be seen from the corresponding EDS line scans that Cr concentrations in the grain boundary region decreases near the surface of the alloy.**

The alloys under study demonstrated rather dramatic grain boundary corrosion after exposure to FLiNaK in the graphite capsules. Streicher [26] has shown that grain boundary corrosion can arise in specific grades of Hastelloy due to sensitization after exposure to temperatures in the range 650-1200°C. This can lead to the formation of M_6C, $M_{23}C_6$ or M_7C_3 type carbides at the grain boundaries. These carbide phases can lead to corrosion either by forming a galvanic couple with the neighboring matrix (and lead to preferential dissolution of the matrix) or by self-dissolution. It is believed that both effects may be occurring in the high temperature FLiNaK corrosion tests. The Mo/W enriched particles in Hastealloy X and Haynes 230 lead to a galvanic couple and dissolution of the alloy matrix directly surrounding the carbides when the carbides are located at grain boundaries, as seen in Fig. 43 for W-containing Haynes 230. Another effect of carbide formation is that carbides can concentrate Cr at the grain boundaries, which may directly be dissolved into the FLiNaK.
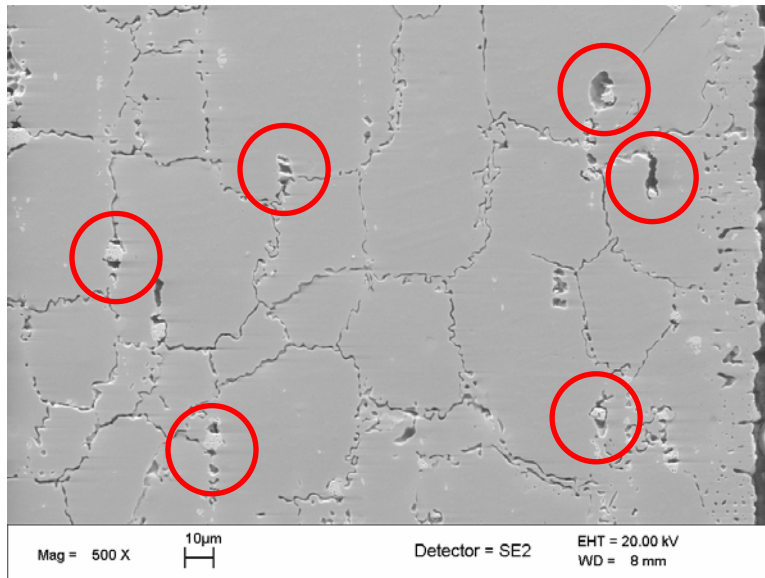
Fig. 43. Circled regions are W-rich precipitates in Haynes 230 (after corrosion tests) that appear to have led to dissolution of the neighboring alloy matrix.

Streicher [26] has shown that control of carbon content in alloy can dramatically lower carbide formation and mitigate this intergranular corrosion mechanism. Jackson et al. [27] have described corrosion in molten heat treatment salts to be primarily along carbide networks, rather than by direct dissolution from the alloy matrix. The carbon contents from the specific heats of the alloys from used this research program tests in FLiNaK are listed in Table 6. Figure 44 shows that an excellent correlation exists between the carbon content of the alloy and the weight loss experienced during corrosion testing in FLiNaK.

Table 6. Carbon contents of specific alloys that were tested for corrosion.

Alloy	Carbon Content (weight %)
Hastelloy-N	0.03
Hastelloy-X	0.059
Inconel-617	0.08
Haynes-230	0.1
Incoloy-800H	0.069
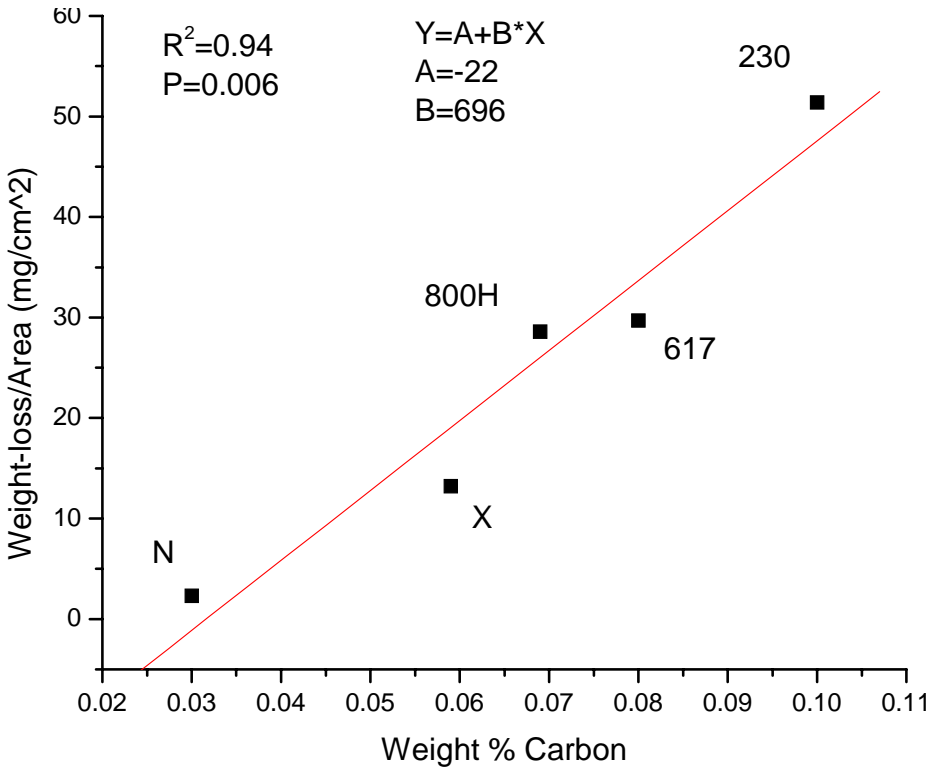
Fig. 44. Weight-loss per area as a function of weight percent carbon in the alloy heats tested.

The R^2 of 0.94 in Figure 44 implies a good correlation between weight-loss per area and carbon content. This correlation is much better than any correlation for weight-loss vs. alloying element investigated so far and than that obtained for Cr itself. It appears that carbon content of the alloys explains the difference in corrosion of the high Cr alloys (~21% Cr) Hastelloy-X, Incolloy-800H, Inconel-617, and Haynes-230. It is interesting that the lower Cr content alloy, Hastelloy-N (~6% Cr) exhibits such a good correlation. This implies that by the time an alloy attains 6% Cr, Cr-carbide formation may already be a dominant corrosion mechanism. At the same time, the low carbon content of Hastelloy-N may be just as important as its low Cr content in mitigating corrosion.

The role of carbon in intergranular corrosion of alloys in molten fluoride salts is important, but may be of limited value. In the alloys studied, carbide formation cannot be avoided at the temperatures of interest if kept at the present concentrations. Carbide phases also play the role of strengthening these alloys.. Heat treatments exist, such as spherodization, where the carbides are formed more uniformly in the alloy matrix and not allowed to form primarily at the grain boundaries, which could potentially decrease the grain boundary attack. However, spherodization is often performed to make an alloy more malleable, and results in decreased strength.

5. HIGH TEMPERATURE ELECTROCHEMISRTY OF MOLTEN SALTS

5.a. Introduction

High temperature electrochemistry was performed to gain a fundamental understanding of corrosion in molten salts, and with the long-term goal of developing *in situ* probes to monitor corrosion on-line in molten salt systems. To achieve this objective anodic stripping voltammetry (ASV) was performed in conjunction with independent chemical analysis of salts by neutron activation analysis (NAA) in the University of Wisconsin nuclear reactor (UWNR). Specific emphasis was placed on the detection of Cr, which is an important constituent in high temperature alloys, and also most prone to dissolution in molten FLiNaK salt.   Salts from the corrosion tests described earlier were evaluated using ASV and NAA techniques. The procedures were validated by addition of known quantities of Cr in form of Cr-fluorides to pure FLiNaK salt. Tests were performed in molten FLiNaK at a temperature of 650°C. Finally, the technique has been extended to the detection of Fe which also exhibits a propensity for dissolution in molten FLiNaK salt.

6. b. Basic Principles of Anodic Stripping Voltammetry

Anodic stripping voltammetry (ASV) is an electrochemical technique that allows for determination of concentrations of trace metal cations in solution. Each ionic species has its own reduction potential, or half-cell potential, which can be calculated by the Nernst equation,

$$E = E^0 - \frac{2.3RT}{nF} \log \frac{Activity_{Reactant}}{Activity_{Product}}$$

where,

E = half cell potential

E_0 = standard half cell potential at 25 °C

R = universal gas constant

T = temperature of the cell

n = number of electrons transferred in the reduction

F = Faraday constant

Table 7 gives the emf series of several elements of interest in FLiNaK as measured by other researchers [28 - 30]. Temperature and type of reference electrodes (RE) are also given. QRE denotes quasi reference electrode.

ASV is a three step process that involves the use of three electrodes: the working electrode (WE), the counter electrode (CE), and the reference electrode (RE). ASV is performed in a potentiodynamic corrosion cell in which a potential is applied and the resulting current flow is measured. When ASV is performed in a potentiodynamic cell, a voltage is applied to the cell to polarize the WE and CE causing a current to flow from the WE to the CE. Since the electrolyte in the cell has a fixed resistance, there will be a voltage drop across the cell (potential drop (V) = current (i) * solution resistance (R)). Therefore, by using a third electrode (the reference electrode (RE)), with no current flowing between it and the WE, a known potential can be measured between the WE and the RE. Figure 45 shows the basic electrochemical cell for ASV. A very large resistance exists between the WE and RE so minimal current is generated. This keeps the RE unpolarized and at a constant potential throughout all voltammetric measurements. The WE

and CE are located in an electrolyte bath with the RE, but current should only flow between the WE and CE. All three electrodes connect to a potentiostat which controls the potential between the WE and RE and measures and records the current flowing between the WE and CE and the potential between the WE and RE.

Table 7. Measured reduction potentials in molten FLiNaK.

Reaction	Reduction Potential (V)	RE	Temperature (C)	Sources
Zr(IV)/Zr	-1.4	Pt-QRE	500	19
Fe(II)-Fe	-0.60	Pt-QRE	500	27
Fe(III)-Fe(II)	-0.5	Pt-QRE	500	24
Ni(II)-Ni	-0.2	Pt-QRE	500	26
Fe(II)-Fe	-0.39	Ni(II)/Ni	500	13
Fe(III)-Fe	-0.2	Ni(II)/Ni	500	13
Ni(II)-Ni	0.0	Ni(II)/Ni	500	13
Al(III)-Al	-1.5	Ni(II)/Ni	750	15
Cr(II)-Cr	-1.13	Ni(II)/Ni	750	15
Cr(III)-Cr(II)	-0.69	Ni(II)/Ni	750	15
Fe(II)-Fe	-0.512	Ni(II)/Ni	750	15
Fe(III)-Fe(II)	-0.21	Ni(II)/Ni	750	15
Ni(II)-Ni	0	Ni(II)/Ni	750	15
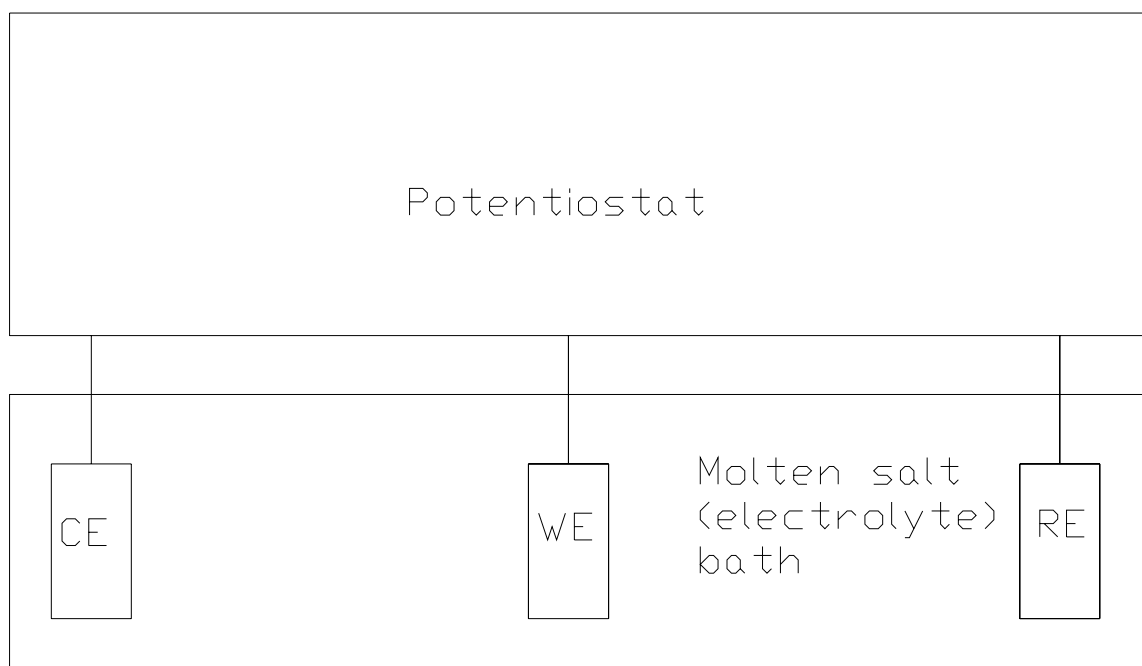
Figure 45. Basic design of the electrochemical cell used for anodic stripping voltammetry.

The three steps of the ASV technique are the plating step, the stripping step, and the cleaning step. Throughout the process of anodic stripping, all reactions of interest occur at the WE, while the CE is used only as a path to allow current to flow in the solution. The CE is kept at opposite polarity with respect to the WE (as measured against the RE) and has a much larger surface area. The larger area ensures that the CE does not limit the reaction at the WE due to insufficient area to conduct current. RE is needed to give a reference for comparing the potential of the WE so that repeatable results may be more easily obtained.

Figure 46 shows the circuit during the plating process when a voltage is applied between the WE and CE, making the potential of the WE negative compared to the CE. The actual voltage of interest in the cell is measured between the WE and the RE. The potential of the WE, with respect to the RE, must be more negative than the reduction potential of the ionically charged chemical species of interest (hereafter referred to as the analyte) to plate the analyte on the WE. As ions reduce to metal atoms onto the WE, electrons flow from the positive CE to the negative WE. All reactions of interest occur at the WE. When a metal atom reduces onto the WE, an oxidation process must occur at the CE. However, due to the complexity of the system, the oxidation process could represent a number of different reactions. Knowing the reaction at the CE is not necessary to complete the ASV process as long as the reaction at the CE does not limit the reaction occurring at the WE.

Following the plating step, the stripping step oxidizes the accumulated analyte, leading to a reversal of electron flow. This is accomplished by linearly increasing applied voltage between the WE and the CE from the plating potential until the WE is more positive than the reduction potential of the analyte. As the reduction potential of each analyte is passed, the metal atom oxidizes off the electrode surface (deplates) and electrons flow can be measured.

The voltage change and subsequent current measurement is referred to as the stripping step. Figure 47 shows that during the stripping step, the WE is brought to a more positive potential, and current flows as metal atoms oxidizes into the solution.
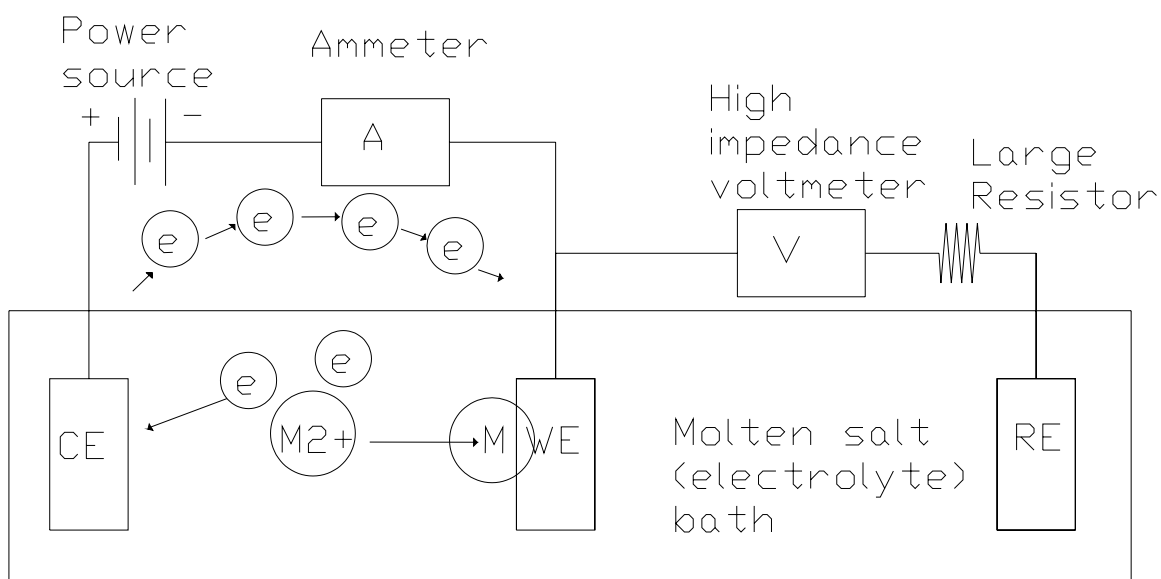
Figure 46. Details experimental system for plating.
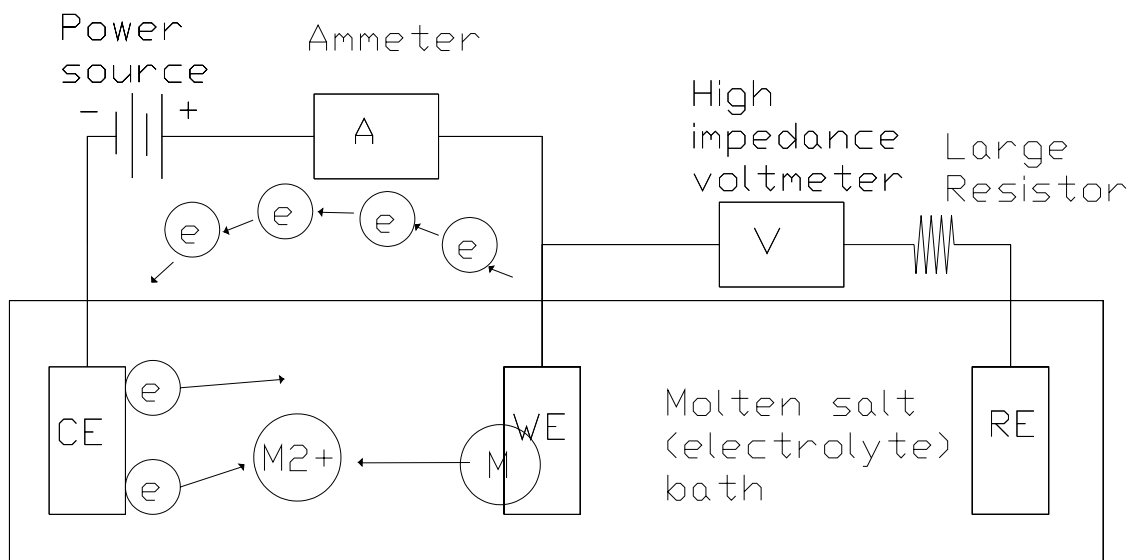
Figure 47. Current flow during stripping step.

Following the stripping step, a cleaning step is performed to ensure that all metal ion species that are plated initially have been oxidized back into the solution. This is accomplished by holding the potential of the WE greater than the reduction potential of any analyte in solution until the current through the cell reaches a steady value. The cleaning step is generally used with mercury electrodes to force metal ions

out of the mercury solution, but the cleaning step has also been performed on metal electrodes [31]. Although the cleaning step is not necessary for ASV, it increases repeatability of results by ensuring that the surface of the WE has had the same treatment before each test.

The three steps of the anodic stripping process described in circuit diagrams above are shown graphically in Figure 48. The initial voltage must be more negative than the reduction potential of any analyte of interest, and the voltage during the stripping step must then pass through the reduction potential of the analyte in order to detect it.

Potential vs. Time in Anodic Stripping
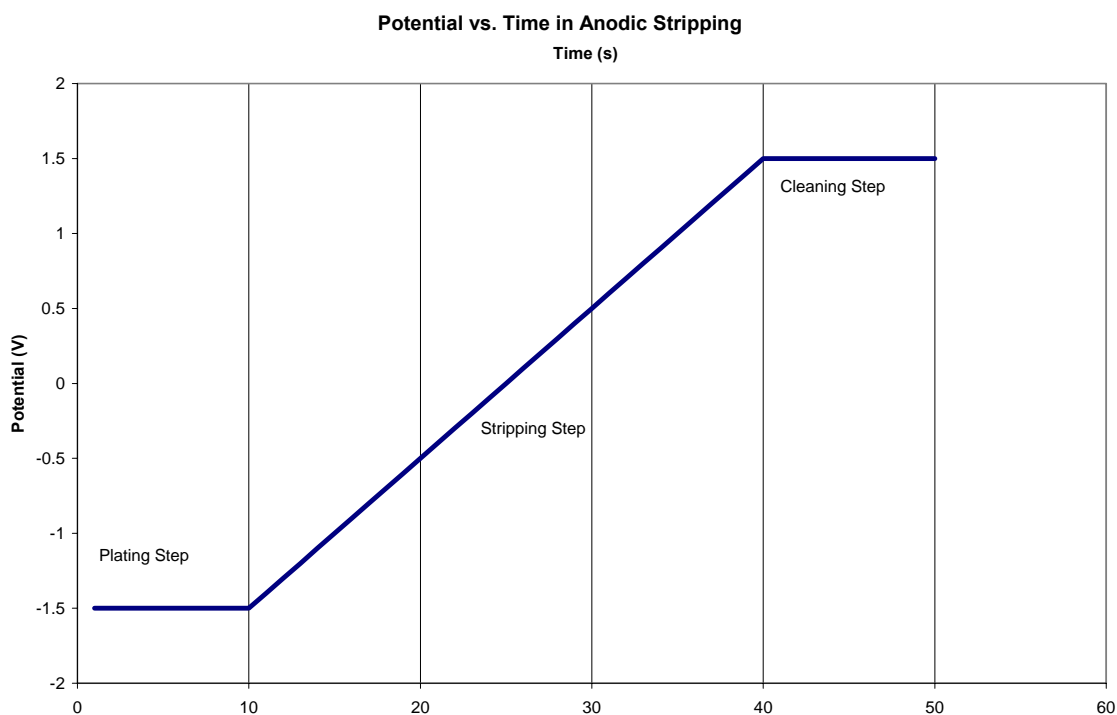
Figure 48. The three steps of the anodic stripping process.

The duration of the plating step depends on the concentration of the analyte in the solution. An acceptable duration will provide an adequate signal-to-noise ratio during the stripping step. Once a sufficient amount of analyte has been plated on the negatively charged WE, the voltage across the electrodes is made more positive so that the potential on the WE passes the reduction potential of the analyte. When the potential of the WE passes through the reduction potential of the analyte, the analyte oxidizes off of the WE into solution. When the analyte oxidizes, it becomes a cation, according to its valence state. The introduction of electrons from the oxidation of the analyte causes the current between the WE and CE to increase. Once the potential of the WE passes the reduction potential of the analyte, the electron current then decreases back to the baseline due to depletion of the analyte from the WE. The size of the current peak is proportional to the concentration of the analyte that was plated onto the WE, and thus to the concentration of the analyte in the solution. This principle is used for the detection of metal cation species in solution to detect Cr and Fe.

5.c. Experimental Procedure for Anodic Stripping Voltammetry

Pt wires are used for the working electrode (WE), counter electrode (CE), and quasi-reference electrode (QRE), because of its high nobility and if maintained in an unoxidized state, it allows for the detection of any metal cation that is less noble. Glassy carbon was used as the container for the molten salt because of its relative inertness to molten FLiNaK salt.

Keeping the surface area constant between voltammetric measurements increases repeatability. Attempts have been made to hot press boron nitride (an insulator in molten fluorides) along the entire WE length, exposing only the bottom tip to the molten salt. Because hot pressed boron nitride is not electrically insulating above 500 °C in FLiNaK, a mechanical method of obtaining a constant surface area must be used (i.e. the electrode is only dipped a set distance into the melt for each measurement.) This method is not ideal because it can be difficult to determine the surface area precisely. Alumina (Al_2O_3) can be used to insulate the entire WE, except for the bottom surface that will be polished to a mirror finish, giving an exact surface area of the WE.

All molten salt work was performed under an Ar atmosphere in a glovebox. Materials used in the electrochemical cell are listed in Table 8. Figure 49 shows the initial electrochemical experiment setup with a Pt-QRE.

Table 8. Materials used for electrochemical measurements.

Material	Use in experiment	Description (if applicable)	Vendor
CrF_2	Working curve development	Anhydrous, 99% purity	Alfa Aesar
CrF_3	Working curve development	Anhydrous, 99% purity	Alfa Aesar
Cr metal	Working curve development	2-3 mm pieces, 99.995% purity	Alfa Aesar
FeF_2	Working curve development	Anhydrous, 99.9% purity	Alfa Aesar
FeF_3	Working curve development	Anhydrous, 98% purity	Alfa Aesar
Fe wire	Working curve development	1 mm, 99.99% purity	Alfa Aesar
NiF_2	Reference Electrode	Anhydrous, 99% purity	Alfa Aesar
Ni wire	Reference Electrode	2 mm 99.98% purity	Alfa Aesar
Graphite	Reference Electrode	Open porosity:15%, medium pore size:2 μm	SGL Carbon
Graphite	Secondary Container	GR060	Graphite Store
Graphite	NAA sampler	AXZ-5Q	POCO graphite
Alumina bisque	Electrochemical setup support	Machinable	McMaster
Alumina Paste	Secure alumina	Resbond 989	Cotronics Corporation
Glassy Carbon	Salt container	Sigradur GAT 19	Hochtemperatur-Werkstoffe GmbH (HTW)
FLiNaK Salt	Salt under analysis	(46.5 mol% LiF-11.5 mol% NaF-42 mol% KF)	Electrochemical Systems, Inc.
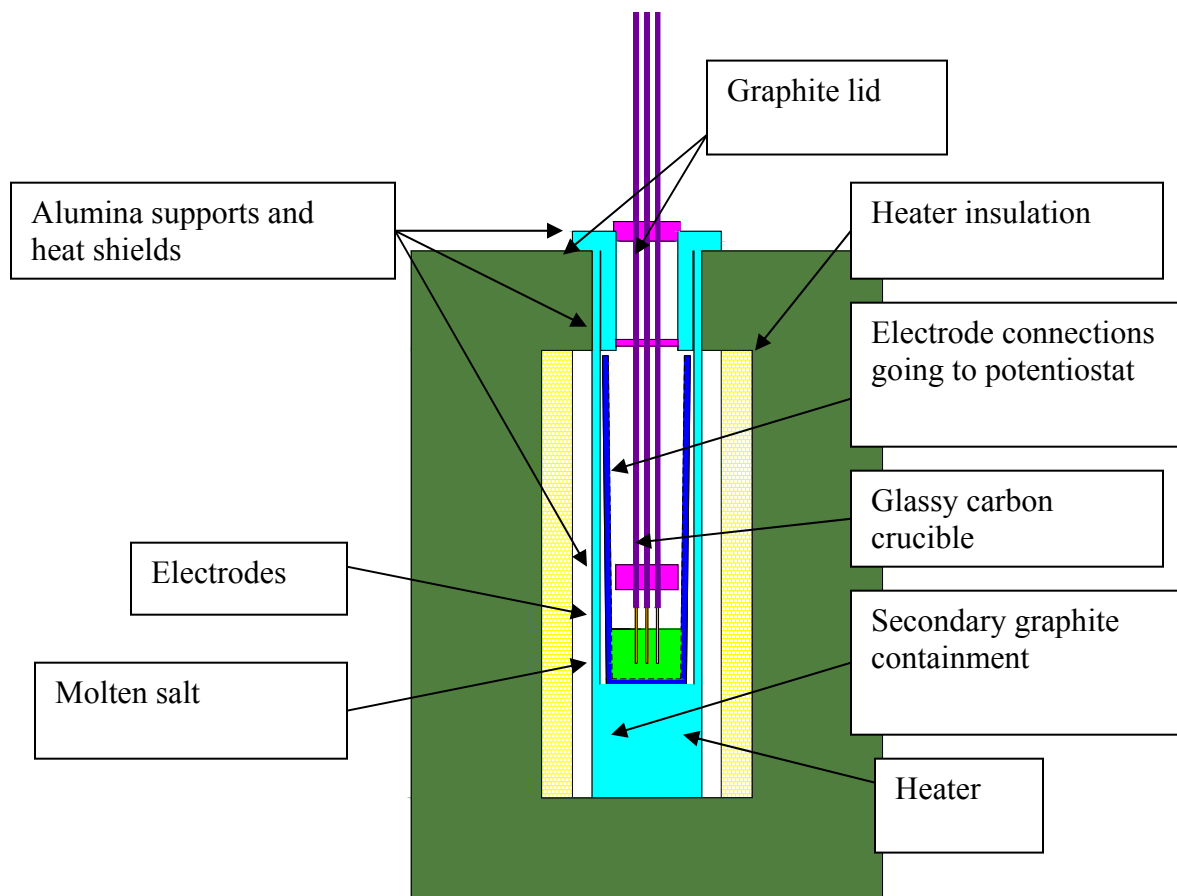
Figure 49. Schematic illustration of the experimental system for high temperature electrochemistry studies in molten FLiNaK.

In the center (please see Figure 49) are the three electrodes used for voltammetry. The bottoms of the electrodes are immersed in molten salt. An alumina apparatus hold the electrodes in place. Figure 50 shows a picture and a schematic of the alumina apparatus used for holding the electrodes.
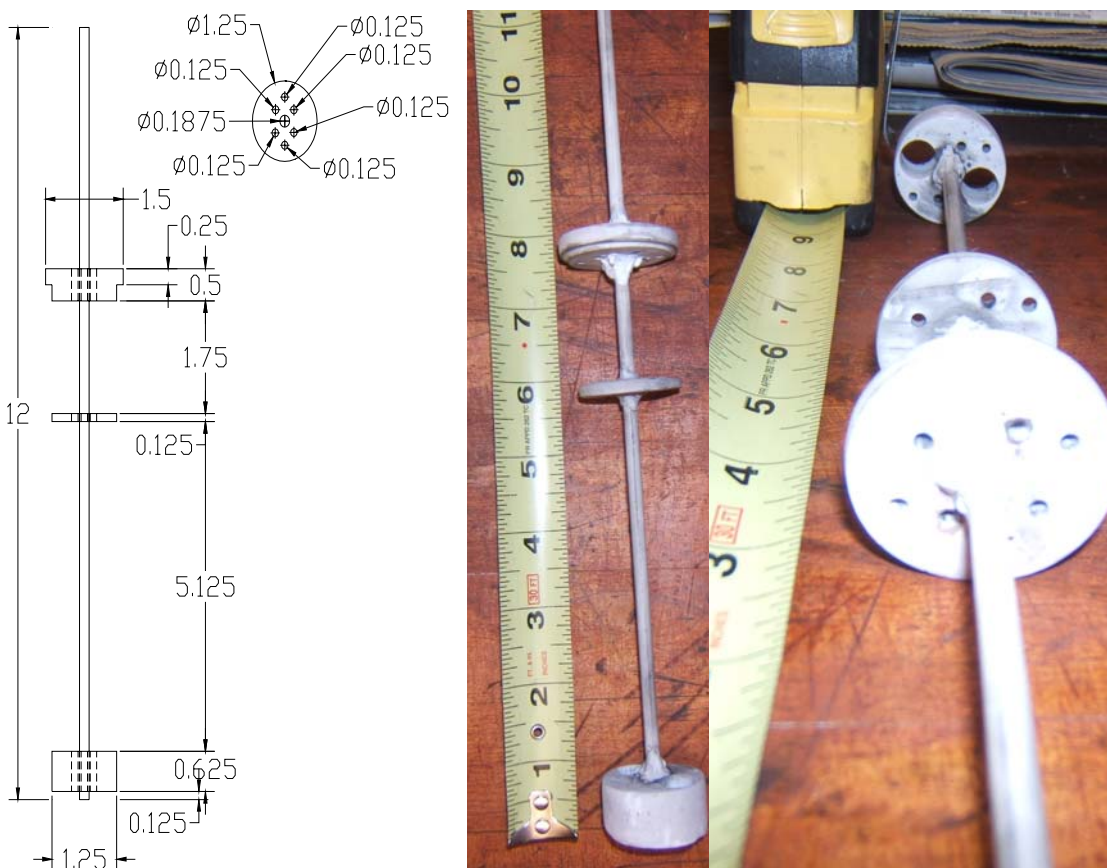
Figure 50. Alumina apparatus for holding electrodes during electrochemical measurements. The larger holes through the bottom piece were drilled when the RE were implemented.

Fired and unfired alumina bisques were tested. Fired alumina bisque was more durable while unfired alumina bisque became embrittled with time. However, the unfired alumina bisque could be machined easily to accommodate updates to experimental hardware such as the addition of a Ni(II)/Ni RE, to be discussed in a later section.

The molten salt is contained within a 1.4" diameter glassy carbon crucible that rests within a larger graphite crucible. The graphite crucible acts as a secondary containment in case the glassy carbon crucible breaks. A graphite lid and alumina shields help to equalize temperatures. A Thermocraft RH ceramic heater was used in conjunction with LabView for temperature control. A Solartron 1287 potentiostat was used for voltage control and current measurement.

The WE and CE were both 1mm Pt wires. The CE was 0.5" longer than the WE to ensure that it had a larger surface area. A Pt-QRE was used. Figure 51 shows a picture of the electrode setup. Ni wires were welded to the Pt electrodes to reduce the amount of platinum used in the electrochemical setup (to reduce the price of the setup).
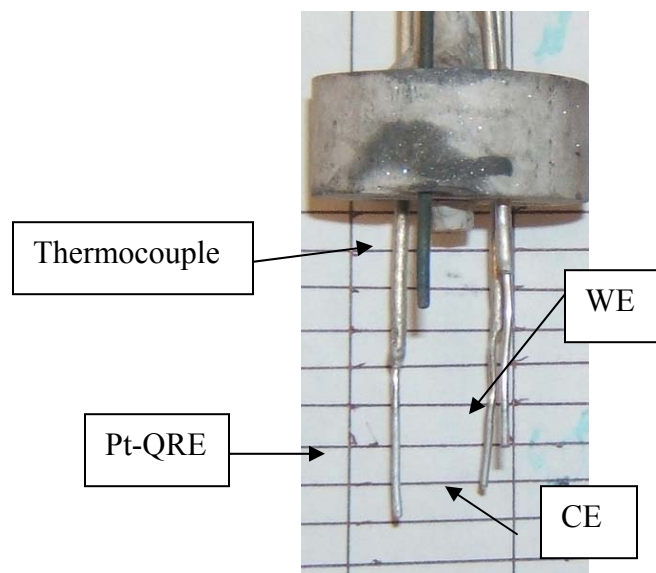
Figure 51. Electrochemical setup with Pt wires for the WE, CE, and QRE.

5.d. Optimization of Electrochemical Parameters

To ensure that no pure salt was wasted while electrochemical parameters were optimized, initial molten salt voltammetric measurements were performed using previously exposed salt from the 500 h static corrosion tests. The salt from the test of Ni-201 showed no weight loss, so it was taken as a "pure" salt baseline. To obtain a working curve of peak current as a function of Cr concentration, small portions of salt exposed in the static corrosion test of Haynes-230 (a 22.5 Cr% alloy) were added. This salt was chosen because Haynes-230 exhibited the largest weight loss and hence released a substantial amount of Cr into the molten salt.

Attempts were initially made to insulate the WE with alumina to provide a constant surface area throughout the breadth of the experiment. The Pt WE was inserted into a small hole drilled in alumina bisque that was subsequently fired at 1700°C. The firing shrunk the alumina around the Pt and reduced the alumina bisque porosity from 20% to near 0. Only the polished bottom of the Pt rod was exposed to the salt. However, alumina proved to be unstable in FLiNaK, and the dissolution of alumina introduced a large concentration of unwanted aluminum ions into the melt. The current peak during the stripping step was large enough that it masked any current peaks of other ions of interest. Insulating the WE was summarily abandoned, and the surface area of the WE was calculated by the depth that the WE was immersed in the molten salt. This depth was controlled by bending the Ni wire which connected the Pt electrodes to the potentiostat at a set distance for all measurements.

Several parameters were optimized using salts from the static corrosion tests. Acceptable plating times ranged from 15 s to 60 s. 15 s was chosen as optimal to reduce the total time of the electrochemical test as the heater was turned off during testing. A scan rate of 0.1 V/s was used for the stripping step. Scan ranges varied depending on the element of interest during the scan. The cleaning potential was held until the current was less than 0.001 A. A cleaning time of 10 s proved adequate for all measurements. Peaks were detected at -1.1, -0.79, -0.14, and 0.3 V for tests performed against a Pt-QRE.

5.e. Working Curves for Cr in FLiNaK using Pt-QRE

In an attempt to determine the Cr peak from the data obtained using salt from the static corrosion tests, an experiment was performed in which approximately equal amounts of CrF_2 and CrF_3 were added to pure FLiNaK. Anodic stripping was performed after each Cr addition with the following parameters: a plating potential of -0.7 V, a scan rate of 0.1 V/s, a final potential of 0V, and a cleaning potential of 0V. 1 mm Pt wires were used as the WE, CE, and QRE. The CE and QRE were inserted 1.5 cm into the melt while the WE was inserted 0.5 cm into the melt.

Concentration of Cr in the solution was estimated by calculation and confirmed by NAA. Samples for NAA were taken using a 3/8" graphite rod with a 1/4" hole drilled into it at an angle. Figure 52 shows a drawing of the sample removal tool as well as a picture of this tool with and without a small sample of salt in the collection area.
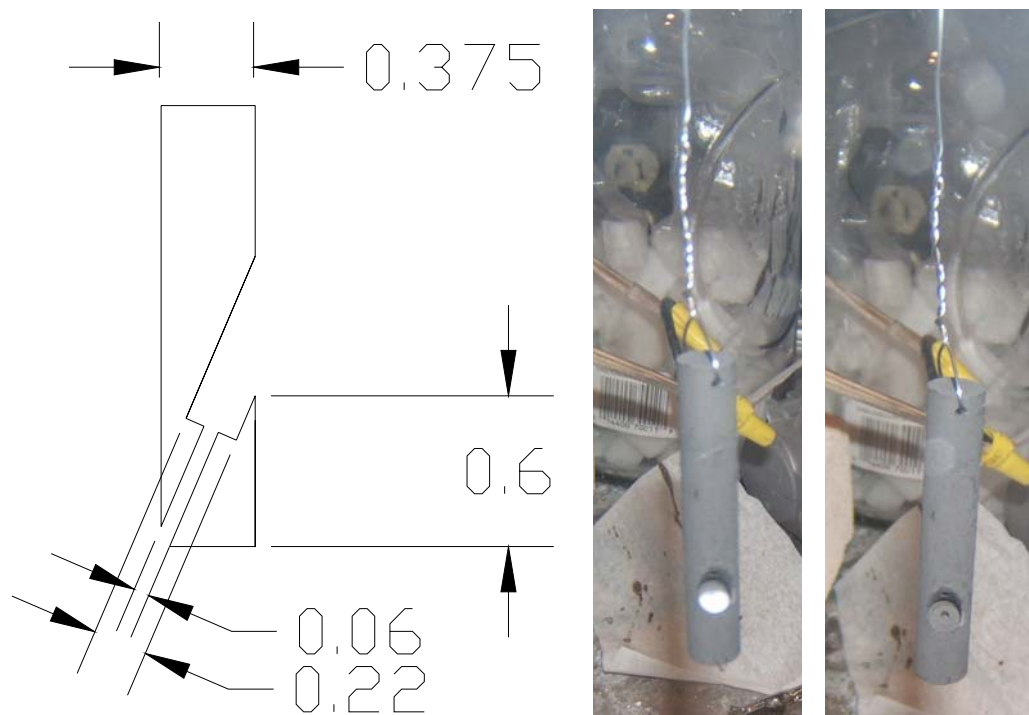
Figure 52. NAA sample removal tool drawing (left) and pictures with (center) and without (right) a salt sample. Dimensions are in inches.

Two working curves of integrated current as a function of Cr concentration were obtained: one for Cr concentrations ranging from 10-300 PPM, the second for Cr concentrations of 100-900 PPM. To obtain the low concentrations of Cr for the 10-300 working curve, salt from the high Cr concentration (900 PPM) tests was added to pure FLiNaK. Equal portions of salt were removed as added using the NAA sampler to keep the exposed area of the WE constant for all measurements. A 30s plating time was necessary for the lower concentration curve while a 15s plating time was sufficient for the higher concentrations.

The electrodes built up a dark surface layer over time, necessitating regular cleaning to obtain reproducible data. The layer can be seen in Figure 53. The surfaces near the red lines were above the salt line while the surfaces near the black lines were immersed in the salt.
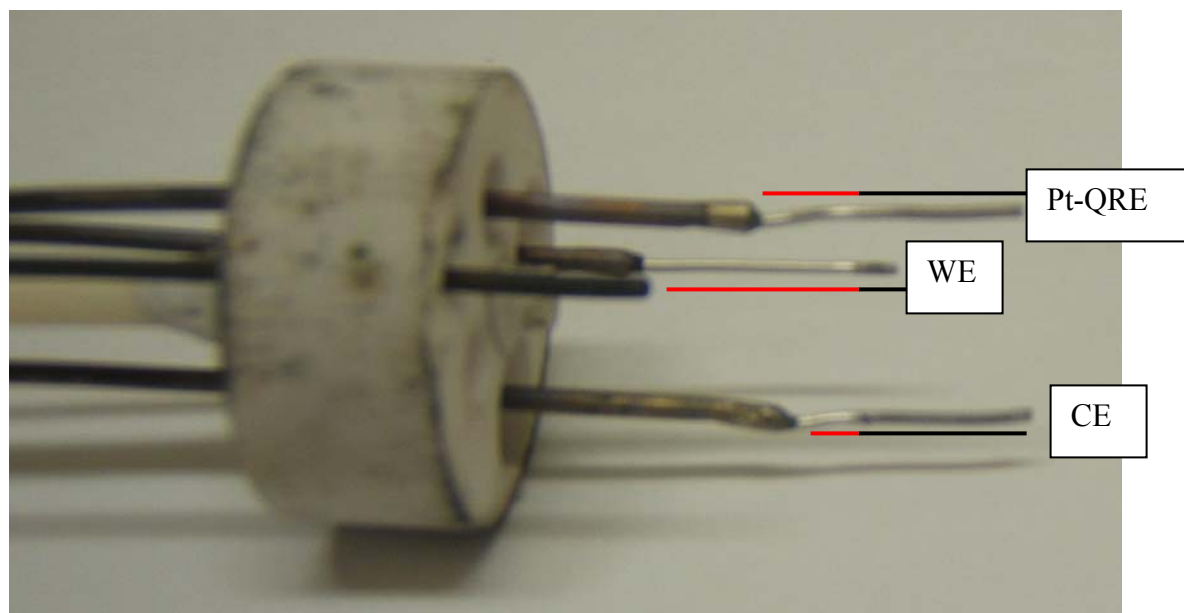
Figure 53. Film buildup on electrodes and the red lines indicate the portion of the electrodes above the salt.

The layer is likely carbon introduced into the salt from the support structure or the glassy carbon. Inspection of the salt after multiple days of taking electrochemical data showed what appeared to be a thin layer of graphite on the surface. The electrodes were cleaned each morning by polishing with 1 micron diamond paste and ultrasonically cleaning for 5 minutes in methanol and distilled water, the suggested method of removing any excess diamond paste.

5.f. Working Curves for Cr in FLiNaK using Ni(II)/Ni Reference Electrode

Following the development of the working curve using the Pt-QRE, another working curve was obtained using a Ni(II)/Ni RE. While the Pt-QRE was very durable, the Ni(II)/Ni RE was expected to give a more constant potential for comparison. Two 10 mol% Ni(II)/Ni RE were prepared for this purpose. The RE were contained in graphite with an average grain size of 0.008 in, a bulk density of 1.73 g/cm^3, an open porosity of 15 vol%, and a medium pore size of 0.00008 in. Table 9 shows masses used for each reference electrode. Figure 54 shows a schematic of the Ni(II)/Ni RE.

Table 9. Masses of FLiNaK and NiF_2 used in 10 mol% Ni(II)/Ni RE.

RE 1		
Mass NiF_2 (g)	Mass FLiNaK (g)	Mol%
0.1365	0.5265	9.968
RE 2		
Mass NiF_2 (g)	Mass FLiNaK (g)	Mol%
0.1345	0.5165	10.007
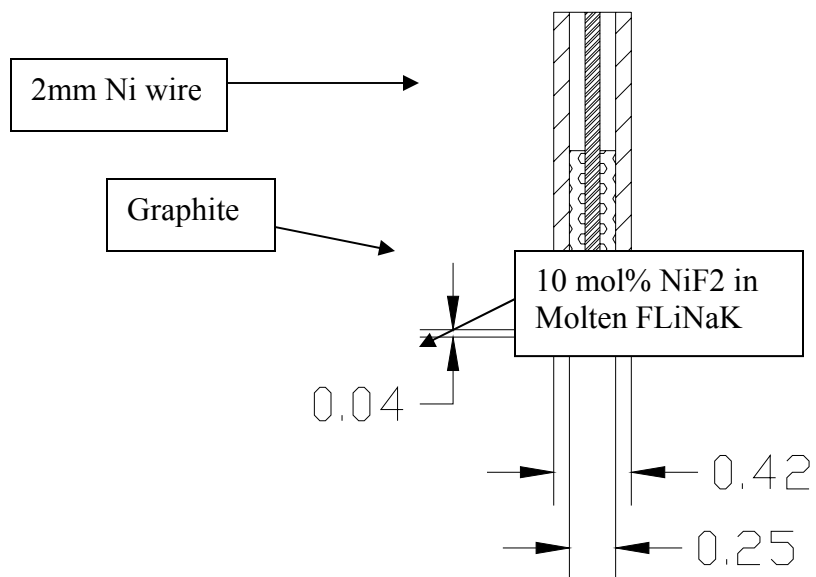
Figure 54. Schematic of Ni(II)/Ni RE. Dimensions are in inches.

Two RE are necessary to ensure that wetting has occurred and that the RE are stable over time. Checking the open circuit potential between the two reference electrodes gives insight into the condition of the reference electrodes with respect to one another. Figure 55 shows a schematic of how both RE are used.
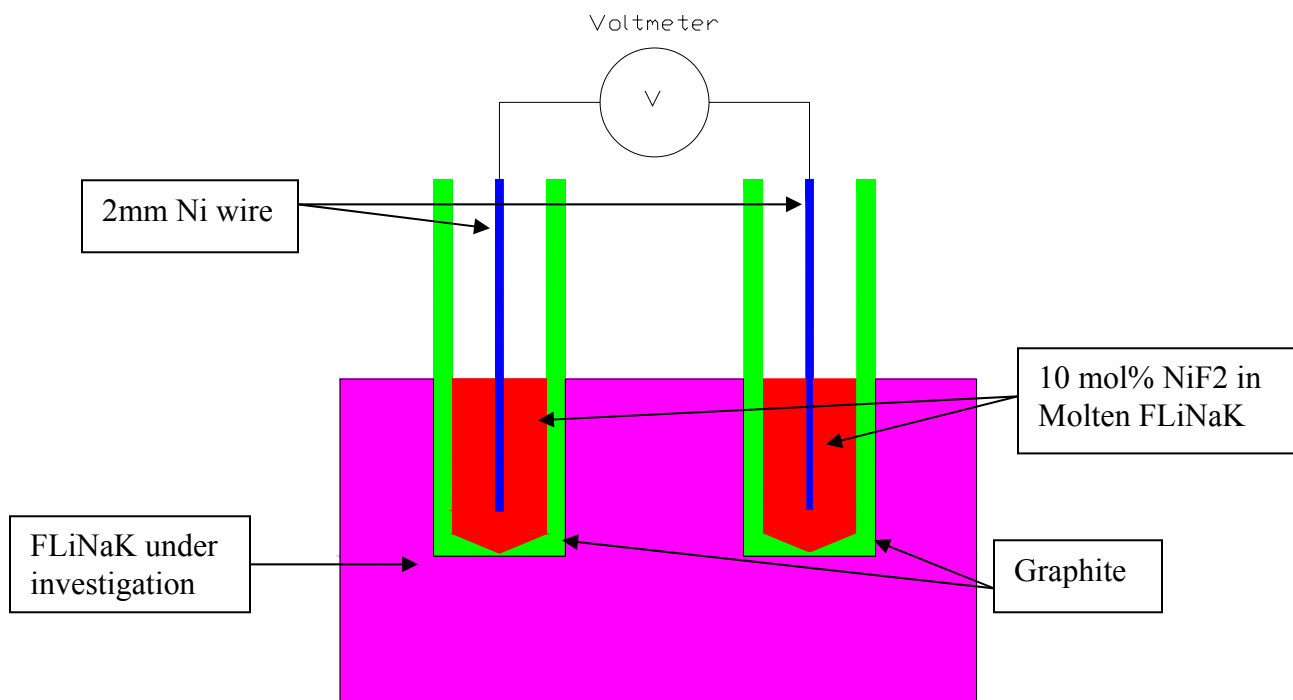
Figure 55. Experimental set-up for measuring the open circuit potential between two RE to determine extent of wetting; the potential difference between the two RE is zero when the RE are fully wetted.

Holes were drilled into the alumina support structure to allow the RE to fit through the alumina but still being held fast. The outer diameter of the RE was 0.42" so the holes were drilled to 0.43". An alumina adhesive was applied to the outside edge of the top of the RE, making a rim that prevented the RE from sliding through the alumina support. Figure 56 shows a picture of the electrode setup. A 1 mm Pt wire was the WE and a coiled Pt wire was the CE. Glassy carbon was the salt container. The Ni wires that sit inside the RE were removed for this picture for ease of viewing. Figure 57 shows a view of the same electrode setup from below with all wires installed.
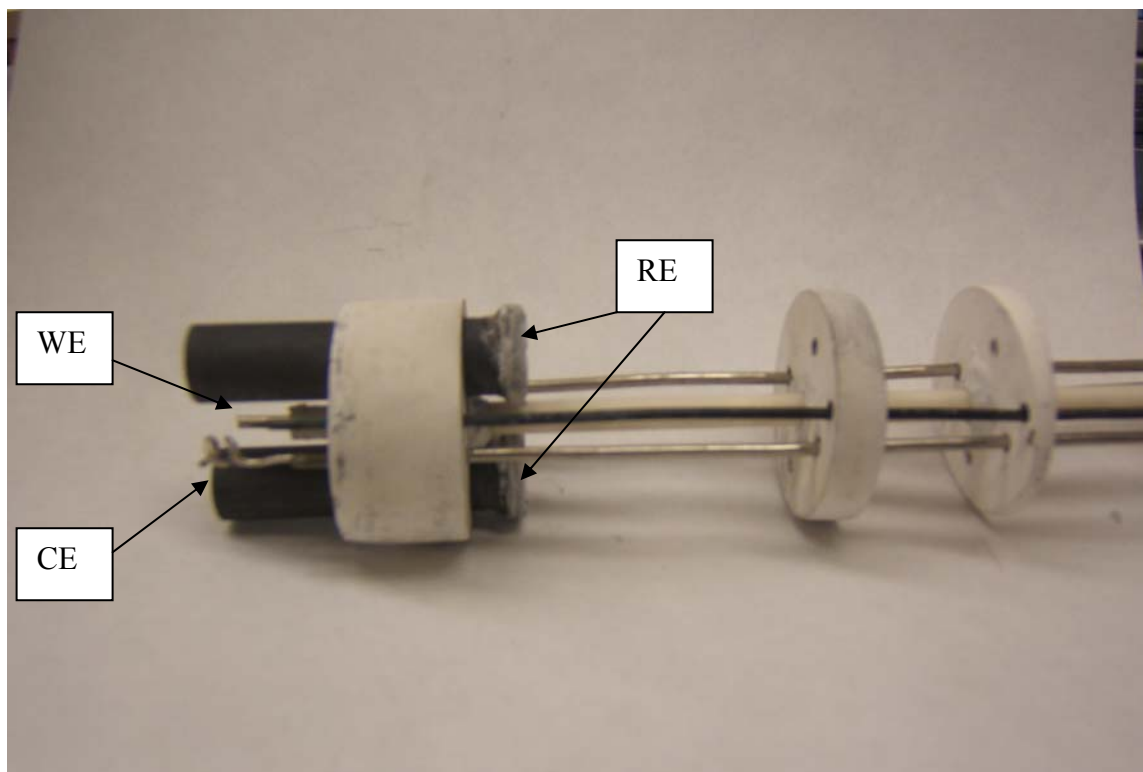
Figure 56. Side view of electrochemical setup using Ni(II)/Ni RE, a coiled 1mm Pt wire as the CE, and a 1mm Pt wire WE.
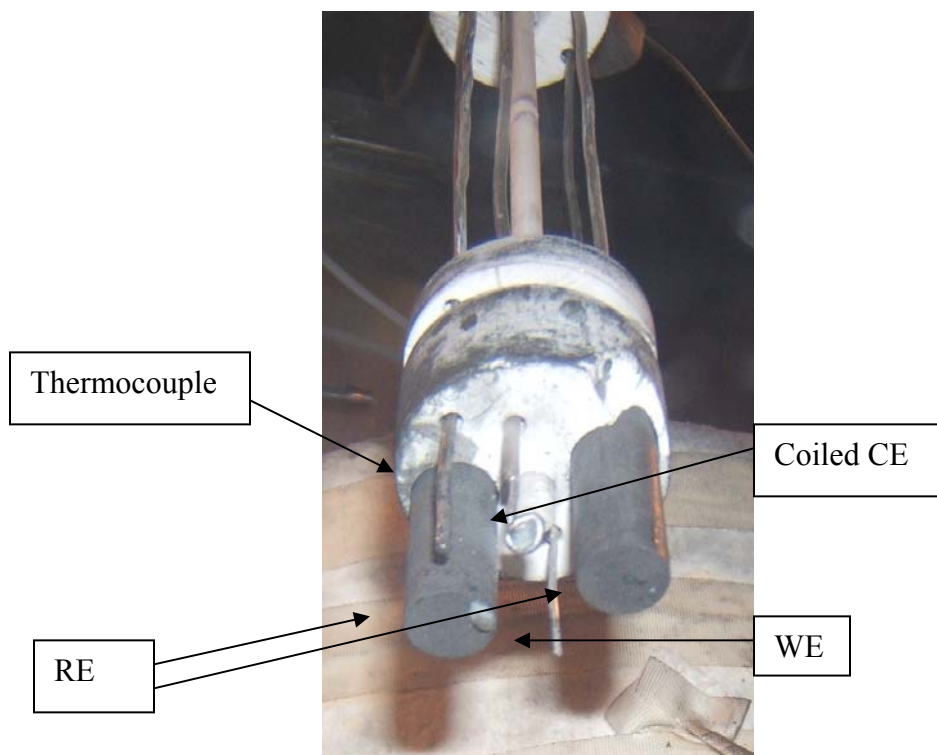
Figure 57. View of electrochemical setup from beneath using Ni(II)/Ni RE, a coiled 1mm Pt wire CE, and a 1mm Pt wire WE.

Wetting times for the porous graphite membrane (acting to ionically connect the RE to the solution while not allowing species to mix) were determined by monitoring the potential difference between the two identical RE. As described in earlier sections, the RE are deemed wetted and ready for use when the potential difference between the two RE reaches zero. Open circuit potential measurements were taken between the two RE for 60 s intervals periodically while the RE were immersed in the salt. When the two RE were initially immersed in the salt, the potential difference between the two electrodes did not reach zero. Figure 58 shows the potential difference between the two RE versus time for the first day (using an average value measured for each open circuit potential measurement). A linear approach to zero was expected, but the unexpected shape of the potential may be due to the mixing of the NiF_2 and FLiNaK inside the RE.
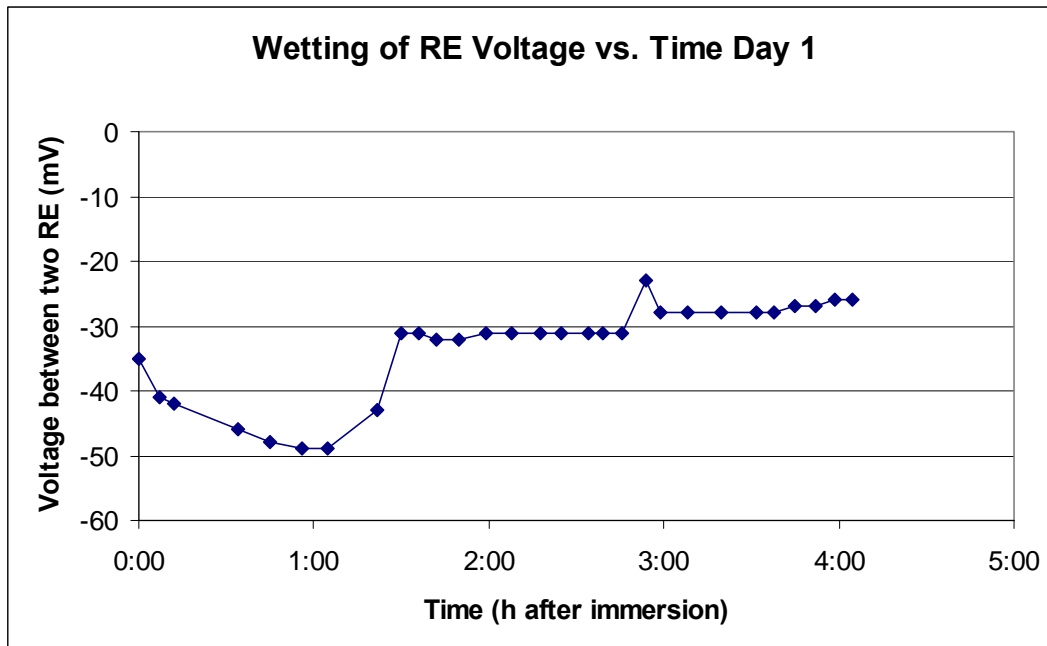
Figure 58. First immersion of RE in salt showed that wetting had not occurred after 4 hours.

After 24 hours the RE were again immersed in FLiNaK. Figure 59 shows potential difference as a function of time for the second immersion. The voltage linearly approached zero for ~4hrs. After that, the potential began to approach zero asymptotically. The RE were allowed to freeze overnight outside of the FLiNaK test crucible and were reimmersed the following morning. Figure 60 shows wetting of the RE.
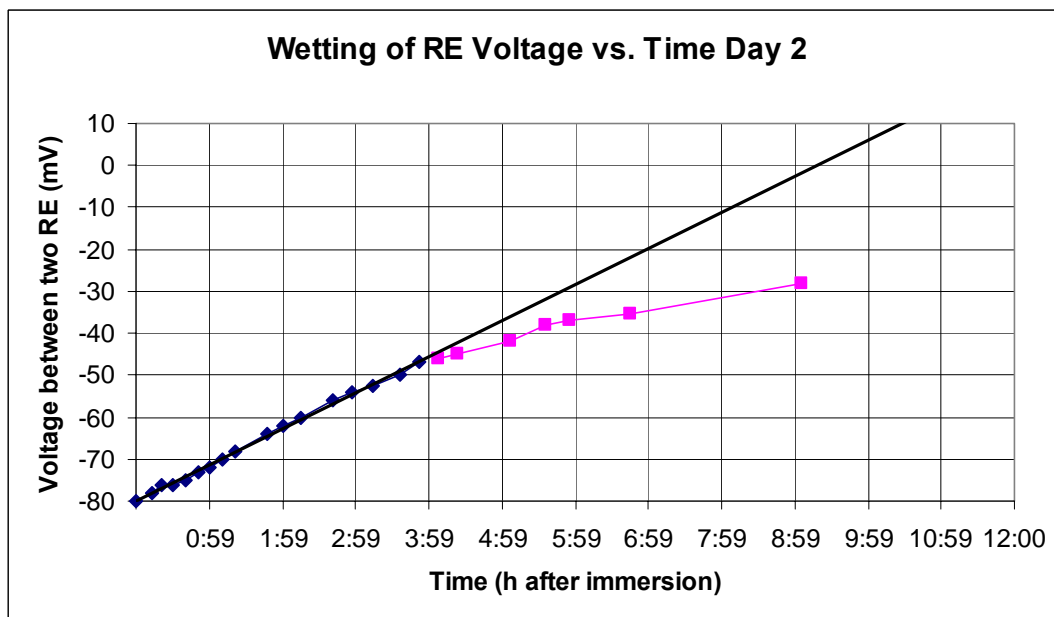
Figure 59. Potential as a function of time for the second immersion of the two RE in FLiNaK. This is the expected behavior of potential difference when wetting is occurring.
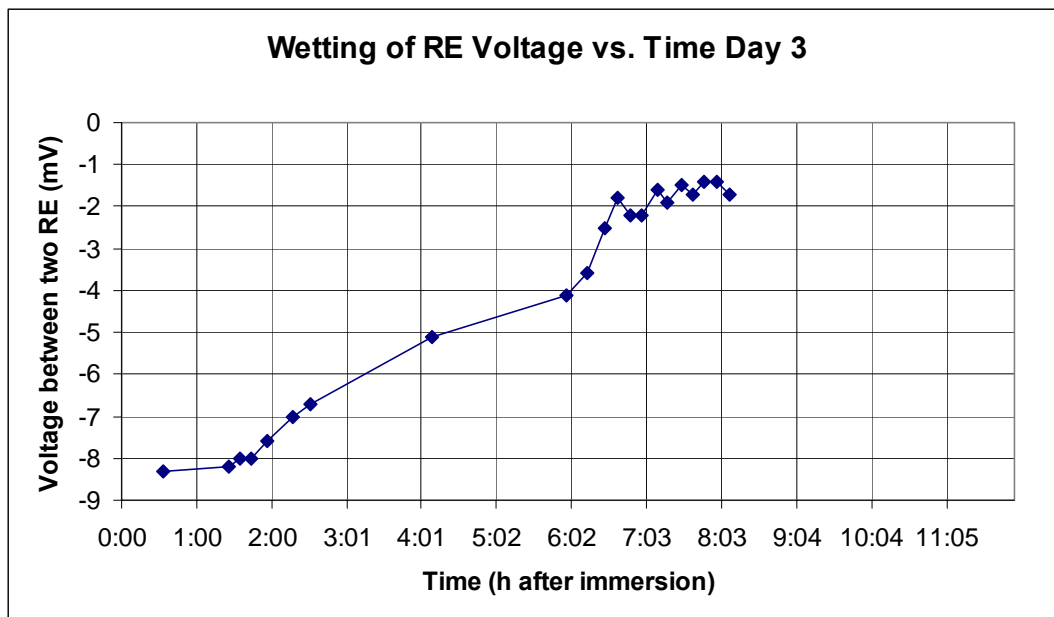
Figure 60. Wetting of RE occurs after 6.5 hours on the third day, a total of 21 hours after the first immersion.

The potential difference between the two RE never fully reached zero; the 2 mV difference could stem from an error in mass of either the NiF_2 or the FLiNaK inside the RE of less than 1 mg. It was deemed that wetting had occurred when the potential difference reached a steady value of ~1.5 mV. Wetting occurred after 6.5 hours on the third day of immersion, that is, after a total of 21 hours after the initial immersion.

The electrodes were again allowed to freeze overnight and wetting of the RE the following day occurred after 3 hours. From this point on, it was determined that the RE were to be kept in the molten FLiNaK to eliminate the need to wait for the RE to wet each morning.

All stripping scans performed when using the Ni(II)/Ni RE had a final potential of 0.3 V, which was then held for 10 s to fully clean the WE. The final voltage of 0.3 V ensured that if any Ni had diffused out of the RE into the FLiNaK, a peak would be detected at 0 V. A peak at 0 V could be identified as Ni because the RE is made from the Ni(II)/Ni couple in FLiNaK. Thus a peak at 0 V vs. the RE would be the same ionic couple as in the RE. If a peak was detected at 0 V, the RE would then be replaced to ensure the purity of the melt. The first set of RE were assumed to be leaking NiF_2 after 300h in the molten FLiNaK when such a peak was found. The RE had been frozen and remelted 12 times.

Working curves were developed for Cr concentrations of 10-300 PPM and 100-2000 PPM using the same method as described for the Pt-QRE. Electrochemical parameters were as follows: a plating potential of -0.7 V vs. Ni(II)/Ni RE, a scan rate was 100 mV/s with a scan range of -0.7 to -0.3 V vs. Ni(II)/Ni RE, a cleaning potential of 0.3 V vs. Ni(II)/Ni RE. NAA samples were taken after each addition. The WE was cleaned between each Cr addition using the procedure described previously. A 1/16" Ni tube was placed in the melt to bubble Ar gas for mixing in an attempt to improve repeatability.

5.g. Neutron Activation Analysis

Neutron activation analysis (NAA) was routinely used in this project to determine the concentration of metal cation impurities in the salt. In NAA the samples are activated by irradiating with a neutron flux and measuring the resulting gamma radiation of an excited isotope as a function of energy. As an irradiated atom decays from its excited state, it emits radiation to return to its ground state. In many cases, that radiation is in the form of gamma rays. Each radioactive isotope has a characteristic set of gamma ray energies. For example, when naturally occurring Fe is irradiated, one of the radioactive isotopes formed from neutron absorption is Fe-59, which then decays via gamma and beta emission to Co-59. Characteristic gamma rays are emitted at 1099 keV with an intensity of 56% and 1291 keV with an intensity of 43%. Gamma ray intensity is the percent chance that a specific gamma ray is emitted each time that a radioactive particle decays in contrast to the standard definition of intensity being the strength or degree of a measurement. In some decays, no gamma rays are emitted (decay via alpha or beta particles without gamma rays) or multiple gamma rays are emitted. In Fe-59, the gamma ray at 1099 keV is more likely to be emitted than the gamma ray at 1291 keV due to its higher intensity. One can infer the presence of Fe in an irradiated sample if a large number of counts are detected at both energy levels with the correct intensity ratio.

Gamma rays can be detected as a function of energy using a high purity germanium detector. Thus, gamma rays from each isotope can be detected and distinguished from each other. Figure 61 shows an example spectrum of the detector output after counting a radioactive sample with a high purity germanium detector. This particular spectrum was obtained from an irradiated FLiNaK sample from a 500 h static corrosion test of Hastelloy-X. A high Cr loss was determined for Hastelloy-X from scanning electron microscope (SEM) and energy-dispersive x-ray spectroscopy (EDS).
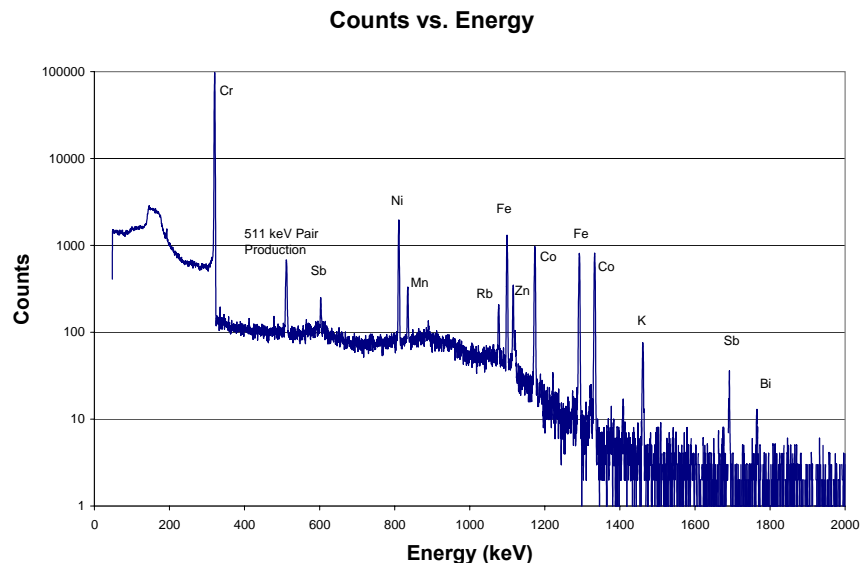
Figure 61. Typical output when counting a radioactive sample emitting gamma rays on a high purity germanium detector (obtained from a FLiNaK sample from a 500h static corrosion test of Hastelloy-X).

The University of Wisconsin Nuclear Reactor (UWNR) was used as the neutron source. Irradiation facilities included a tube that propelled samples with air to allow for short irradiations and immediate counting, as well as a submersed tube to allow for longer irradiations and to provide radiation shielding to the operator post-irradiation. Short irradiations (less than one minute) were performed in the air propelled (pneumatic) tube while long irradiations (two hours) were performed in the submersed (whale) tube. Table 10 shows conditions used for each type of irradiation and the approximate fluxes in each facility.

Table 10. Details of irradiation process used for salt analysis for NAA analysis using UWNR.

Irradiation Facility	Length of Irradiation	Decay Time After Removal from Reactor	Thermal Flux (n/cm^2s)	Epithermal Flux (n/cm^2s)	Fast Flux (n/cm^2s)
Pneumatic Tube	Short (3 sec)	16 minutes	4.44E12	1.28E11	5.87E11
Whale Tube	Long (2 hr)	~2 weeks	7.64E12	3.77E11	1.74E12

5.h. Voltammetry of Cr in Molten FLiNaK Salt

Working curves for Cr concentration as a function of integrated current were obtained by adding Cr in several forms including, addition of CrF_2 and CrF_3 and and pure Cr metal. Working curves were obtained using a Pt-QRE as well as a 10 mol% Ni(II)/Ni RE at 650°C.

The number of electrons transferred (n value) in each peak was identified by cyclic voltammetry (CV). To ensure that the Randles-Sevick equation applied and that the system was reversible, CV was performed at several scan rates to ensure that the peak current was linearly proportion to the square root of the scan rate. Figure 62 shows a compilation of cyclic voltammograms performed at scan rates of 100, 150, 200, and 300 mV/s. The maximum scan rate was chosen to be 300 mV/s due to data collection rate of the potentiostat limiting the detail of the voltammogram. Figure 63 shows a plot of peak current as a function of scan rate for the first peak. For the Cr peaks, the n value calculated for the first peak was exactly double that of the n value for the second peak implying that the first peak was the Cr(II)/Cr(0) reduction and the second peak was the Cr(III)/Cr(II) peak.

Figure 64 to 66 display the plating, stripping, and cleaning steps, respectively
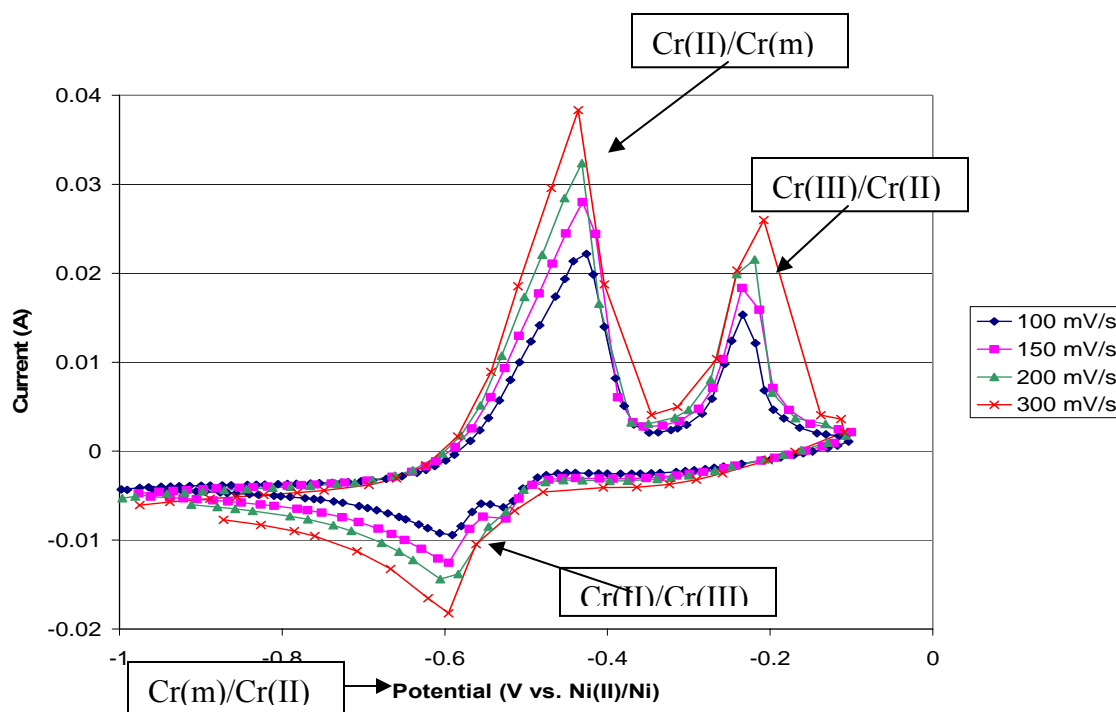
Figure 62. Cyclic voltammograms for increasing scan rates. At 300 mV/s, the potentiostat could not collect data fast enough to provide adequate detail for the first cathodic peak.
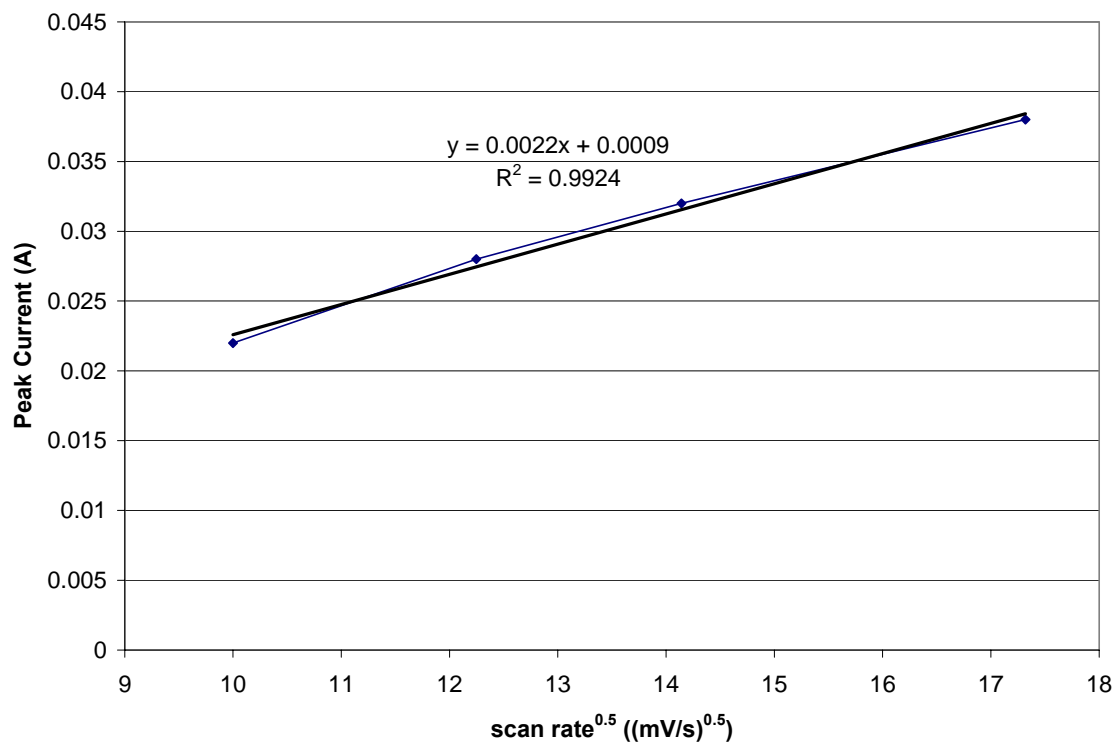
Figure 63. Peak current from CV as a function of scan rate. If the process is reversible, and Randles-Sevick equation applies, the scan rate should be linearly proportional to the peak current.
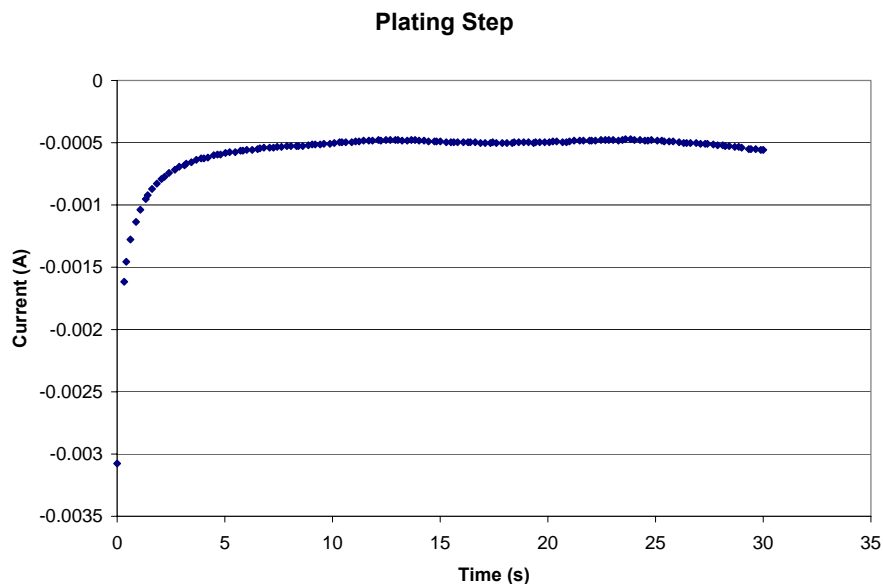
Plating Step

Figure 64. Variation in current as a function of time during the plating step. The current becomes less negative with time as metal cations deplete in the solution.

Linear Stripping of Cr
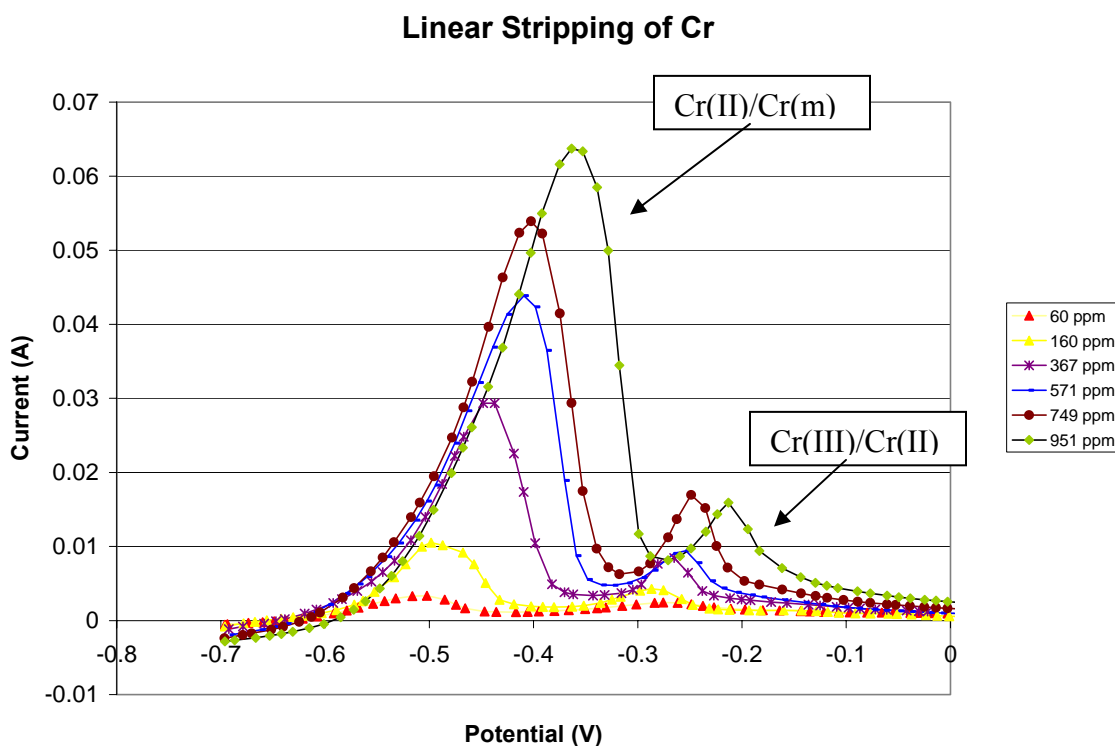
Figure 65. The oxidation of Cr from the WE into solution gives a current peak starting at -0.6 V vs. 10 mol% Ni(II)/Ni RE. As the concentration increases, the area under the peak and the peak voltage increase, but the reduction potential (the starting point of the peak) remains constant.

63
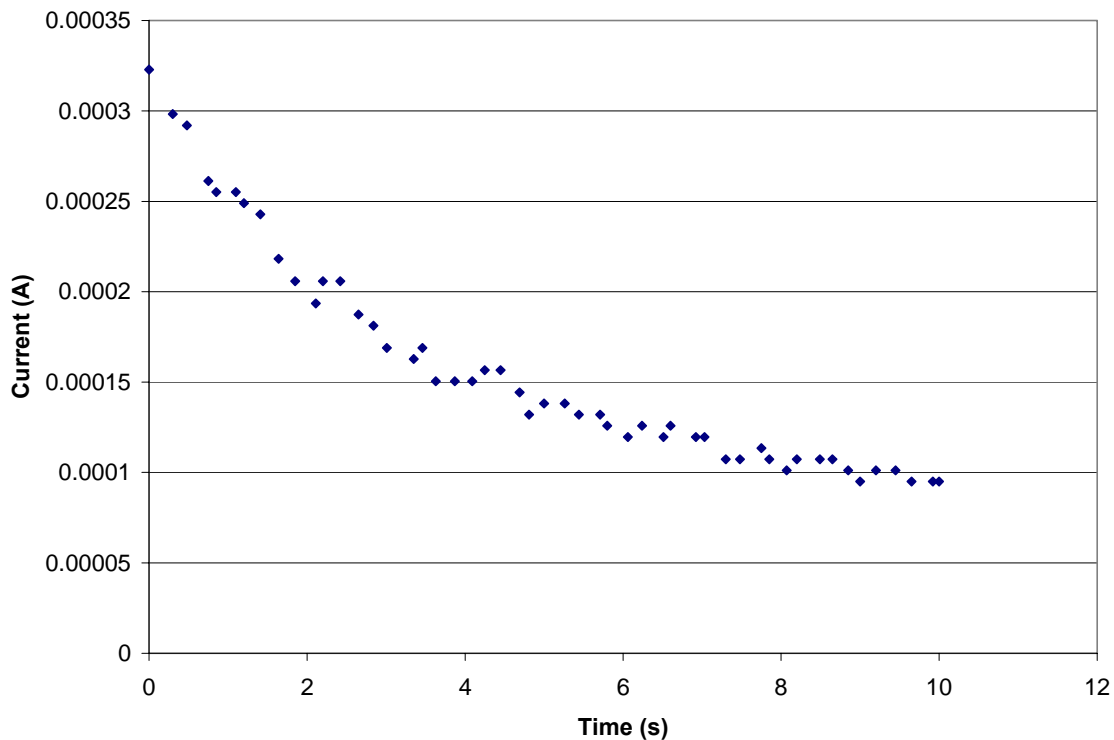
Figure 66. The cleaning step after each stripping step reduced the number of ions plated on the WE. Current decreases as there were fewer ions to oxidize into solution. The cleaning time was long enough to reduce the current to 0.001 A.

A working curve of integrated peak current as a function of Cr concentration was developed for high and low concentrations, as shown in Figures 67 and 68. The uncertainties in the following working curves are due to counting statistics from the NAA for determining concentration. The uncertainty of the potentiostat measurements was determined by taking six ASV measurements at each concentration and calculating the spread in the six measurements.
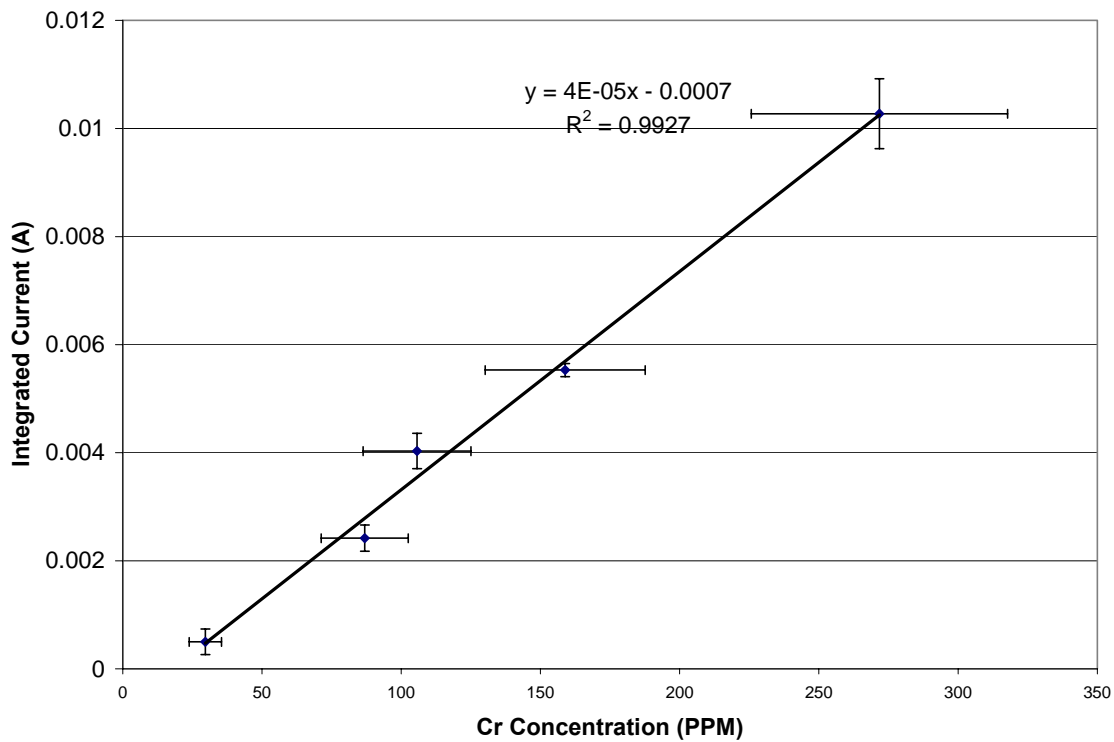
Figure 67. Integrated current as a function of Cr concentration below 300 ppm using Pt-QRE.
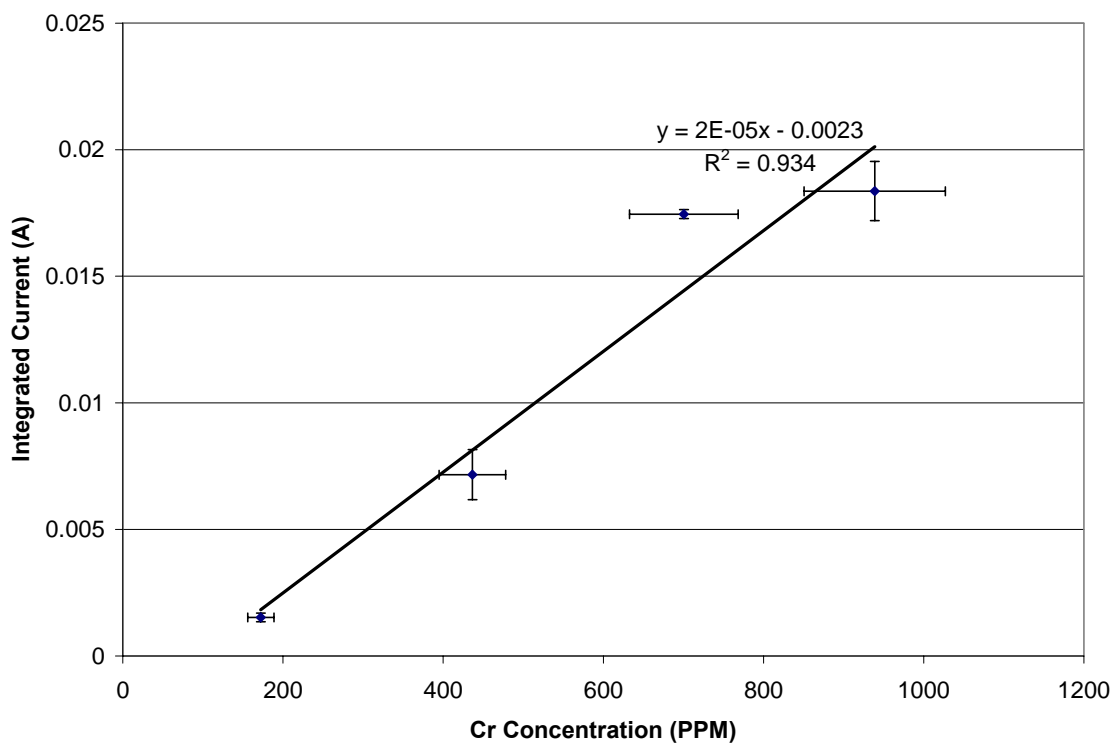
Figure 68. Integrated current as a function of Cr concentration below 1000 ppm using Pt-QRE.

Plating times of 120 s were used at lower concentrations to obtain significant signal-to-noise ratio and decreased to 15 s for higher concentrations. Since current output from the stripping step is directly proportional to plating time, working curves were made of integrated current divided by plating time so that values could be compared for high and low concentrations. The peak current is also directly proportional to the area of the WE so current densities between measurements with different WE areas can be compared by dividing by the area of the WE. Figure 69 shows integrated current density per plating time as a function of Cr concentration over the entire range of Cr concentrations.
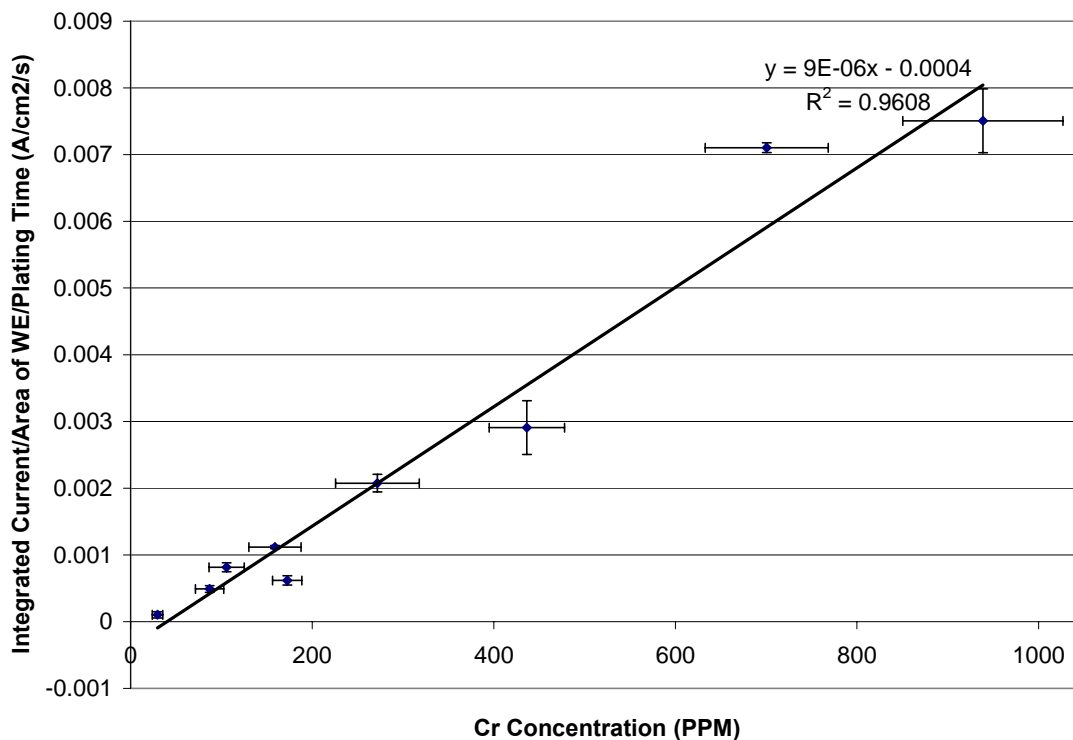
Figure 69. Combination of low and high concentrations of Cr working curves using Pt-QRE.

   Similar measurements of integrated peak current as a function of Cr concentration were made using a Ni(II)/Ni RE for high and low concentrations. Figures 70 and 71 show working curves of integrated current as a function of Cr concentration for low and high Cr concentrations, respectively. Figure 72 combines the two by dividing by area of the WE and plating time.

66
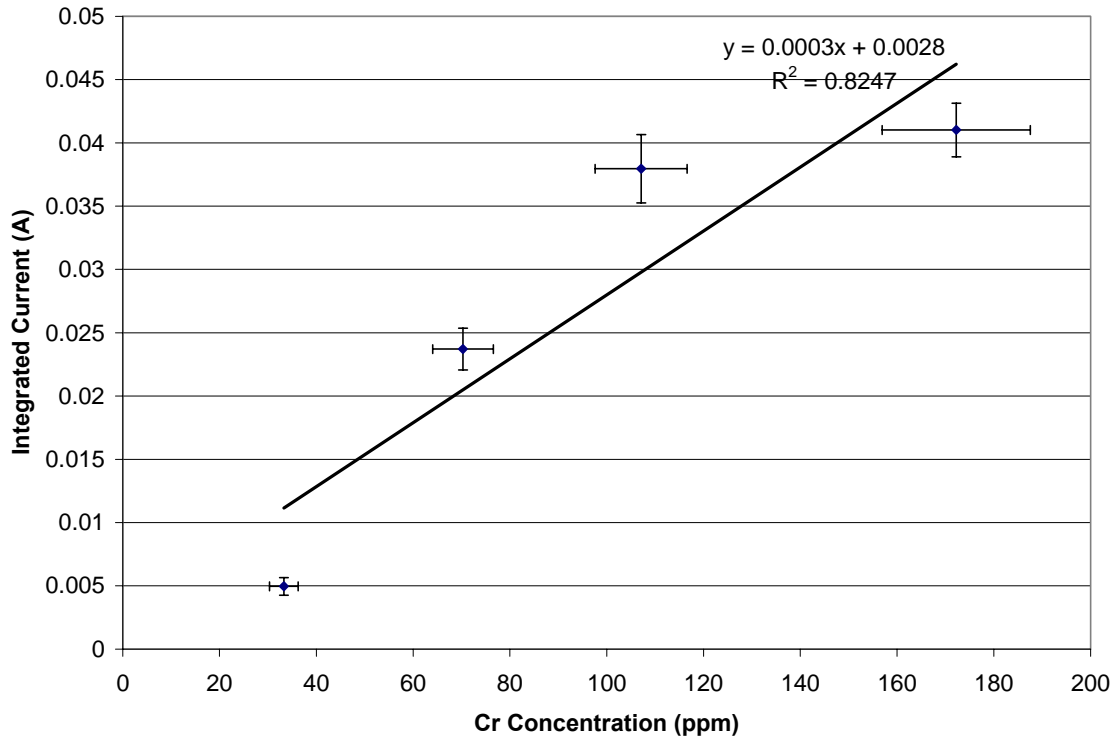
Figure 70. Integrated current as a function of Cr concentration below 300 ppm using Ni(II)/Ni RE.
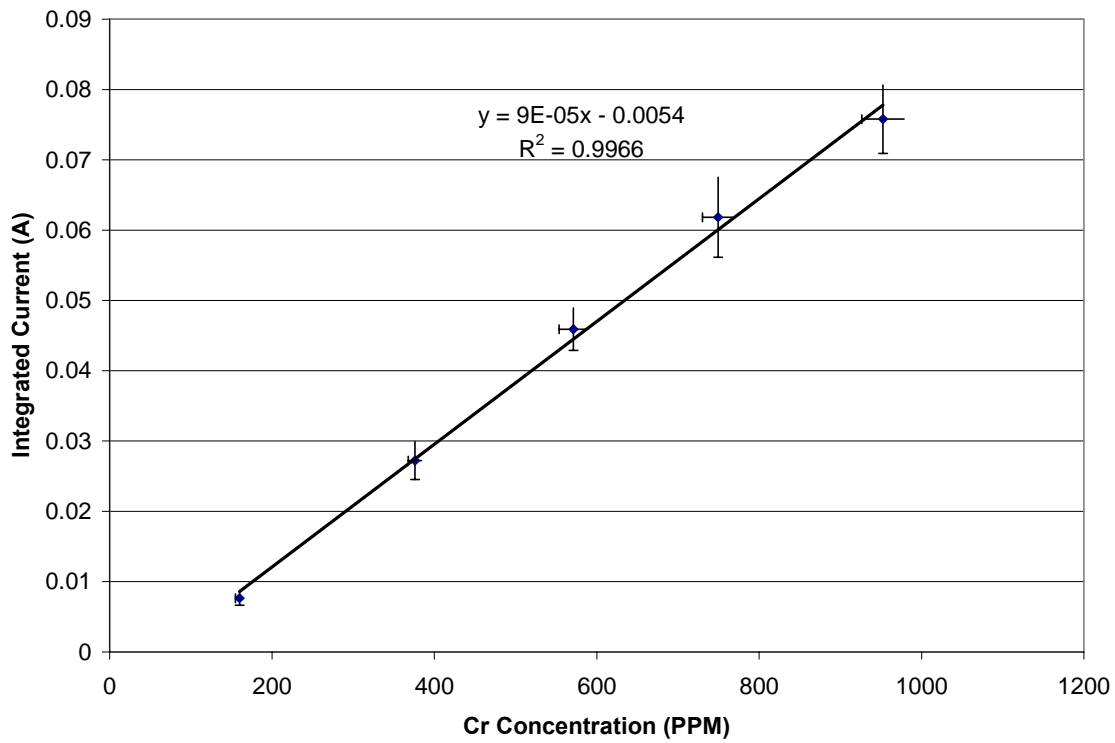
Figure 71. Integrated current as a function of Cr concentration below 1000 ppm Ni(II)/Ni RE.
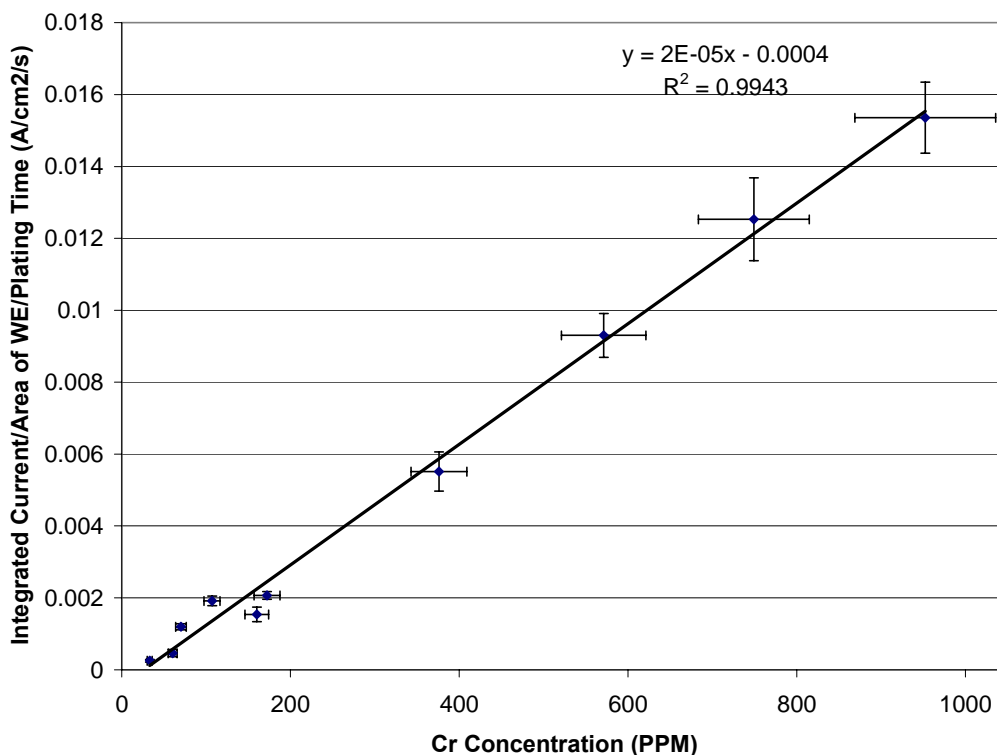
Figure 72. Combination of low and high concentrations of Cr working curves using Ni(II)/Ni RE.

5.i. Voltammetry of Fe in Molten FLiNaK Salt

Working curves for Fe concentrations of 80-595 ppm were obtained using the Ni(II)/Ni RE by adding FeF_2 and FeF_3 at 650°C. At this point, the 1 mol% Ni(II)/Ni RE was employed due to failure of the 10 mol% Ni(II)/Ni RE. A plating potential of -0.1 V was held for 30 s for all measurements. The stripping step consisted of a scan rate of 100 mV/s with an initial potential of -1.0 V and a final potential of 0.5 V. The cleaning potential of 0.5V was held for ~10 s following each stripping step. The actual time was varied to allow the current to drop below 0.0001 A.

At lower concentrations two peaks were seen during anodic stripping corresponding to Fe(II)/Fe(0) and Fe(III)/Fe(II), but only one large peak was observed at higher concentrations. This led to the suspicion that the two peaks were overlapping. To generate the working curve, integrals were taken under both peaks if two were seen. Figure 73 shows a compilation of ASV scans from concentrations of 100-900 ppm Fe. Unlike the comparable curve for Cr concentration, the Fe curves do not all have the same starting point which is caused by the faulty 10 mol% Ni(II)/Ni RE.
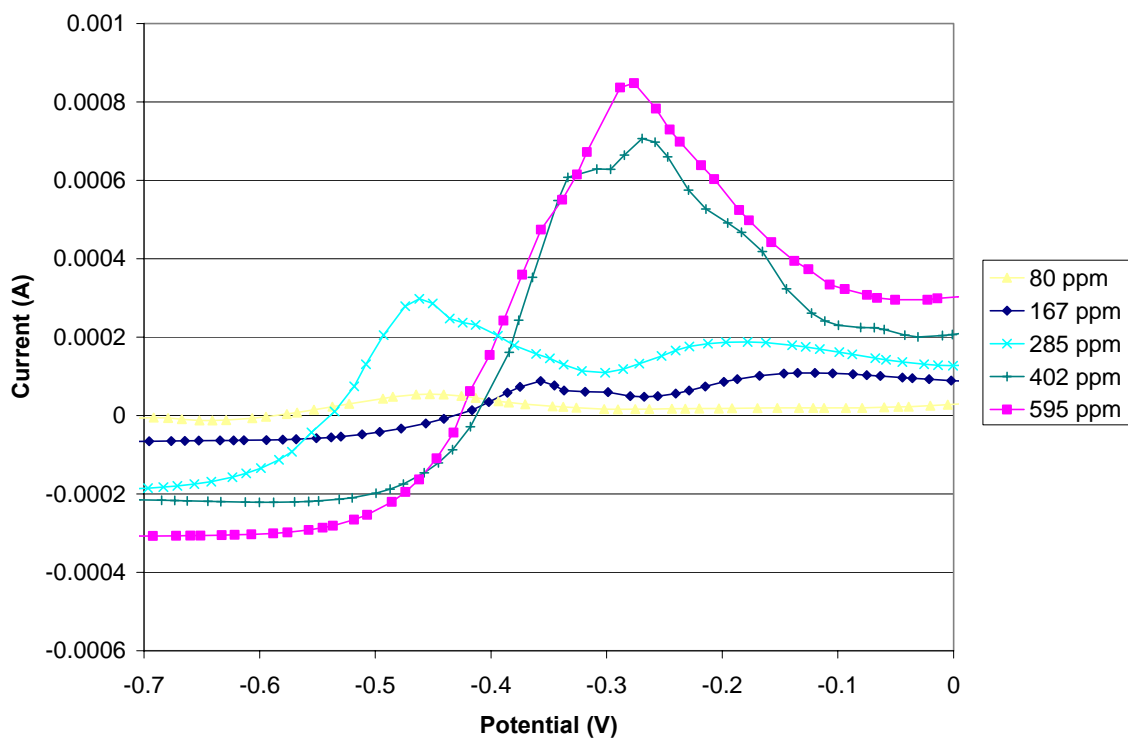
Figure 73. ASV of increasing concentrations of Fe in FLiNaK using a 1 mol% Ni(II)/Ni RE.

Figure 74 shows a working curve of integrated peak current per area per plating time as a function of Fe concentration. When integrating for the 167 and 285 ppm peaks, the integral was taken under both peaks. Cyclic voltammetry was performed for Fe in FLiNaK once the highest concentration was reached. However, electron transfer for each reaction could not determined by this point as only one large peak was observed instead of the two peaks seen at lower concentrations. Figure 75 shows a cyclic voltammogram of 600 ppm of Fe in FLiNaK.
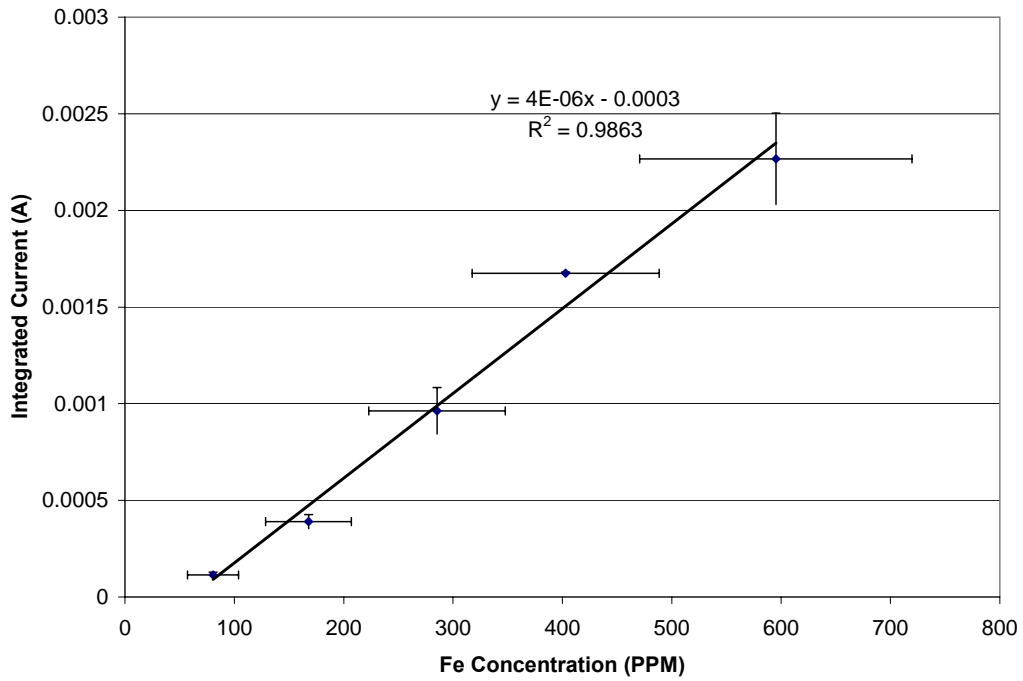
Figure 74. Working curve for Fe in FLiNaK.
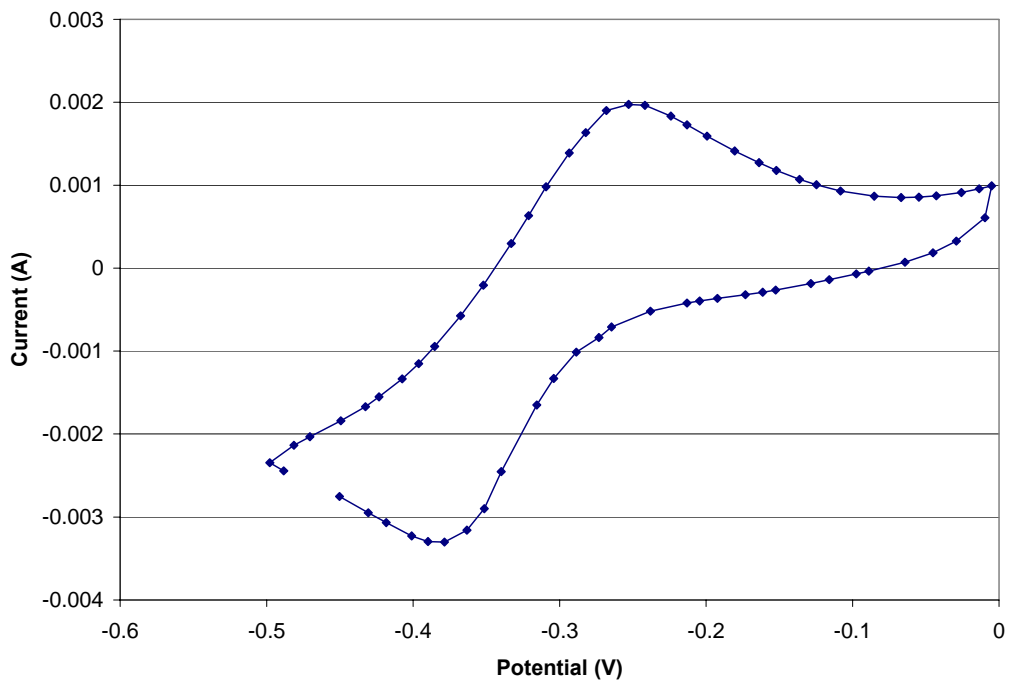
Figure 75. Cyclic voltammogram of Fe in FLiNaK using a 1 mol% Ni(II)/Ni RE.

5.j. Effects of Variations on Electrochemical Cell Parameters

Bubbling was attempted using a 1/16" Ni tube. Since the plating step is diffusion controlled, it was thought that bubbling Ar gas the melt might increase the diffusion of ionic species to the WE. However, bubbling had no effect as repeatable results were obtained independent of whether the melt was being bubbled.

ASV was performed in glassy carbon, graphite, and Ni 200 crucibles under an Ar atmosphere. Once frozen, the salt slid out of the glassy carbon and graphite containers easily where as the salt would not fall out of the Ni crucible. The salt eventually came out when the crucible was repeatedly tapped with a wrench. **Tests were repeatable between all three crucibles.**

Effects of varying the distance between the WE and the RE were tested by bending the WE nearer or further away from the RE. However, due to the low resistance in the solution, no differences were seen between the measurements.

6. MOLTEN SALT HEAT TRANSFER AND FLOW LOOP

6.a. Joining of Graphite for High Temperature Molten Salt Applications

Graphite is currently being evaluated as a material of choice for the main components of a thermal-poly loop. Graphite is a chemically compatible material for use with molten salts and retains its strength at temperatures well above 2000°C.

Three main concerns with the use of graphite as a structural material are: oxidation, ability to withstand stresses induced by differential thermal expansion, and the ability to join the pieces of the machined graphite. The graphite loop would be in a controlled environment. This would reduce the risk of oxidation, but would restrict access to the loop when temperatures are much above 300°C. Researchers in France have reported studies with a graphite loop in a molten salt environment, however, leaks at the joints were reported as a problem during the operation of the loop [32]. New technologies may aid in more effective joining of graphite components than typical threading. For example, a graphite epoxy, Resbond 931-1, forms a 99.9% pure graphite bond and was evaluated as a possible method for joining graphite components. Small capsule tests were conducted to evaluate the strength and chemical compatibility of this epoxy in FLiNaK environments up to 1000°C.

6,a.i. Capsule Design

The design of the experimental capsule is shown in Figure 76. A 1" piece of graphite was machined from 3/8" diameter POCO grade AXZ-5Q1 graphite rods. The plug was machined from ¼" diameter graphite of the same grade as the 3/8" stock. The design called for a 0.001" difference in the diameter of the plug and capsule hole to allow spacing to fill the epoxy.
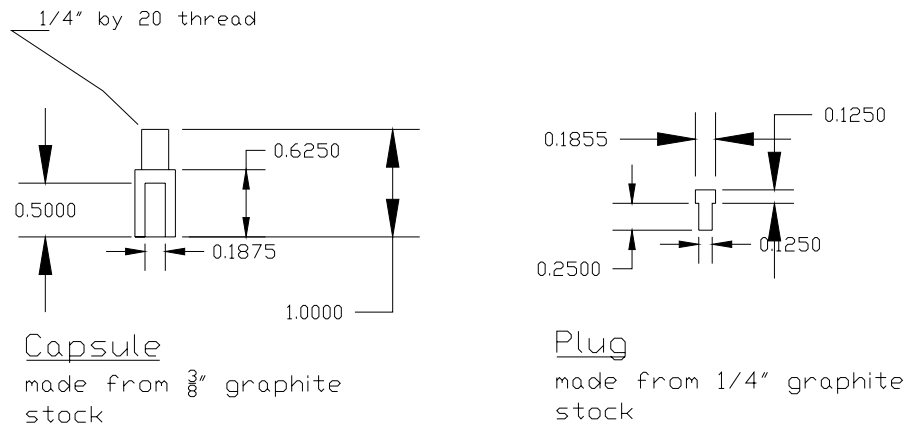
Figure 76. Stress capsules showing the design of individual pieces for the graphite capsule and plug machined from POCO graphite.

The graphite was cleaned after machining to remove oils and dust from the pieces. For this, graphite was ultrasonically cleaned three times in methanol for 5 minutes per each cleaning step. This was followed by ultrasonically cleaning three times in water also for 5 minutes per cleaning step. The pieces were then placed in a tube furnace and baked at 260°C for 12 hours to expel excess moisture. The graphite pieces were then ready for the application of the high temperature epoxy.

The Resbond 931-1 epoxy is a two-component epoxy, binder and graphite powder. The epoxy is created by mixing 100 parts powder to 35 parts binder, on a weight basis. The mixed epoxy was then placed around the 0.1855" portion of the plug and the plug was inserted into the 0.1875" bore in the capsule. The epoxied surfaces were wetted with binder before the application of the epoxy in order to promote adhesion. The excess epoxy was removed from the end of the plug.

The recommended curing process for the epoxy called for 4 hours at room temperature, 4 hours at 100°C followed by 16 hours at 130°C. To achieve maximum strength, the epoxied graphite pieces were baked in an inert glove box for 2 hours at 1000°C. The epoxy manufacturer, Cotronics Inc., recommended post-curing at 200°C.

After the final curing, the graphite pieces were kept in the inert glove box until they were tested. The capsules were threaded into the bottom of the graphite rod as shown in Figure 77. This graphite rod extended above the heater insulation where an alumina-silicate (LAVA) rod was threaded onto the top of the graphite rod. The alumina-silicate was used as an insulating material to keep the heat away from the linear bearings. A Celesco CLP-25 LVDT was used to measure the linear displacement of the plug as lead weights were added to the top. Test weights were added to the necked down section of the steel piece at the top of the test section.
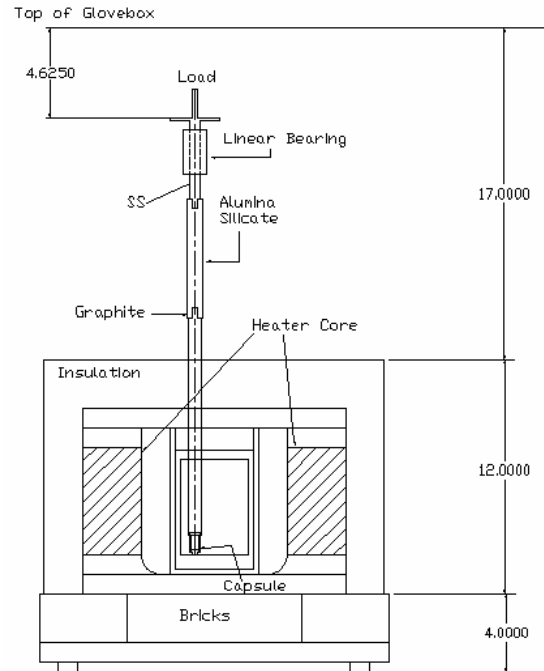
Figure 77. A cross-sectional view of the experimental setup showing the capsule loading apparatus used for testing of the strength and compatibility of Resbond 931-1 graphite epoxy in molten FLiNaK salt. All dimensions are in inches.

Capsules were tested in three different environments; 25°C in argon environment, 1000°C in argon environment, and 1000°C in molten FLiNaK environment. This was done to separate the temperature effects from the environmental effects of the salt on the epoxied graphite. Temperature and LVDT data from the tests was recorded using a LABVIEW computer program.

Two larger capsules were built out of 1" graphite rod as shown in Figures 78 and 79. These two capsules were placed in the salt environment for 111 hours at 1000°C to determine the effects of an extended exposure to the salt environment without any additional stress on the graphite epoxy. Stainless steel tubing was placed in the bore in the graphite to keep the graphite from floating. This ensured that the graphite epoxy would remain in contact with the molten salt.
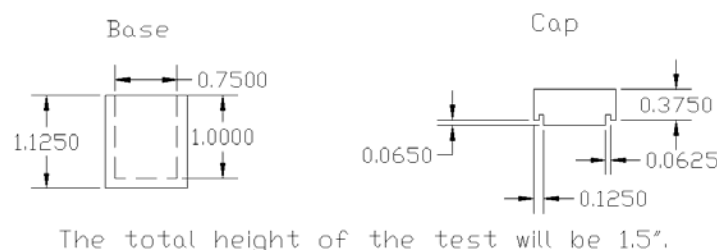
Figure 78. Two capsules (such as shown above) were placed in the molten salt with no external loading to determine if the epoxy would be susceptible to attack by the molten salt if exposed for extended periods. Dimensions are in inches.

A

B

C

D

Figure 79. (A) the capsules for the extended time tests before the metal pieces were put in the salt, (B) the sealed capsules in the large graphite crucible with FLiNaK chunks, (C) the capsules after being removed form the crucible, and (D) the capsules and the metal pieces after the capsules were cut open.

6.a.ii. Results of Capsule Tests

Twenty-eight capsules were built and tested to failure: four capsules at room temperature, five capsules at 1000°C in argon environment, and nineteen capsules at 1000°C in molten FLiNaK environment. The capsules that were tested in these three environments will be referred to as RT, HT, and MS for room temperature, 1000°C argon, and 1000°C FLiNaK environments, respectively. In order to determine the time and loading when the capsule broke, an additional weight was added onto the cell only after three minutes had elapsed since the previous weight had been added. The time and reading from the LVDT was recorded after the weight was added. This allowed for the determination of time and weight for failure.

The results from these 28 different capsules are shown in Table 11. The reported stress is an average of the failure stress and the previous stress before failure. For example, capsule MS-A-3 failed at a loading of 6134 psi. The loading just prior to failure was 5926 psi. The average of these two stresses, 6030 psi, is the reported value in Table 12. Different letters are used to distinguish different sized areas that were epoxied.

Table 11. Results of the graphite epoxy capsule tests. The maximum strength shows a wide variation in each of the different environments. The B capsules have a larger epoxied surface area than the A capsules.

Capsule	σ_{max}	Capsule	σ_{max}	Capsule	σ_{max}
RT-A-1	< 394	HT-A-1	> 5400 psi	MS-C-1	< 394
RT-A-2	< 394	HT-A-2	1264	MS-C-2	4838
RT-A-3	> 5400 psi	HT-A-3	4575	MS-C-3	720
RT-A-4	1264	HT-A-4	> 5400 psi	MS-C-4	6030
RT-A-5	> 5400 psi	HT-B-1	> 4737 psi	MS-D-1	5095
RT-A-6	> 5400 psi			MS-D-2	< 394
				MS-D-3	3892
				MS-D-4	2048
				MS-E-1	5077
				MS-E-2	< 394
				MS-E-3	< 394
				MS-E-4	4021
				MS-E-5	5894
				MS-E-6	3873
				MS-E-7	5151
				MS-F-1	1568
				MS-F-2	4368
				MS-F-3	< 394
				MS-F-4	< 394

The results in Table 11 show that for each of the three environments there is at least one capsule that failed at a lower stress than the remaining capsules. For the case of the epoxy tested in FLiNaK, over half of the samples (ten out of 19) failed before the manufacturer's quoted stress of 2500 psi. The reason for the lower fracture stress is not entirely clear, but it is speculated that it could be due to small differences in the machining tolerances, or slight differences in the application or mixing of the graphite epoxy. The tolerances of the D, E, and F capsules was measured to try and to remove machining tolerances as the reason for early failure. Table 12 lists the average values and the standard deviation for the capsules.

Table 12. The average diameter and lengths for the set of graphite capsules tested have been recorded. The capsule set D has a slightly larger diameter due to a larger diameter of the test capsule.

Capsules	Avg. Diam. (in)	95%	Avg. L (in)	95%
D	0.2049	0.0018	0.1316	0.0011
E	0.1860	0.0015	0.1254	0.0016
F	0.1845	0.0011	0.1301	0.0012

In light of the continual success of some of the capsules, it was assumed that the application of the epoxy to the graphite is the most important aspect of the process. Further research is needed to determine the best method to apply the epoxy to the surfaces that are to be joined.

The extended time test samples were cut open to be able to section the graphite for microscopic analysis. Examination of the metal pieces inside the graphite capsule indicated that the salt did not penetrate through the epoxy.

The chemistry of the salt did not change with the addition of the epoxied graphite pieces. This was determined by the fact that the salt did not penetrate the surface at regions where the capsule and the graphite rod came into contact. A reducing salt (which would have been a result of epoxy dissolution in the salt) would have been able to penetrate the gap where the two graphite pieces came into contact.

6.b. Heat Transfer Calculations

6.b.i. Previous Literature

Convective heat transfer of molten salts has been evaluated over a four-decade period by Hoffman at ORNL [33], Grele at NASA [34], Vriesema at Delft University in the Netherlands [35], and by Ignat'ev in Russia [36]. These studies have shown that molten salts follow the general correlations of turbulent heat transfer of fluids as described by the Dittus-Boelter and Chilton-Colburn models. The physical properties of the FLiNaK salt for analyzing the data were different in these studies. Most notably, a large variation in the accepted thermal conductivity of FLiNaK salt can be seen from the 1950's to the accepted value today [37]. In addition, each investigator used different metal containers for their tests. Hoffman looked at heat transfer of FLiNaK salt in nickel, 316 stainless steel, and Inconel tubes. Grele used Inconel X tube, Vriesema Inconel 600, and Ignat'ev Kh18N10T. A summary of the experimental conditions for these experiments is listed in Table 13.

Table 13. Experimental data showing the range of values that were investigated for convective heat transfer of FLiNaK salt.

	Hoffman			Grele	Vriesema	Ig'natev
Metal	Ni	SS – 316	Inconel	Inconel X	Inconel 600	Kh10N18T
D (cm)	0.2985	0.4572	0.4445	0.6223		0.3
Reynolds	2400 - 5600	6600 – 9500	2800 - 8337	2000 - 20000	14000 - 93000	5000 - 15000
Fluid Temperature (°C)	527 - 734	722 – 745	646 – 702	540 - 729	575 - 675	550 - 650
Surface Temperature (°C)	535 - 753	733 – 753	662 – 727	570 - 793		
Q" (kW/m^2)	73 - 604	250 - 355	29 – 540	28 - 606	n/a	30 - 60
Prandtl	5.1 - 17.1	4.9 – 5.4	6.0 – 8.0	5.2 - 15.6	6.9 – 12.3	
Orientation	Horizontal			Horizontal	Vertical	Vertical
Heat / Cool	Heating			Heating	Cooling	Heating
# of Runs	10	7	12	52	33	45

The results of the heat transfer experiments in the Ni and SS-316 tubes varied from the results obtained in the different Inconel tubes. Originally, the difference was attributed to a film formation on the Inconel surface. It has since been found that molten salts do not form a film [37], thus the cause for the difference in heat transfer in the different metal tubes is unexplained. It is believed that all of these

alloys should interact similarly with the salt due to approximately the same levels of Cr in their compositions as shown in Table 14.

Table 14. Nominal composition of the alloys used in the forced convective experiments.

Alloy	Fe	Ni	Cr	C	Mn	Al
Inconel 600	8	74.5	15.5	0.1	1	
Inconel X	7	73	15.5	0.04	-	0.7
AISI 316	64	12	18	0.08	2	
Kh18N10T	72	9	19	-	-	-
Nickel	0.25	99.5		0.07	0.35	

The radiant heat transfer of FLiNaK has also been reported on by Ewing at the U. S. Naval Research Laboratory [38]. Thermal conductivity measurements of FLiNaK were performed using a vertical apparatus that contained an inch gap filled with FLiNaK between two Inconel surfaces. It was found that the thermal conductivity of the salt changed drastically during the experiment. It was then realized that the thermal conductivity measurement contained a molecular conductivity term and a radiation term from the hot to cold Inconel surface. It was concluded that FLiNaK is transparent to infrared radiation when pure. The salt did not absorb the radiation emitted from the hot surface. As corrosion products in the salt accumulated, the transparency of the salt decreased.

6.b.ii. Salt Properties
The accepted physical properties for FLiNaK salt have varied over the course of the past 50 years. Even today some variation [37] is found in the values that are used to evaluate this molten salt. The following are some equations to describe how the salt properties of FLiNaK change with temperature over the following ranges. Equations 1 – 5 have been used in the preliminary design of the molten salt loop:

ρ [kg / m^3] = 2729.4 – 0.73 T[K] [23](1)

μ [Pa s] = 4 * 10^{-5} exp (4170 / T[K]) [23](2)
<div align="center">Valid for 500°C < T < 800°C</div>

C_p [J / kg K] = 979.2 + 1.066 T [24](3)
<div align="center">Valid for 477°C < T[K] < 587°C</div>

k [W / m K] = 0.36 + 0.00056 T[K] [25](4)
<div align="center">Valid for 517°C < T < 807°C</div>

h [J / kg] = $\int Cp(T)dT$ (5)

6.b.iii. Heat Transfer Calculations
The data from Hoffman [33], Grele [34], and Vriesema [35] were evaluated using different values for the physical properties. Each set of data was re-evaluated using the same physical properties to compare the data from the different investigators. The properties that were used to compare the data were Equations 1 and 2 for density and viscosity, respectively, and with the values for k and C_P of 0.6 W/m K and 1.88 kJ/kg K, respectively. Several different analyses were conducted with the data to try and get the best fit between the experimental data and the Dittus-Boelter Correlation. It should be noted that the report by Ignat'ev did not give physical properties or test data to allow for comparison of the experimental data with the other reports.

The first analysis only looked at the data obtained by Hoffman [33] and Grele [34] to determine why an offset in the convection coefficient was seen in the different metal tubes. The data from the molten salt heat transfer experiment showed a different convective coefficient if the salt was flowing through an Inconel tube versus a stainless steel or nickel tube. The data was analyzed in three different ways to determine if thermal radiation was a cause for the offsets seen in the experiments. First, the thermal conductivity was varied to obtain the best fit of the reported data to the Dittus-Boelter relation

$$\mathrm{Nu}_D = 0.023\,\mathrm{Re}^{0.8}\,\mathrm{Pr}^{0.4}. \quad (6)$$

Second, a convective term for the approximation of radiation heat transfer was computed according to,

$$h_r = 4\varepsilon_1 \sigma \overline{T}^3, (7)$$

and used in parallel with the convective term for flow with the same reference temperature to obtain:

$$Q'' = h_T\left(T_1 - T_\infty\right), (8)$$

where $h_T = h + h_r$. The amount of energy absorbed by the salt, ε_1, was varied until the difference in the reported and calculated heat flux was minimized. Finally, effective thermal conductivities were computed using Equation 9, from work done by Ewing [38], and Equation 10 from a slight manipulation of Equation 7:

$$k_{eff} = k_m + F\Delta x C_t \sigma \left[\frac{T_S^4 - T_F^4}{T_S - T_F}\right], (9)$$

$$k_{eff} = k_m + \left(4\varepsilon_1 \sigma \overline{T}^3\right)D. (10)$$

This effective thermal conductivity was used in Equation 7. The amount of energy absorbed by the salt was varied by changing C_t in Equation 9 and ε_1 in Equation 10 until the best fit was obtained to the experimental data. As an example, the data shown in Table15 was obtained from forced convection in an Inconel X tube as reported by Grele [34].

Table 15. Sample convective heat transfer data. This data was obtained from Grele [18] and the values were converted to SI units for analysis.

Run	T_{Fin} (K)	ΔT_F (K)	T_W (K)	T_S (K)	W ($^g/_{sec}$)	V ($^m/_s$)	G (kg/s/m^2)	Q (W)	Q/S (W/m^2)	h (W/m^2/K)	Nu	Pr	Re
49	968.2	28.9	1060.9	1048.7	107	1.77	3.49E+03	6462	540E+03	8168.9	11.3	1.3	7558

The value for the thermal conductivity that was used by Grele is off compared to the values used today, as described earlier. The values of the physical properties that were used by Grele and the values that were used in this calculation are shown in Table 16.

Table 16. Salt properties used by previous investigator and the analysis in this study.

Property	Grele	Used in this Analysis
Density, ρ (kg/m^3)	2555 - 0.6 * T(K)	2729.4 – 0.73 * T(K)
Thermal Conductivity, k (W/m K)	4.6	0.6
Heat Capacity, C_P (kJ/kg K)	2.09	1.88
Viscosity, μ (Pa s)	$2.5 * 10^{-5} * \exp^{(4790/_{T(K)})}$	$4.0 * 10^{-5} * \exp^{(4170/_{T(K)})}$

With these values, the values for Nu, Pr and Re numbers were recalculated and found to be 76.39, 8.73, and 7791, respectively.

Vary Thermal Conductivity: The value of the thermal conductivity was varied until the predicted value from the Dittus-Boelter Equation, Equation 6, was equal to the experimental data. The value of k that satisfies this for this set of data is $k = 0.677$ W/m K.

Heat flux balance using Equations 7 and 8: The amount of radiation that was absorbed by the salt was varied until the heat flux was balanced for experimental and calculated values. It was found that the salt would have to absorb 8.5 times more radiation than the walls were emitting.

Use k effective from Equations 9 and 10: The value of C_t and ε_1 were allowed to vary to produce an effective thermal conductivity that when placed in the Dittus-Boelter equation would obtain the same result as part 1. Results are shown in Table 17.

Table 17. The values of the variables in Equations 9 and 10 that give the best fit for the data.

ε_1	k_{eff} (W/ m K)	C_t	k_{eff} (W/ m K)
0.0534	0.677	0.927	0.673

Further analysis of the forced convective heat transfer of FLiNaK salt was performed, including data measured from Vriesema [35] from Delft University in the Netherlands. All the data was re-analyzed using Equations 1, 2, and 4 for the values for the density, viscosity, and thermal conductivity, respectively, of the salt and 1.88 kJ/kg K for the heat capacity. The re-analyzed data can be seen in Figure 80.
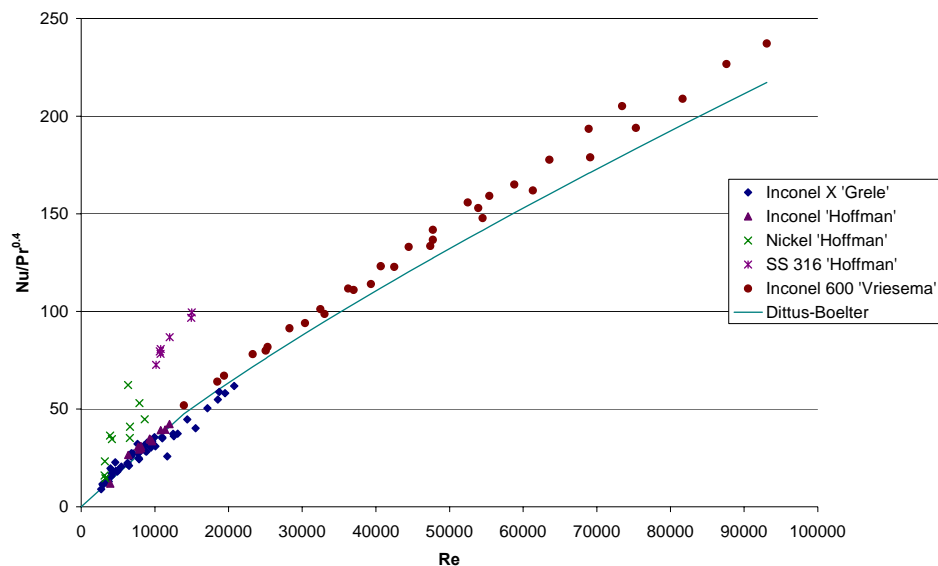

Figure 80. The data for convective heat transfer for the Inconel test tubes falls within the expected range of ±10% when compared to the Dittus-Boelter correlation. The heat transfer data taken with Ni and SS-316 tubes is still significantly offset from the predicted and experimental values for the other material tubes.

The Dittus-Boelter correlation over predicted the measured heat transfer of the salt within 3% and 10% for the values obtained by Hoffman and Grele, respectively, in the Inconel tubes and under-predicted the heat transfer seen in the Inconel 600, Ni, and SS-316 tubes by 8%, 33%, and 50%, respectively. The Ni and SS-316 tubes showed an offset compared to the data for the other tests. This difference in the heat transfer from the SS-316 and Ni tubes should not exist since molten salts do not form a film. The data was examined to determine the reason for the difference in heat transfer between the metal containers.

Two different methods were used to compare the data for the nickel and stainless steel would agree with the Dittus-Boelter correlation, radiative heat transfer and computer modeling. The amount of energy expected to be transferred to the salt by radiation was computed and compared to the energy transferred by convection using the Dittus-Boelter correlation. Finally, the test sections of each of the metal surfaces were modeled using FLUENT (a 3D Navier-Stokes code) to predict the heat transfer. The results obtained were compared to the actual data and the Dittus-Boelter correlation.

In order to determine how much energy was transferred to the salt by radiation, an effective absorption was determined from work done by Ewing [38]. The values for the transmittance coefficient of FLiNaK to radiant energy varied from 0.86 to 0.5 as the impurities in the salt built up, and this correlates to values of 0.06 cm^{-1} to 0.27 cm^{-1}, respectively, for the attenuation. A radiation heat transfer term was determined, Equation 8, and used to compare the amount of heat transferred by radiation and from convection. For each set of data, h_r, accounted for less than 0.6% of the heat transferred to the salt using $\alpha = 0.27$ *cm*$^{-1}$ and $k = 0.6$ *W/m K*. This analysis therefore suggests that radiant heat transfer to the salt from the different metal tubes was not the reason for the offset in the data for the different metal containers.

A 2-D computer model of each test section used by Hoffman and Grele [33, 34] was modeled in FLUENT to compare the computer simulation with the experimental values reported. The input parameters for the code were the heat flux, velocity, and the inlet salt temperature. The density, heat capacity, viscosity, and thermal conductivity were inputs for the code. The heat flux and velocity were recalculated from the mass flow rate, the salt inlet and outlet temperatures, and the physical parameters of the test section. The results indicated a deviation in the reported values compared to FLUENT for the wall surface temperature of each metal tube. At this point the reports were re-examined to try and determine if errors were reported in the thermocouples. Hoffman reports good agreement with the calibration of the thermocouples in the Inconel tube with the melting points of Pb, Al, and Zn. No specific data is given for this calibration with the other metal surfaces. Grele makes no mention of calibration of the thermocouples. The conclusion at this point is that the offset of the nickel and SS-316 data could be due to errors in the reported surface temperature, and it may be necessary to repeat this data.

Although the heat transfer by radiation was small compared to convection heat transfer in the experiments considered, it was desired to approximate at what point radiation heat transfer would become significant (i.e., greater than 10% of the total heat transfer term) for applications using nuclear heat for hydrogen production. In the intermediate heat exchanger, the flow of the salt is expected to be laminar and high temperatures. Under these conditions, radiation heat transfer to the salt may become significant (greater than 10%).

A Matlab script [39] was written that would compute the temperature of the salt such that 10% of the heat transfer to the fluid would be due to absorption of radiative energy. The absorption coefficient for radiant energy for FLiNaK was approximated by assuming that the reflectivity of FLiNaK was negligible.

Then the amount of energy absorbed by the salt would be $1 - C_t$, the transmission coefficient determined by Ewing [38]. The low and high values for the transmission coefficient were used, 6 or 27 m^{-1}. The average absorption length of the fluid (related to the diameter of the pipe) was varied from 1 to 100 mm. The radiation convective coefficient was then computed and compared to a forced convection coefficient.

The forced convective heat transfer coefficient was computed based on heat transfer correlations. A correlation used to compute the convection heat transfer coefficient in the laminar region (Re < 2,300) for constant heat flux is reported by Gnielinski as [40]:

$$Nu = [4.364^3 + 0.6^3 + (1.953 * Gz^{1/3} - 0.6)^3 + (0.924 * \text{Pr}^{1/3} (\text{Re} * d/L)^{1/2})^3]^{1/3} * \left(\mu/\mu_w\right)^{0.11}$$

(11)

where the Graetz number is

$$Gz = \text{Re} * \text{Pr} * (d/L). \quad (12)$$

Heat transfer in the turbulent region (Re > 10,000) is approximated by the DB correlation. The heat transfer in the transitional Reynolds flow was interpolated from the values from laminar flow and turbulent flow evaluated at Reynolds numbers of 2,300 and 10,000, respectively.

The wall temperature was fixed at 1173 K, the expected gas outlet temperature of the reactor. The temperature of the adjacent FLiNaK was solved by iteration until the heat transfer due to radiation between the metal and salt was equal to ten percent of the convective heat transfer term. Figures 81 and 82 show the temperature curves where the radiation heat transfer is equal to 10% of the total heat transfer for different diameter pipes. The regime to the upper left of the curve and below 1173 K is the area when radiation effects are significant. As the pipe diameter increases, the amount of energy that is transferred by radiation becomes significant for laminar flow regimes. Radiation is expected to become significant for pipe diameters greater than 8 mm and 16 mm, for Re < 200, for absorption coefficients of 6 and 27 m^{-1}, respectively.
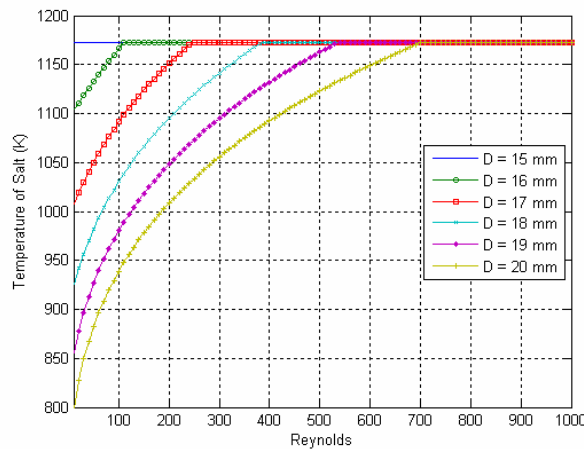
Figure 81. The radiation heat transfer from the pipe wall to the salt is > 10% of the total heat transfer) in the region above and to the left of the lines representing the diameter of the pipe. For an absorption coefficient of 6 m^{-1} and a temperature difference between wall and fluid of 50K , radiation effects become significant at Re < 500 for a pipe with a diameter of 20 mm.

81
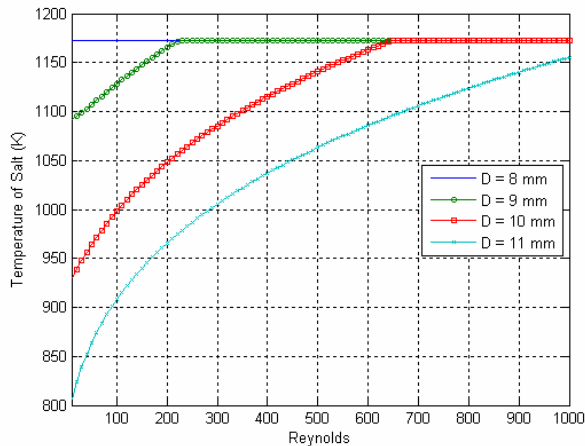
Figure 82. The radiation heat transfer from the pipe wall to the salt is > 10% of the total heat transfer in the region above and to the left of the lines representing the diameter of the pipe. For the case of an absorption coefficient of 27 m^{-1}, If a temperature difference between wall and fluid of 35 K is assumed, radiation effects become significant at Re <= 500 for a pipe with a diameter of 10 mm.

6.c. Molten Salt Flow Loop Design

The forced convection loop for molten salt research at the University of Wisconsin is designed to simulate conditions in the intermediate heat exchanger (IHX) and for study of transfer of heat and mass across the system. There are many challenges involved with the construction and instrumentation of the loop. Most deal with the chemical aggressiveness of this fluid at these elevated temperatures. During design of the loop, several key components of the system to the loop: materials, pump, mass flow measurement, temperature measurement, and pressure drop measurement, were considered. A front view of the loop and system shows the forced convection loop and major components, Figure 83.

The selection of the material for construction of the loop components was based on cost, ease of machining, and availability of material. After consideration of Inconel 600 and 316 stainless steel, it was decided that 316 stainless steel would be the material of choice for the loop construction. 316 stainless steel is more readiliy available and several corrosion studies using SS-316 at elevated temperatures have shown that it performs better than Inconel 600 in both fluoride and chloride environments, as shown in Table 18.

Two different types of connections were determined for feasibility for connecting pieces of the flow loop: Graylok and Swagelok. Swagelok connections were chosen for the loop, as this requires the use of tubing and not pipe. The purpose of the loop is to examine flow similar to conditions expected for the NGNP application. A maximum temperature of 850ºC at the outlet of the test section is targeted. If the heating rate is 200 K/m, the temperature rise in the test section will be 122 K. In order to get to 850ºC, the temperature of the incoming salt must be 725ºC. The pump was designed to operate at 600ºC and so the test section includes a preheat section to raise the temperature of the salt to the desired test inlet temperature.
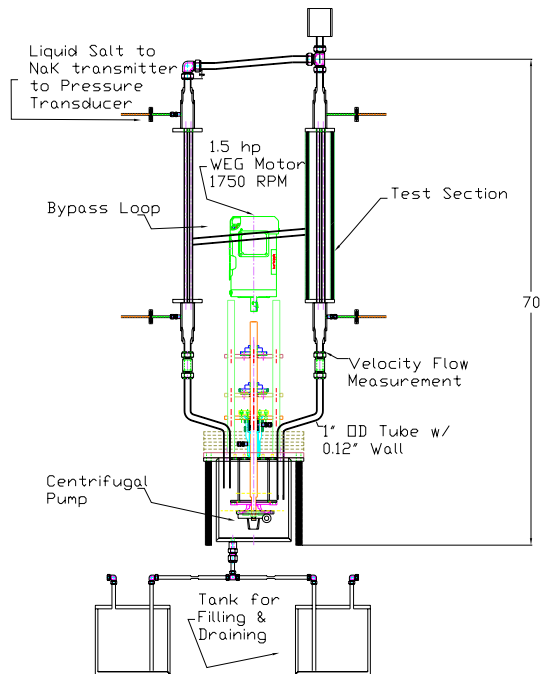
Figure 83. Design of forced convective loop includes design of centrifugal pump, flow loop, and instrumentation for velocity and pressure.

Table 18. Corrosion tests done at ORNL compared the corrosion resistance of SS-316, Inconel 600, and Hastelloy N (INOR-8).

Loop #	Alloy	Salt	Duration (hr)	Tmax (ºC)	Corrosion Depth (mil)	Corrosion Depth (mm/yr)	ORNL Report
116	SS-316	FLiNaK	500	815	4	1.78	1294
	Inconel	FLiNaK	500	815	7	3.12	1816
78	Inconel	FLiNaK	1000	815	13	2.89	1294 & 2337
1214	Inconel	FLiNaK	4673	677	13	0.62	2684
9344-2	Inconel	FLiNaK	8750	649	8	0.20	2890 & 3215
	INOR-8	FLiNaK	3048	815	0.1	0.01	
1208	INOR-8	FLiNaK	8760	677	1	0.03	2799
1165	INOR-8	FLiNaK	1340	677	0	0.00	2551
1194	INOR-8	FLiNaK	1000	607	0	0.00	2551

The pump and components of the molten salt loop must be able to operate to temperatures of 600ºC. The melting temperatures of FLiNaK is 454ºC and it remains viscous until about 500ºC. The main issue with the ability to pump liquids up to 550ºC is degradation of the lubricants and sealing materials. In most commercial centrifugal pumps, the seals are made from different types of polymers. The temperature of these materials is usually limited to 100ºC. The lubricating oils around the bearings usually degrade at temperatures above 200ºC.

In order to move away from these issues, the pump for the movement of the liquid salts will be a vertical cantilever type centrifugal pump. A vertical cantilever type pump removes the bearings away

from the fluid allowing the bearings to maintain a lower temperatures than the fluid being moved. Most available molten salt pumps are designed to transfer salt from a heat treatment bath to a reservoir during maintenance operations, and therefore their ability of the pump to operate at high temperatures for an extended period is uncertain. After consideration, it was decided to build the centrifugal pump at the University of Wisconsin.

The pump will be constructed using a commercially purchased motor, impeller, casing, suction cover, and bearings. The impeller, casing, and suction cover were removed from an AMT 368A-98 water centrifugal pump. These parts are manufactured by casting SS-316 and post-machining. The water pump and impeller is shown in Figure 84.

Figure 84. A complete water pump was purchased for SS-316 wetted materials: casing, impeller, and suction cover.

The diameter of the shaft was determined by looking at the torsional stress in the shaft. The radius of a rotating solid cylinder is determined by the following equation [41]:

$$ r = \sqrt[3]{\frac{2 * T_{max}}{\pi * G}} $$

the maximum torque (Tmax = 59 N-m for 1.5 hp engine at 1140 rpm), G – modulus of rigidity = 61.2 MPa for SS-316 at 600ºC. Solving the equation with a factor of safety of 2 for G, results in a radius of 0.422". The diameter of the shaft was chosen to be an inch for ease in machining. The length of the shaft is dependent on the ability to keep the temperature of the bearings below 200ºC. In order to keep the length of the pump shaft minimal, the shaft is actively cooled. The packing box seals the lid to the shaft to keep the atmosphere in the can free of oxygen. Copper tubes (1/4" diameter) are wrapped around the packing box. Previous experiments at the University of Wisconsin have shown that a heat removal rate of 6 kW/m is possible. Fluent code was used to calculate the temperature profile along the shaft. The temperature along the base and can lid was set to 600ºC. The heat removal rate at the bearings was set to -5 kW/m^2. This cooling rate is equal to 1/5th the expected cooling rate based on previous experiments. The model and results is shown in Figure 85. The average temperature of the bearings and shaft below the bearings is T$_{bearing}$= 94ºC and T$_{shaft}$ = 257ºC, respectively. The bearings will be able to remain cool during operation of the fluid at 600ºC.
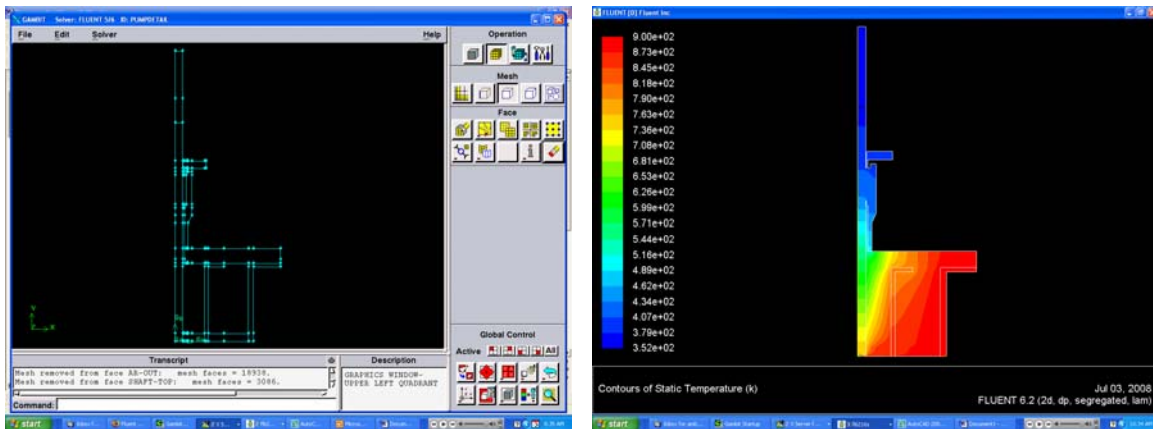
Figure 85. The model and results from Fluent calculation examining the temperature profile of the shaft and bearings.

The supports and shaft will not have the same temperature profile due to active cooling and other factors. This temperature difference will cause differences in thermal expansion that could become significant. This difference was accounted for in the design of the pump. From previous calculation, the average temperature of the shaft was 257ºC. The average temperature of the supports = 367ºC. The expected difference in thermal expansion would increase the length of the support by 0.03" relative to the shaft from startup to operating conditions.

The original motor to turn the pump was originally a 1/3 hp single phase WEG motor. A 1.5 hp, three phase, inverter duty motor will be used to power the centrifugal pump. The motor is oversized to ensure that the pump will be able to move the amount of salt needed for the test section. The ability to use an inverter on the pump allows for changing in the rpm of the pump. This will allow the pump output to be shifted to achieve the desired flow rate through the loop.

The pressure drop through the test section will be continuously monitored. The electronics in pressure transducers limit the maximum temperature of the fluid to 100ºC. In order to be able to withstand the temperature of the loop (600°C) the differential pressure gauge will be backfilled with NaK which is a fluid at both room temperature and at 600ºC. This will allow the electronics of the transducer to be at approximately room temperature, while keeping the temperature of the salt in the loop above the melting point. In order to get accurate pressure measurement, a wide diameter flange is needed to allow for the pressure to be transmitted across the SS-316 membraned. A pressure tap will come from before and after the test section through ¼" high pressure tube attached to the flange.

The flow rate of the fluid through the test section is an important parameter to measure accurately. The ability to produce accurate heat transfer calculations from the wall to the fluid are based on accurate knowledge of the mass flow rate. At high temperatures, ultrasonic waveguides have been used to measure the average velocity in a pipe [42, 43]. The waveguide isusually made out of SS-316 and acts as a fin to keep the piezoelectric device below 100ºC. Three different techniques have been developed for construction of waveguides: wrapped foil (t < 0.1 mm), bundle of small diameter tubes (D < 0.1 mm), and a thin fin (6.4 mm). The thin materials restrict the dispersion of the ultrasonic wave. Keeping the wave from dispersing and matching impedances of the different materials are two important factors in the ultrasonic waveguides.

7. References

1. Peterson, P., Zhao, H., and Fukuda, G. (December 5, 2003). *Comparison of Molten Salt and High-Pressure Helium for the NGNP Intermediate Heat Transfer Fluid*, Report UCBTH-03-004, pp. 1-12.

2. Williams, D., Wilson, D., Keiser, J, Toth, L., and Caja, J. (2003). *Research on Molten Fluorides as High Temperature Heat Transfer Agents*, Global 2003, Session 2A: Coolant/Material Interactions in Advanced Reactor Systems, Embedded Topical Within 2003 American Nuclear Society Winter Meeting, November 16-20, 2003, New Orleans, Louisiana, pp. 1-12.

3. Manly, W., Coobs, J., DeVan, J., Douglas, D., Inouye, H., Patriarca, P., Roche, T., and Scott, J. (1960), *Metallurgical Problems in Molten Fluoride Systems*, Progress in Nuclear Energy, Series IV: Technology, Engineering and Safety, Vol. 2, pp. 164-179.

4. Forsberg, C.W., (June 7, 2006) High-Temperature Reactors for In Situ Recovery of Oil from Oil Shale, Presentation for ICAPP'06; Paper 6104

5. Williams, D.F., Assessment of Candidate Molten Salt Coolants for the NGNP/NHI Heat-Transfer Loop, ORNL/TM-2006/69, 2006, pp. 1-44.

6. Peterson, P.F., Zhao, H., *proc. ICAPP* (2006), Reno, NV, Paper No. 6052.

7. Williams, D., Toth, L., Clarno, K., and Forsberg, C. (June 30, 2005). *Assessment of Properties of Candidate Liquid Salt Coolants for the Advanced High Temperature Reactor (AHTR)*, ORNL/GEN4/LTR-05-001, pp. 1-38.

8. Janz, G., and Tomkins, R. (July, 1981). *Physical Properties Data Compilations Relevant to Energy Storage, IV. Molten Salts: Data on Additional Single and Multi-Component Salt Systems*, Molten Salts Data Center, Cogswell Laboratory, Rensselaer Polytechnic Institute, pp. 192-204.

9. Dr. David Williams and Dr. Dane Wilson, ORNL, private communications, 2005 to 2007.

10. POCO Inc. (2006). AXZ-5Q, [online], accessed 4/26/2006, available: http://www.poco.com/us/Graphite/axz.asp.

11. Sheppard, R., Mathes, D., and Bray, D. (November, 2001). *Poco Graphite, Inc. Properties and Characteristics of Graphite for Industrial Applications*, [online], accessed 4/26/2006, available: http://www.poco.com/us/literature/files/Graphite/Properties.and.Characteristics.of.Graphite.for.Industrial.Applications.pdf

12. Metzger, G. (1967). *Survey of Structural Materials for the Molten Salt Experimental ("MOSEL") Reactor*, Nuclear Engineering and Design, Vol. 7, pp. 29-39.

13. Kirillov, V., and Fedulov, V. (November-December, 1980) The Corrosion Resistance of 12Kh18N10T Steel in Molten Fluoride Salts, translated from *Fiziko-Khimicheskaya Mekhanika Materialov*, Vol. 16, No. 6, pp. 22-25.

14. Ingersoll, D., Forsberg, C., Ott, L., Williams, D., Renier, J., Wilson, D., Ball, S., Reid, L., Corwin, W., Del Cul, G., Peterson, P., Zhao, H., Pickard, P., Parma, E., and Vernon, M. (May, 2004). *Status of Preconceptual Design of the Advanced High-Temperature Reactor (AHTR)*, ORNL/TM-2004/104, [online] available: http://www.ornl.gov/~webworks/cppr/y2001/rpt/120370.pdf, pp. 1-105.

15. McKoy, H., Beatty, R., Cook, W., Gehlbach, R., Kennedy, C., Koger, J., Litman, A., Sessions, C., and Weir, J. (February, 1970). *New Developments in Materials for Molten-Salt Reactors*, Nuclear Applications & Technology, Vol. 8, pp. 156-169

16. Davis, C., Oh, C., Barner, R., Sherman, S., and Wilson, D. (June, 2005). *Thermal-Hydraulic Analyses of Heat Transfer Fluid Requirements and Characteristics for Coupling A Hydrogen Production Plant to a High-Temperature Nuclear Reactor*, INL/EXT-05-00453, pp. 1-87.

17. Ingersoll, D., Forsberg, C., Ott, L., Williams, D., Renier, J., Wilson, D., Ball, S., Reid, L., Corwin, W., Del Cul, G., Peterson, P., Zhao, H., Pickard, P., Parma, E., and Vernon, M. (May, 2004). *Status of Preconceptual Design of the Advanced High-Temperature Reactor (AHTR)*, ORNL/TM-2004/104, [online], available: http://www.ornl.gov/~webworks/cppr/y2001/rpt/120370.pdf, pp. 1-105.

18. Shaw, B. (2002). ASM Handbook: Volume 7, *Powder Metal Technologies and Applications: Corrosion-Resistant Powder Metallurgy Alloys*.

19. Safranek, W. (1986). *The Properties of Electrodeposited Metals and Alloys*: A Handbook, Second Edition, pp. 253-326.

20. Weil. R., Jacobus, W., DeMay, S. (September, 1964). *Journal of the Electrochemical Society*, pp. 1046-1052.

21.Safranek, W., and Schaer, G. (1956), Technical proceedings of the annual convention – *American Electroplaters' Society*, Vol. 43, pp. 105-117.

22. Jacobson, B., and Silwa, J. (September, 1979), *Plating and Surface Finishing*, Vol. 66, No. 9, pp. 42-47.

23. Tabet, N., Allam, I., Yin, R. (2003), *Applied Surface Science*, pp. 259-272

24. Detroye, M., Reniers, F., Buess-Herman, C., Vereecken, J. (1999). *Applied Surface Science*, pp. 78-82.

25. Ozeryanaya, I. (1985). *Metal Science and Heat Treatment*, No. 3, pp. 184-188.

26. Streicher, M. (1976). *Corrosion-NACE*, Vol. 32, No. 3, pp. 79–93.

27. Jackson, J., LaChance, M. (1954). *Transactions of the ASM*, Vol. 46, pp. 157-183.

28. Jenkins, H., Mamantov, G., and Manning, D., *Journal of Electrochemical Society.* 117 (1970): 183-185. (ALSO ORNL-4812).

29. Mellors, G. and Senderoff, S. *Proceedings of the First Conference on the Thermodynamic Properties of Materials* (University of Pittsburgh), Gordon and Breach Science Publishers. New York. (1969) 81-103.

30. Manning, D. *Journal of the Electrochemical Society.* 6 (1963): 227-233.

31. Chryssoulakis, J, Bouteillon, J., and Poignet, J.C., 8 (1978) 103-108.

32. Sannier, J. and Santarini, G. (20-22 April 1983), *Studies of Materials for Molten Salt Nuclear Applications, 1st Int. Symp. Molten Salt Chemistry and Tech*., Kyoto, Japan,.

33. Hoffman, H.W. & Lones, J. (Feb. 1955), *Fused Salt Heat Transfer Part II: Forced Convection Heat Transfer in Circular Tubes Containing NaF-KF-LiF* Eutectic, ORNL 1777.

34. Grele, M.D. & Gedeon, L. (Feb 1954), *Forced-Convection Heat-Transfer Characteristics of Molten FLiNaK Flowing in an Inconel X System,* NACA RM E53L18

35. Vriesema, I. B. (Jan. 1979), *Aspects of Molten Fluorides as Heat Transfer Agents for Power Generation,* WTHD No. 112, Delft University of Technology, Netherlands

36. Ignat'ev, V.V, et al (Aug 1984), *Atomnaya Énergia*, v. 57, No 2, pp 123-124

37. Williams, D.F. (June 2005), et al, *Assessment of Properties of Candidate Liquid Salt Coolants for the Advanced High Temperature Reactor (AHTR),* ORNL/GEN4/LTR-05-001

38. Ewing, C.T. (Apr. 1962), et al, *Journal of Chemical and Engineering Data*, V 7, No 2, pp 246-250

39. Computer program, Matlab R2006, (The MathWorks, 2006)

40. V. Gnielinski, *Forschung im Ingenieurwesen* (Engineering Research), 61 (9), 240 (1995).

41.Young, W.C., *Roark's for Stress and Strain*, Sixth Ed., Ch. 8

42. Lynnworth, L.C., *Extensional Bundle Waveguide Techniques for Measuring Flow of Hot Fluids,* IEEE Transactions on Ultrasonic, Ferroelectrics, and Frequency Control, Vol. 52, No. 4, April 2005

43. Eckert, S., Gerbeth, G., Melnikov, V.I., *Velocity Measurements at High Temperatures by Ultrasound Doppler Velocimetry Using an Acoustic Wave Guide,* Experiments in Fluids, 35 (2003) pp 381-388